A new Climate Data Record of Upper Tropospheric Humidity

Masterarbeit

zur Erlangung des akademischen Grades eines
Master of Science der Meteorologie
an der Universität Hamburg

von

Theresa Lang

Hamburg, April 2019

Erstgutachter: Prof. Dr. Stefan Bühler
Meteorologisches Institut, Universität Hamburg

Zweitgutachter: Dr. Martin Burgdorf
Meteorologisches Institut, Universität Hamburg

Thema der Arbeit:
A new Climate Data Record of Upper Tropospheric Humidity

Abstract

The amount of water vapour in the upper troposphere has a substantial impact on the Earth's radiation budget and therefore plays an important role in modelling climate change. To evaluate climate models, long-term observational data records of upper tropospheric water vapour are needed. The creation of such a Climate Data Record (CDR) from satellite observations is the aim of this thesis. The core variable in the CDR is the Upper Tropospheric Humidity (UTH), which is a vertical average of the relative humidity in the upper troposphere, roughly in a layer between 200 and 500 hPa. UTH can be derived from brightness temperatures measured with passive infrared and microwave sensors using a simple exponential relationship. A combination of observations from both kinds of sensors would allow the creation of a 40 year time series of UTH and is therefore of great interest for climate research. However, a direct comparison of infrared and microwave UTH is not possible due to the current definition of UTH, which depends on the specific instrument channel used for the measurement.

Therefore, this thesis introduces a new definition of UTH that is identical for the water vapour channels of the infrared instrument HIRS/2 and the microwave instruments MHS, AMSU-B and SSMT-2. Thus, it will allow to combine UTH CDRs based on infrared and microwave measurements. However, a general weakness of the concept of UTH is not solved with the new definition. It is owed to the fact that the brightness temperature is influenced by other factors than relative humidity. By means of idealised climate model simulations I show that a shift of the emission layer to lower pressure in a warming climate leads to an increase in the infrared brightness temperature. Thus, the infrared UTH decreases in a warming climate even though the relative humidity might stay unchanged.

In the second part of this thesis, the new UTH definition is used to create a Microwave UTH CDR based on calibrated brightness temperatures from a Fundamental Climate Data Record (FCDR). The UTH CDR includes all satellite missions carrying the SSMT-2, AMSU-B and MHS instruments and covers the time period from 1994 to 2017. It contains monthly averages of brightness temperature and UTH, mapped on a regular latitude-longitude grid covering the tropical region. Besides the new UTH definition, another new feature of the CDR is the fact that it contains measurement uncertainties, which are propagated from the FCDR. However, it is shown that these are not the only uncertainties at CDR level because additional uncertainties arise from assumptions made during the CDR processing. Based on these additional sources of uncertainty I provide a guideline on how to create a time series of tropical mean UTH from the CDR data.

Contents

List of Figures

List of Tables

List of abbreviations

AMSU-B	Advanced Microwave Sounding Unit - B
ARTS	Atmospheric Radiative Transfer Simulator
BT	Brightness Temperature
CDR	Climate Data Record
CF	Climate and Forecast
CMIP5	Coupled Model Intercomparison Project 5
DMSP	Defence Meteorological Satellite Program
EUMETSAT	European Organisation for the Exploitation of Meteorological Satellites
FCDR	Fundamental Climate Data Record
FIDUCEO	Fidelity and Uncertainty in Climate Data Records from Earth Observations
GUM	Guide to the expression of uncertainty in measurement
HIRS	High-Resolution Infrared Radiation Sounder
HITRAN	High-Resolution Transmission Molecular Absorption Database
IR	Infrared
IWV	Integrated Water Vapour
L1, L2, L3	Level 1, Level 2, Level 3
Metop	Meteorological Operational Satellite
MHS	Microwave Humidity Sounder
MPI-ESM	Max-Planck-Institute Earth System Model
MW	Microwave
NOAA	National Oceanic and Atmospheric Administration
OLR	Outgoing Longwave Radiation

RCE	Radiative Convective Equilibrium
RH	Relative Humidity
RTTOV	Fast Radiative Transfer Model for TOVS
SSMT-2	Special Sensor Microwave Temperature - 2
TIROS	Television Infrared Observing Satellite
TOA	Top of the Atmosphere
TOVS	TIROS Operational Vertical Sounder
UTH	Upper Tropospheric Humidity
VMR	Volume Mixing Ratio

CHAPTER 1

Introduction

Water vapour is the predominant greenhouse gas in the Earth's atmosphere and therefore plays an important role in modelling climate change (Held and Soden, 2000). The concentration of water vapour is expected to increase in a warmer climate (IPCC, 2013). In that case, the additional absorption by water vapour will act to further amplify the climate system's response to all other greenhouse gasses. Climate models predict that this so-called water vapour feedback increases the sensitivity of surface temperature to CO_2 by almost a factor of two (Held and Soden, 2000; Pierrehumbert et al., 2007).

Even though most of the atmospheric water vapour is confined to the low warm parts of the troposphere, it is the comparably small amount of water vapour in the upper troposphere that has the largest impact on the Outgoing Longwave Radiation (OLR) and hence on the Earth's radiation budget (Pierrehumbert et al., 2007). Since the radiative effect of water vapour is logarithmic in its concentration, it is not the absolute, but the fractional change in water vapour that determines its impact. Therefore, small additional quantities of water vapour in the upper troposphere are sufficient to significantly alter the OLR. This vital importance of water vapour in the upper troposphere has led to the concept of Upper Tropospheric Humidity (UTH). It can be defined as the relative humidity in the altitude region of the atmosphere that has a significant impact on the radiation budget.

Virtually all climate models show a water vapour feedback that is consistent with an approximately constant upper-tropospheric relative humidity (e.g. Soden and Held, 2006; John and Soden, 2007). However, the validity of these projections has been debated controversially (e.g. Lindzen et al., 2001; Minschwaner and Dessler, 2004; Soden et al., 2005). Hence, long-term observational data records of UTH are needed to evaluate

climate models. The longest existing humidity data record available is provided by radiosonde measurements. However, the quality of radiosonde measurements tends to be poor under the cold and dry conditions of the upper troposphere (Elliot and Gaffen, 1991) and the spatial coverage of such measurements is sparse, especially over the oceans. This leaves satellite measurements as the only source of UTH observations providing global coverage.

For the measurement of UTH with satellite instruments two frequency bands are commonly used. One is in the infrared (IR) spectral region near the strong water vapour vibrational absorption band at 6.3 μm and one lies in the microwave (MW) spectral region near the water vapour rotational absorption line at 183.31 GHz. In both cases, UTH is obtained from the measured brightness temperature via a simple exponential relationship. IR instruments are the more established ones to make measurements of UTH and hence go back further in time. Starting in 1979, the longest data record is provided by the High-Resolution Infrared Radiation Sounder (HIRS) (Shi and Bates, 2011). In recent years, MW instruments such as the Special Sensor Microwave Temperature - 2 (SSMT-2), the Advanced Microwave Sounding Unit - B (AMSU-B) and the Microwave Humidity Sounder (MHS) have been increasingly relied on for studying UTH (e.g. Buehler et al., 2008). These MW measurements are less affected by clouds than IR measurements and therefore provide better coverage.

A combination of UTH derived from IR and MW observations would allow the creation of a time series covering a 40 year period. However, such a combination is problematic due to the way UTH is currently defined. The definition is based on the water vapour Jacobian and hence depends on the specific instrument channel that is used for the measurement of brightness temperature. Consequently, UTH measured with an IR instrument is defined differently than UTH measured with a MW instrument. Thus, comparing UTH derived from different instrument types or even combining them into one data record is hardly possible.

To overcome this problem, I introduce a new definition of UTH in this thesis. It is based on more fundamental characteristics of the atmosphere than the Jacobian and it is consistent for both IR and MW instruments and as such allows for them to be combined. This definition is used to create a new Climate Data Record (CDR) of UTH based on MW brightness temperatures from a Fundamental Climate Data Record (FCDR), which has been created in the framework of the Horizon 2020 project Fidelity and Uncertainty in

Climate Data Records from Earth Observations (FIDUCEO). As a second novelty, the new CDR contains estimations of measurement uncertainties, which are propagated from the FCDR.

First, an introduction into the concepts of satellite-borne remote sensing of water vapour and the satellite instruments used in this thesis as well as some basic knowledge about CDRs and uncertainty propagation is provided. Then, the revised UTH definition is introduced including its optimization procedure and an assessment of the updated UTH retrieval. In Chapter 4, idealised climate model simulations are used to investigate how UTH behaves in a warming climate. It is pointed out how a warming atmosphere can lead to trends in the observed UTH, even though the upper-tropospheric relative humidity might stay unchanged. Finally, the creation of the microwave UTH CDR including input data, processing chain and contents is described. This is concluded by a discussion of the sources of uncertainty at CDR level and a guideline for the creation of a time series of tropical mean UTH.

CHAPTER 2

Theoretical basis

2.1 Satellite-borne remote sensing of upper-tropospheric water vapour

The amount of water vapour in the upper troposphere can be derived from measurements with passive infrared and microwave radiometers. These instruments measure the thermal radiation emitted by the atmosphere and the Earth's surface. The basic concepts of radiative transfer needed to understand these measurements are explained in the following sections.

2.1.1 Propagation of thermal radiation through the atmosphere

Satellite instruments used to measure atmospheric water vapour in this thesis operate either in the infrared or in the microwave spectral region. Thus, I will focus on the propagation of thermal radiation through the atmosphere. Since the wavelength of infrared waves (typically 1 μm to 1 mm) is more than three magnitudes larger than the typical size of an air molecule, scattering effects can be ignored. This is only true in the clear-sky case, meaning that no hydrometeors such as cloud droplets or ice crystals are present. Here, only the clear-sky case is considered.

A radiometer on-board a satellite oriented vertically towards the Earth's surface receives the intensity of radiation I (unit $\mathrm{Wm^{-2}sr^{-1}}$):

$$I = \int_{\Delta\nu} F(\nu)\, I_\nu \, d\nu, \tag{2.1}$$

where ν is the frequency, $\Delta\nu$ is the frequency range the channel is sensitive to and $F(\nu)$ is the spectral response function of the channel. I_ν is the spectral radiance, i.e. the radiance at a given frequency ν (in units of $\mathrm{Wm^{-2}sr^{-1}Hz^{-1}}$), which is obtained by the solution of Schwarzschild's equation in the absence of scattering via (Wu et al., 1993):

$$I_\nu = B_\nu(T_s)\,\tau_\nu(p_s) + \int_{p_s}^{0} B_\nu(T(p))\,\frac{\partial\tau_\nu(p)}{\partial p}\,dp. \tag{2.2}$$

Here, B_ν is the Planck function, yielding the thermal emission of a black body for a given frequency ν and temperature T. The parameter $\tau_\nu(p)$ is the atmospheric transmittance from a pressure level p to the top of the atmosphere (TOA). T_s and p_s denote the temperature and pressure at the Earth's surface, respectively.

As can be seen from the right hand side of Equation 2.2, the spectral radiance that reaches the TOA is composed of two terms: The first term describes the radiation that is emitted by the Earth's surface and altered by absorption as it propagates through the atmosphere. The second term describes the sum of the thermal emissions by all atmospheric layers. The emission of each layer $B_\nu(T(p))$ is weighted with a factor that takes into account the transmittance τ_ν of the atmosphere above this layer. This factor is often called the weighting function $W_\nu(p)$:

$$W_\nu(p) = \frac{\partial\tau_\nu(p)}{\partial p}. \tag{2.3}$$

For the channels used for remote sensing of upper tropospheric water vapour, the surface term in Equation 2.2 is negligibly small because the atmospheric transmittance is close to zero. Thus, the measurement I of a radiometer is a function of the radiation emitted at each level p, modulated by the weighting function W.

The radiometers used in this thesis are calibrated in terms of brightness temperature (BT). The brightness temperature is the temperature a black body needs to have to emit a given spectral radiance within a given frequency range. Spectral radiances and BTs can be converted into each other via the Planck function. Consequently, the two quantities differ in their units: Spectral radiances are given in Watts per square metre, Herz and steradian ($\mathrm{Wm^{-2}}\,Hz^{-1}\,sr^{-1}$), whereas brightness temperatures are given in Kelvin (K).

2.1.2 Upper-tropospheric water vapour channels

Two frequency bands are commonly used to measure upper tropospheric water vapour: One is located near the strong water vapour absorption band at 6.3 μm in the infrared (IR) region, the other one is located close to the water vapour absorption line at 183.31 GHz in the microwave (MW) region. These channels will hereafter be called upper tropospheric humidity channels (UTH channels). The UTH channels of the IR instrument (HIRS/2) and MW instruments (SSMT-2, AMSU-B and MHS) used in this thesis (see Section 2.2) are centred at 6.72 μm and at 183.31±1 GHz, respectively. Both channels are sensitive to water vapour in a very similar altitude range of the atmosphere.

Figure 2.1 shows where the two channels are located in the clear-sky outgoing longwave radiation (OLR) spectrum of a typical tropical atmosphere. It reveals an important difference between the two channels: While the MW 183.31±1 GHz channel is located on the two flanks of a single water vapour rotational absorption line, the IR 6.72 μm channel has a larger bandwidth and includes a large amount of narrow, irregularly spaced absorption lines due to the fine structure of the ν_2 vibrational band. This difference should be kept in mind, even though the two channels will be treated equally in the first part of this thesis. It will become important when the evolution of BT in a warming climate is investigated (Chapter 4).

2.1.3 Interpretation of brightness temperature measurements

The BT observed in a UTH channel reflects the average temperature in a certain atmospheric layer, hereafter called emission layer, which is determined by the weigthing function W of the channel (Section 2.1.1). This emission layer roughly corresponds to the layer between 200 and 500 hPa, but its exact altitude and thickness are mainly controlled by the vertical distribution of water vapour in the atmosphere. Wu et al. (1993) showed that there is usually a defined amount of accumulated water vapour above the top and bottom of the emission layer. This concept will become important later when a new definition for upper tropospheric humidity is introduced. In a moist atmosphere, the emission layer is located at higher altitudes than in a dry atmosphere. As the temperature in the troposphere generally decreases with increasing altitude, high (low) BTs are associated with low (high) humidity. Thus, the BT in an UTH channel can be used as an indicator of the water vapour content under certain conditions. Most importantly, the variations of BT due to water vapour must be much larger than variations due to any

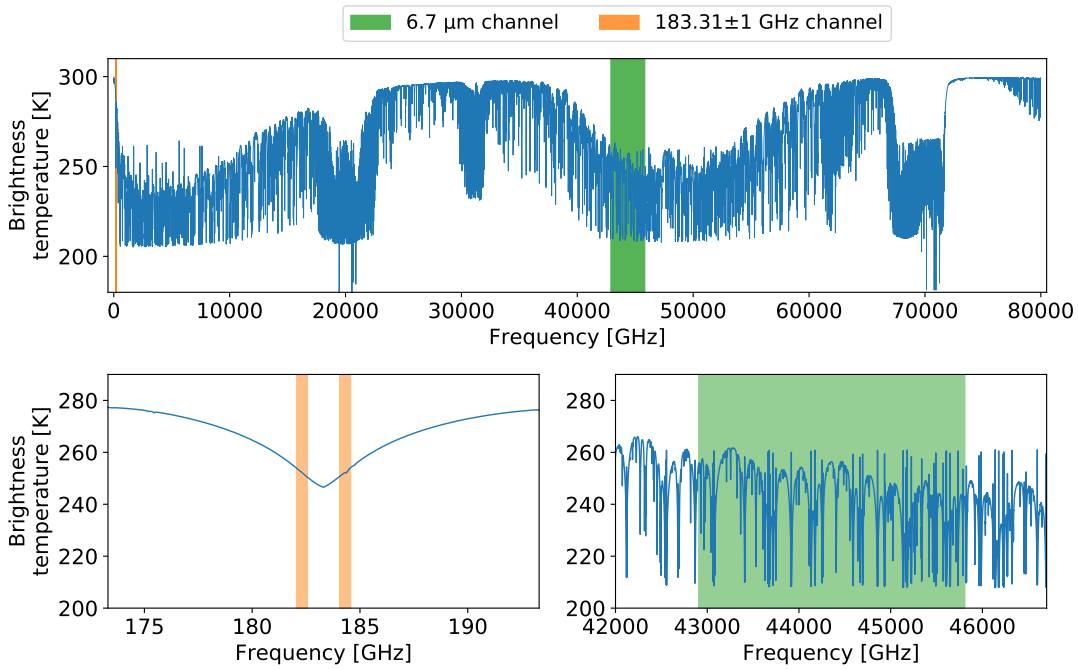

Figure 2.1: Upper panel: Clear-sky brightness temperature emitted by a typical tropical atmosphere (blue) with locations of the HIRS 6.7 µm UTH channel (green) and the AMSU-B 183.31±1 GHz UTH channel (orange). Lower panels: Zoom into the two UTH channels.

other factor like temperature. Wu et al. (1993) showed that this is true especially in the tropical region, where the variation of the 6.7 µm BT due to typical variations of specific humidity is more than three times larger than due to typical variations in temperature.

Soden and Bretherton (1993) showed that BT in the 6.7 µm UTH channel is most sensitive to changes in relative humidity (RH). This can be illustrated by a simple experiment: In a first step, BTs are simulated with the Atmospheric Radiative Transfer Simulator (see Section 3.2.2 for more details) for a set of about 2300 tropical atmospheric profiles that cover a broad range of humidities. As shown in Figure 2.2, the simulated BTs extend over a range of approximately 40 K. In a second step, all profiles are artificially saturated so that their RH is 100 % with respect to liquid water in the whole troposphere. In contrast to the first simulation, the range of occurring BTs shrinks to about 6 K (Figure 2.2). This shows that BT is indeed controlled by RH to a large extent. However, it should be pointed out that there is some remaining variability in BT, which is caused by other factors than RH.

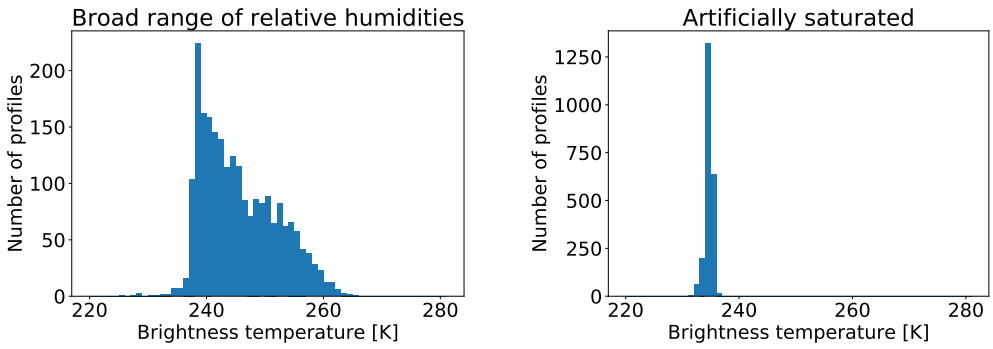

Figure 2.2: Histogram of simulated 6.7 µm BT for 2300 tropical profiles that cover a broad range of RH (left panel) and are artificially saturated (right panel) throughout the whole troposphere. In the saturated scenario the range of BTs shrinks to about 15% of the range of BTs in the scenario with a broad range of humidities.

2.1.4 Jacobians

When satellite measurements are analysed it is helpful to determine from which atmospheric layers the measured signal originates. For a given atmospheric profile this can be investigated by calculating the so-called Jacobian with a radiative transfer model. The Jacobian matrix $\boldsymbol{K}$ encodes the change in the radiance vector $\partial\vec{y}$ for a change in any element of the atmospheric state vector $\partial\vec{x}$ assuming a linear relationship around a given atmospheric state $\vec{x_0}$ (NWP SAF-webpage, 2019):

$$\boldsymbol{K}(\vec{x_0}) = \frac{\partial\vec{y}}{\partial\vec{x}}. \tag{2.4}$$

The components of the vector $\vec{y}$ are the observed signals in different spectral channels. They can be given in units of either radiance or brightness temperature. The vector $\vec{x}$ can contain any state variable, like temperature or water vapour content. Its components correspond to different altitude levels in the atmosphere. The Jacobian can be given either in fractional or in absolute units, i.e. it expresses the change in $\vec{y}$ due to absolute or relative changes in $\vec{x}$.

For example, following Buehler and John (2005) one can calculate a Jacobian to determine how sensitive the observed brightness temperature in a specific channel c is to relative changes in the water vapour volume mixing ratio (VMR) in different altitude

levels i. In this case, the Jacobian is a vector containing one value for every altitude level. The only component of $\vec{y}$ is the brightness temperature in the channel c (BT_c):

$$\boldsymbol{K}_c = \frac{\partial BT_c}{\partial \vec{x}}. \tag{2.5}$$

The vector $\vec{x}$ contains the water vapour VMR ($VMR^{\mathrm{H_2O}}$) at the individual altitude levels in fractional units:

$$x_i = \frac{VMR_i^{\mathrm{H_2O}}}{VMR_i^{\mathrm{Ref}}}, \tag{2.6}$$

where the constant VMR^{Ref} is equal to the VMR profile for which the Jacobian is calculated.

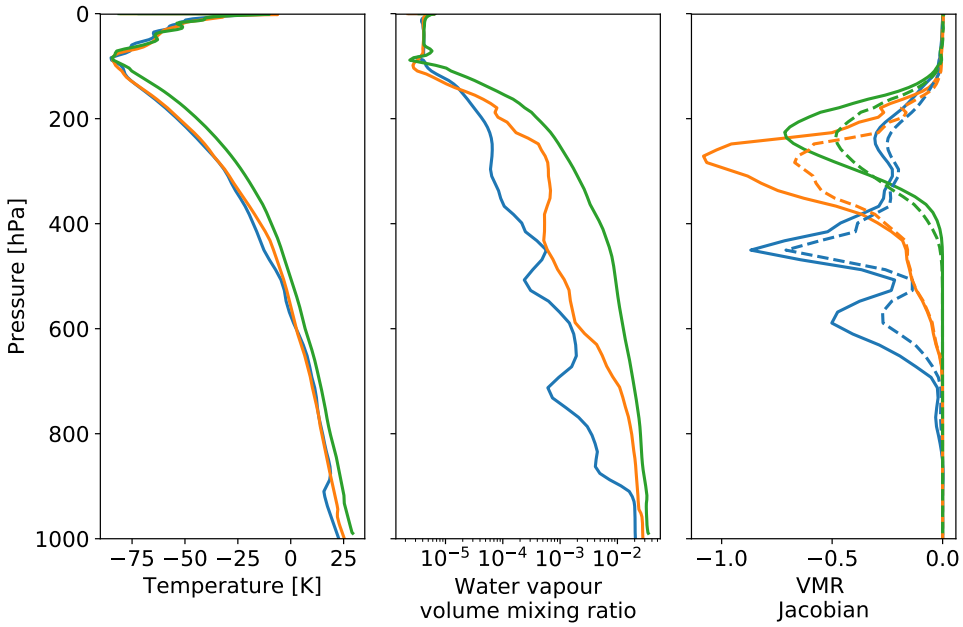

Figure 2.3: Temperature profiles (left panel) and water vapour VMR profiles (middle panel) for three different tropical atmospheres (blue, orange and green) as well as the corresponding fractional water vapour VMR Jacobians (right panel) for the UTH channels at 183.31±1 GHz (solid lines) and 6.7 µm (dashed lines), respectively.

Figure 2.3 shows three examples of tropical temperature and water vapour profiles and the corresponding fractional water vapour VMR Jacobians of the 183.31 ± 1 GHz and the 6.7 μm channel, respectively. They have a negative sign because an increase in $VMR^{\mathrm{H_2O}}$ leads to a decrease in BT. The Jacobians all peak somewhere in the upper troposphere, but the exact shape of the Jacobian depends on the atmospheric water vapour profile. The larger the water vapour concentration, the higher the peak altitude of the Jacobian. As can be seen from Figure 2.3, the Jacobians of the 183.31 ± 1 GHz and the 6.72 μm UTH channels are similar, but not identical.

2.1.5 Upper Tropospheric Humidity (UTH)

The Upper Tropospheric Humidity (UTH) is a quantity that helps to interpret brightness temperatures measured in IR and MW water vapour channels by scaling it to a more intuitive unit. UTH roughly corresponds to the vertical average of RH in a broad layer between 200 and 500 hPa, but the exact definition is more complex and will be explained below. In this work RH is always defined as the ratio of the water vapour pressure to the equilibrium value relative to water.

The concept of UTH is based on the fact that the BT measured in an UTH channel is mainly controlled by RH (Section 2.1.2). Soden and Bretherton (1993) derived a simple relation between BT in the 6.7 μm channel and UTH:

$$\ln(UTH) = a + b\,BT, \tag{2.7}$$

where a and b are constants. It has been shown that the same relation can be used for the BT in the 183.31±1 GHz channel (e.g. Buehler and John, 2005). It will hereafter be referred to as the BT transformation method. UTH is an appropriate vertical average of the RH profile. This average cannot be performed over a fixed atmospheric layer, because the emission layer varies depending on the atmospheric water vapour content (Section 2.1.2). Therefore, UTH is usually defined as the RH weighted with the humidity Jacobian of the specific UTH channel that is used to measure BT. This definition of UTH is illustrated in Figure 2.4 and will hereafter be referred to as the traditional UTH definition. Note that different kinds of humidity Jacobians have been used in the definition. In this thesis, fractional water vapour VMR Jacobians (Figure 2.3) are used as suggested by Buehler and John (2005).

The original form of Equation 2.7 derived by Soden and Bretherton (1993) additionally included a scaled reference pressure and a dimensionless lapse rate parameter. In various later studies one or both of these parameters were omitted on the grounds that they did not significantly improve the performance of the transformation method. An overview over the different forms of the transformation method used across the years is given by Jackson and Bates (2001). In this thesis, the form given by Equation 2.7 is used. Its advantage is that in order to determine the RH no information about the atmospheric profile is needed in addition to the measured BT. However, it will be shown in Chapter 4 that the inclusion of a reference pressure becomes important when climate trends of UTH are analysed.

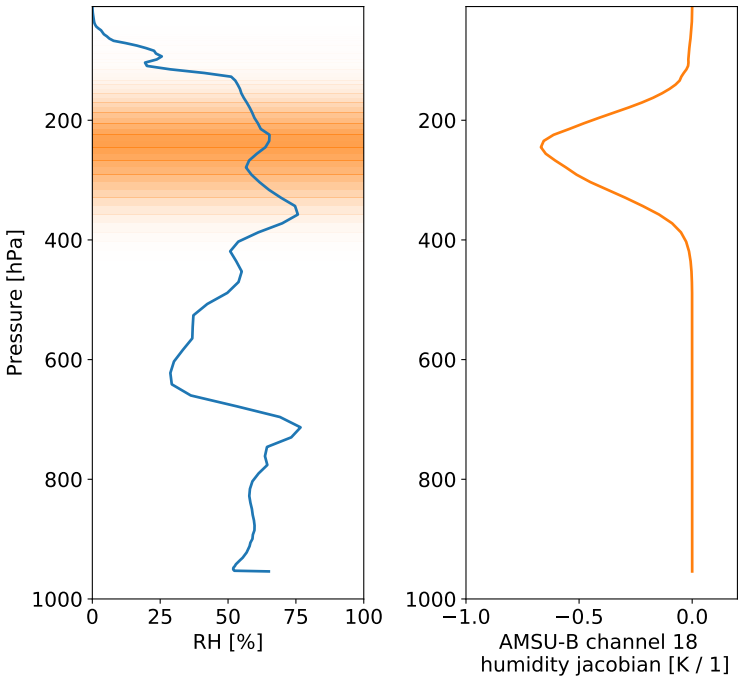

Figure 2.4: Illustration of the traditional definition of UTH: Example of an atmospheric profile of RH (left panel) and the corresponding humidity Jacobian (right panel) which is used for the weighting. The weighting factors for the individual atmospheric layers are indicated by orange shading. The specific Jacobian depicted here is for the 183.31±1 GHz channel of the microwave sensor AMSU-B and shows the change of BT due to a doubling of the water vapour VMR.

The definition of UTH depends on the viewing angle of the satellite. As the viewing angle moves away from nadir, the path length of the radiation through the atmosphere increases and hence the measured signal originates from higher altitudes. Therefore, the UTH scaling (Equation 2.7) has to be performed separately for all viewing angles θ and the corresponding Jacobian $K(\theta)$ has to be used in the UTH definition:

$$UTH(\theta) = \frac{\sum_i K_i(\theta)\, RH_i}{\sum_i K_i(\theta)}, \tag{2.8}$$

where i indicates the altitude level. Consequently, the scaling coefficients a and b also depend on the viewing angle.

These scaling coefficients are usually determined via regression (e.g. Buehler and John, 2005): First, a radiative transfer model is used to simulate BTs and Jacobians for a set of training atmospheres. Then, the Jacobians are used to calculate the true UTH of the atmospheres according to equation 2.8. Finally, the coefficients a and b are derived assuming a linear relation between BT and ln(UTH) (equation 2.7). Figure 2.5 illustrates the regression using the nadir view of the AMSU-B instrument (see Section 2.2.1) as an example.

Limitations of UTH

A general limitation of the UTH concept is that it can only be derived from measurements of BT that are not influenced by clouds. Thus, cloudy scenes have to be discarded before UTH can be derived. This cloud filtering, however, results in a negative bias in UTH (John et al., 2011) because cloud free scenes, which are associated with low UTH values, are sampled preferentially. This so-called clear-sky bias is larger for IR measurements because they require a more rigorous cloud filtering than MW measurements. Furthermore, the derivation of UTH is usually restricted to the tropics and midlatitudes. Under extremely dry conditions, the atmosphere gets too transparent and even in the UTH channels the largest part of the radiation reaching the instrument originates from the Earth's surface. Such extreme conditions occur rarely in the tropics, but frequently in high latitudes.

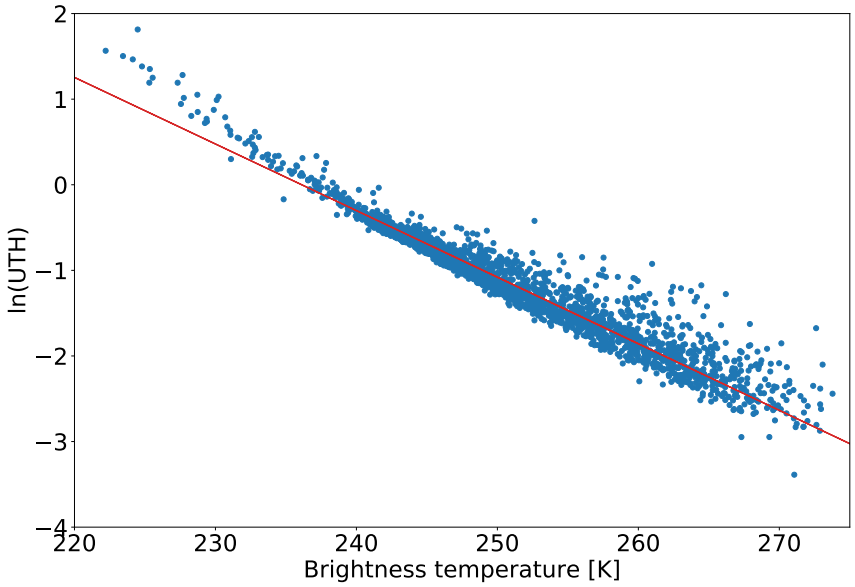

Figure 2.5: Illustration of the BT transformation method: For a set of training atmospheres the logarithm of UTH is plotted against the nadir BT of the AMSU-B instrument (blue dots). The resulting regression line is depicted in red.

The BT transformation method has been used for both IR BTs (e.g. Soden and Bretherton, 1993; Bates, 2001; Soden et al., 2004) and MW BTs (e.g. Spencer and Braswell, 1997; Greenwald and Christopher, 2002; Buehler and John, 2005; Buehler et al., 2008). However, comparing UTH derived from IR and MW BTs is problematic due to the way UTH is traditionally defined (Equation 2.8). Although IR and MW UTH channels are sensitive to RH in a similar altitude region, the shapes of the respective humidity Jacobians slightly differ (Figure 2.3). Thus, UTH derived from IR and MW radiances are defined differently. Adjusting the UTH definition such that it is consistent for both IR and MW measurements is a main goal of this study.

Another shortcoming of the traditional UTH definition arises when UTH derived from satellite instruments is to be compared to UTH from climate model simulations. In order to obtain the UTH of model atmospheres, radiative transfer simulations have to be performed to calculate the Jacobians needed for the weighting of RH. Thus, a new UTH definition should be based on a more fundamental characteristic of the atmosphere in order to simplify its calculation and avoid the detour via radiative transfer simulations.

A third problem of UTH definition poses the fact that the BT in the UTH channels is not solely controlled by RH, but also by other factors like atmospheric temperature. These effects become crucial when long time series of UTH are analysed and trends are determined. This problem will be further investigated and discussed in Chapter 4.

2.2 Satellite instruments

This section gives an overview of the satellite instruments used in this thesis: The High-Resolution Infrared Radiation Sounder (HIRS), the Special Sensor Microwave Temperature - 2 (SSMT-2), the Advanced Microwave Sounding Unit - B (AMSU-B) and the Microwave Humidity Sounder (MHS). They are used in two different ways: On the one hand, their measurements are simulated with a radiative transfer model in the course of the development of the new UTH definition in Chapter 3. On the other hand, "real" measurements of these instruments build the basis for the new climate data records of UTH described in Chapter 5.

2.2.1 Microwave instruments: MHS, AMSU-B and SSMT-2

Three different microwave sensors are considered in this study: SSMT-2, AMSU-B and its successor MHS. All of them are passive microwave radiometers operating on polar-orbiting satellites.

The three instruments have a very similar design. All of them have five spectral channels, three of them located around the 183.31 GHz water vapour absorption line at 183.31 ± 1 GHz, 183.31 ± 3 GHz and 183.31 ± 7 GHz, respectively. Here, the $\pm$ indicates that the channels have two side bands around the centre frequency. An exception is the H5 channel of MHS, which only has one band at $183.31 + 7$ GHz. The three channels provide information on the humidity in the troposphere in different altitude regions. The channel used to observe UTH is the 183.31 ± 1 GHz channel, which has been introduced in Section 2.1.2. It has a total bandwidth of 1 GHz and is called channel H3 for MHS, channel 18 for AMSU-B and channel 2 for SSMT-2 (Robel et al., 2009; WMO-OSCAR, 2019).

MHS, AMSU-B and SSMT-2 are cross-track scanning instruments, meaning that they scan the Earth along the direction perpendicular to the subsatellite-track. Table 2.1 provides

an overview of the scanning properties of the three instruments. For MHS, each scan line consists of 90 Earth views, 45 on each side of the sub-satellite point. Each scan covers about 50° on both sides of the sub-satellite point, resulting in a swath width of 2180 km for a nominal satellite altitude of 850 km. The exact viewing angles range from 0.55° (from nadir) to 48.95° in steps of 1.1°. With an antenna beamwidth of 1.1° the ground footprint at the innermost scan position is circular with a diameter of 16 km. Towards the swath edges it becomes elliptical and reaches a size of 51.6 x 26.9 km at the outermost scan position. The scanning geometry of AMSU-B is almost identical, except from the exact viewing angles, which slightly differ from those of MHS (Table 2.1). SSMT-2 has different scanning properties than AMSU-B and MHS. It scans the Earth in only 28 views but has a larger beam width of 3.7 °, which results in a larger nadir footprint diameter of 48 km.

Table 2.1: Basic scanning properties of SSMT-2, AMSU-B and MHS (Robel et al., 2009; WMO-OSCAR, 2019). Note that the numbers given for SSMT-2 are only valid for channel 2 since the beamwidth changes between the instrument channels.

Instrument	swath width [km]	nominal beam width [°]	nadir footprint diameter [km]	number of Earth views	innermost viewing angle [° from nadir]	outermost viewing angle [° from nadir]
SSMT-2	1500	3.7	48	28	1.5	40.5
AMSU-B	2250	1.1	16	90	0.55	48.95
MHS	2180	1.1	16	90	0.555556	49.444396

2.2.2 Infrared instrument: HIRS

The High-Resolution Infrared Radiation Sounder (HIRS) is a cross-track scanning infrared radiometer with 20 frequency channels covering a spectral range from 0.69 to 15 μm. Channel 12 is designed to observe water vapour in the upper troposphere and thus to derive UTH. It has a spectral bandwidth of approximately 0.45 μm (2998 GHz) and is centred at 6.72 μm for HIRS/2, the earliest version of the instrument. When the instrument was upgraded from HIRS/2 to HIRS/3 with the launch of the satellite NOAA15 in 1998, the spectral response function of the channel changed and its centre wavelength moved to 6.52 μm (Shi and Bates, 2011). It is important to note that only the 6.72 μm channel of the HIRS/2 instrument probes a similar altitude region of the atmosphere as the 183.31 ± 1 GHz of the microwave sounders. As this thesis attempts to combine both microwave and infrared measurements, the newer instrument generations HIRS/3 and HIRS/4 are not considered.

HIRS scans through 56 Earth views and has a total swath width of approximately 2240 km. The instrument viewing angles range from 0.9° to 49.5° from nadir, in steps of 1.8°. With a field of view of 1.25° the footprint at the Earth's surface has a size of 17.7 x 17.7 km at the innermost scan position and increases to 59.5 x 30.4 km at the outermost scan position (NOAA CLASS webpage).

2.2.3 Polar orbiting satellites

All instruments used in this study are operating on satellites in a sun-synchronous near-polar orbit, often referred to simply as polar orbit. Satellite orbits of this kind are characterized by a low altitude (about 850 km) and an inclination against the equatorial plane that is close to 90°. As a result of this high inclination, the satellite has a near-polar orbit, meaning that it nearly passes both poles in every orbit. As the Earth rotates around its own axis, the satellite swath covers different parts of the Earth in each of its 14 orbits per day, so that eventually global coverage is achieved (EUMETSAT-webpage, 2018).

Furthermore, the orbits of the satellites considered in this thesis are sun-synchronous. This means that - in contrast to a fixed polar orbit - the angle between the orbital plane and the sun remains constant. The difference between a fixed polar orbit and a sun-synchronous orbit is illustrated in Figure 2.6. To obtain a sun-synchronous orbit, one uses the fact that every orbit around the Earth is subject to a torque because of the deviations of the Earth's shape from a perfect sphere. This causes a precession of the orbit. The precession can be exploited by choosing the inclination in such a way that the orbit precesses exactly once within each year (Buehler, 2016). As a consequence, the satellites pass a given point on Earth always at the same local solar time and are therefore typically characterized by their equator crossing time. However, maintaining a sun-synchronous orbit over a long period of time requires active corrections of the satellite position. As many of the satellites in this study lack such corrections, the equator crossing time slowly drifts over the course of a satellite mission.

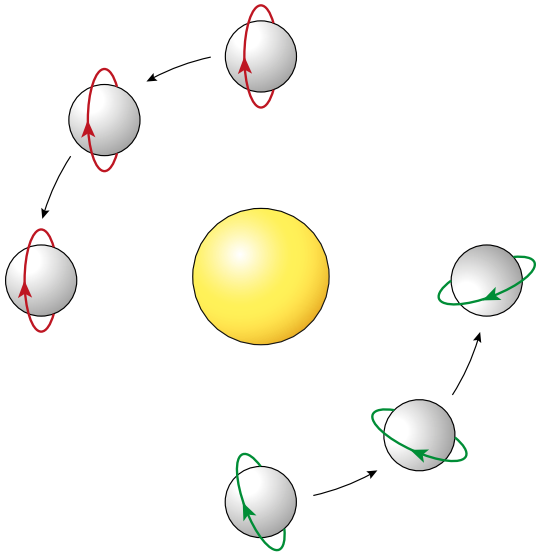

Figure 2.6: Illustration of a fixed polar orbit (red) and a sun-synchronous polar orbit (green). Figure courtesy Oliver Lemke.

2.3 Climate data records (CDRs)

Satellite observations are an important tool to evaluate climate model simulations, because they are the only observations that both cover a long period of time and provide global coverage. However, the conversion of raw satellite data into consistent long-term Climate Data Records (CDRs) is challenging and involves a multitude of intermediate steps.

Particularly, difficulties arise from a deterioration of the instruments and their calibration targets. These deteriorations can lead to artificial trends in the observations, which conceal the actual natural trend. Therefore, the calibration process has to be re-analysed and improved in a step called recalibration. Another problem is that measurements from several instruments have to be combined to create long data records. Operational meteorological satellites have been continuously launched since almost 40 years and are therefore of great interest for climate research. However, the problem with those satellites is that they were originally not designed for climate monitoring but for numerical weather prediction. As a consequence, there are discontinuities between the measurements of successive satellite missions, called "intersatellite-biases". To get a homogeneous time series free of these biases, the instruments have to be intercalibrated (Schulz and Schüller, 2011).

After re- and intercalibrating the instruments an intermediate data product is created: the Fundamental Climate Data Record (FCDR). It is a so-called level 1 (L1) dataset and contains sensor data, such as radiances or brightness temperatures, for every pixel in the satellite swath. A more precise definition of an FCDR is given by Merchant (2018): "An FCDR consists of a continuous, harmonised record of calibrated, geolocated uncertainty-quantified sensor observations in geophysical units (such as radiance), together with all ancillary and underlying data used to calibrate the observations and estimate uncertainty".

This thesis focuses on the last step in the CDR processing: the transformation of FCDR brightness temperatures into a higher-level product, the CDR. CDRs are sometimes also referred to as Thematic Climate Data Records. They contain the geophysical variables that are derived from the FCDR radiances, as for instance UTH or Sea Surface Temperature. CDRs can be either level 2 (L2) or level 3 (L3) data sets, which differ only in their spatial and temporal resolution. In a level 2 dataset the resolution of the FCDR is maintained, whereas a level 3 dataset is mapped to a uniform spatial and temporal grid. In this work a level 3 CDR of UTH is created.

2.4 Uncertainties and their propagation

A novelty of the UTH CDR created in the framework of this thesis is the fact that it contains an estimation of the measurement uncertainty. This uncertainty has to be propagated from FCDR level to CDR level. Some basic metrological concepts needed to understand this propagation are introduced in the following.

First, it is important to understand the difference between the terms error and uncertainty. This can be done by considering the result of a measurement. If it were possible to perform a perfect measurement, one would obtain the true value of the measurand. However, in reality a measurement is never perfect. Thus, the measured values are always an estimate of the true value (FIDUCEO-webpage, 2018). According to the "Guide to the expression of uncertainty in measurement (GUM, 2008)", the term error is defined as the "result of a measurement minus a true value of the measurand". The error can be split up into systematic error and a random error. The systematic error is the "mean that would result from an infinite number of measurements of the same measurand carried out under repeatability conditions minus a true value of the measurand" (GUM, 2008). The random error is the error minus the systematic error.

Since the true value of the measurand is unknown, the error of a measurement is also unknowable. However, the error in the result of a particular measurement can be described as a draw from a probability distribution. This probability distribution is described by the uncertainty associated with the measurement. A frequently used quantity is the standard uncertainty, which is the standard deviation of the probability distribution (FIDUCEO-webpage, 2018).

In many applications it is necessary to determine the uncertainty u of a quantity y, which is not measured directly, but determined from m other quantities $x_1, x_2, ..., x_m$ through a functional relationship f. This can be done using the Law of the Propagation of Uncertainties. In its most general form it can be written as (GUM, 2008):

$$u(y) = \sqrt{\sum_{i=1}^{m} (\frac{\partial f}{\partial x_i})^2 \, u(x_i)^2 + 2 \sum_{i=1}^{m-1} \sum_{j=i+1}^{m} \frac{\partial f}{\partial x_i} \frac{\partial f}{\partial x_j} \, u(x_i) \, u(x_j) \, r(x_i, x_j)}, \tag{2.9}$$

where $u(x_i)$ are the uncertainties of the input quantities x_i. The partial derivatives of f with respect to the input quantities x_i describe the sensitivity of f to changes in x_i and are therefore sometimes called sensitivity coefficients. The correlation coefficient $r(x_i, x_j)$ characterizes the correlation between x_i and x_j. When the input quantities x_i are independent, the correlation coefficient r is zero and hence the second term under the square root disappears. Thus, the uncertainty $u(y)$ is generally larger when the input quantities are positively correlated.

CHAPTER 3

A new definition of Upper Tropospheric Humidity (UTH)

The established definition of UTH, which is based on the water vapour Jacobian of the particular instrument channel, has two major shortcomings. Firstly, it is not equal and hence not readily comparable for IR and MW measurements (Section 2.1.5). Secondly, to compare UTH derived from satellite measurements to UTH from climate model simulations a detour has to be made via radiative transfer simulations in order to obtain the Jacobians. To overcome these issues, the established definition of UTH has to be adapted. This chapter introduces a new definition, which is identical for both instrument types and based solely on the atmospheric humidity profile, so Jacobians are not required. This definition will be used to create a new UTH CDR in Chapter 5.

In the following, the overall concept of the new definition as well as the derivation of its optimal parameters are explained. Furthermore, the performances of UTH retrievals with the old and the new definition are compared.

3.1 A definition based on the water vapour overburden

The overall concept of the new UTH definition is similar to the traditional one (Section 2.1.5). UTH is still defined as a vertical average of RH, but the way of averaging changes. Instead of weighting RH with the channel-specific Jacobian, a regular (unweighted) average of RH is performed over a certain atmospheric layer (Figure 3.1), hereafter referred to as UTH layer. The definition of this UTH layer is based on an idea from Wu et al. (1993), which was already mentioned in Section 2.1.2. They showed that the atmospheric layer that contributes to the BT measured in the 6.7 μm channel is bounded by two characteristic water vapour columns. One possibility to explain this in an intuitive

way is Chapman's Law. It says that the radiation escaping the atmosphere approximately originates from the altitude at which the optical thickness reaches one, seen from the TOA downwards. As the radiation originates from an extended atmospheric layer rather than from one distinct level, one can infer that this layer is bounded by two characteristic optical thicknesses that are close to one. Since the optical thickness in a UTH channel is closely linked to the water vapour column, a UTH layer that is bounded by two water vapour overburdens should be able to reflect the varying altitude of the emission layer, similar to the water vapour Jacobian in the traditional UTH definition (Section 2.1.5). This is an important requirement for the BT transformation method (Equation 2.7) to work.

Using this idea, the new UTH (UTH_{new}) can be defined as the RH averaged over an atmospheric layer that is bounded by two altitude levels $z(IWV_1)$ and $z(IWV_2)$, at which the integrated water vapour (IWV) above exceeds two fixed thresholds IWV_1 and IWV_2 (Figure 3.1):

$$UTH_{\mathrm{new}}(\theta) = \frac{1}{z(IWV_1(\theta)) - z(IWV_2(\theta))} \int_{z(IWV_2(\theta))}^{z(IWV_1(\theta))} RH(z)dz. \tag{3.1}$$

Both IWV thresholds and UTH_{new} depend on the satellite viewing angle θ, because the altitude of the emission level changes with θ. The idea is to use the same IWV thresholds for both MW instruments and HIRS/2, so the new definition is identical for both instrument types. The thresholds are determined with a simple optimisation procedure, which is described in more detail in the next section.

Note that the new UTH definition does not change the fact that the BT might be influenced by other factors than the RH, which is particularly relevant when climate trends are investigated. This general problem of the BT transformation method (Equation 2.7) will be discussed in more detail in Chapter 4.

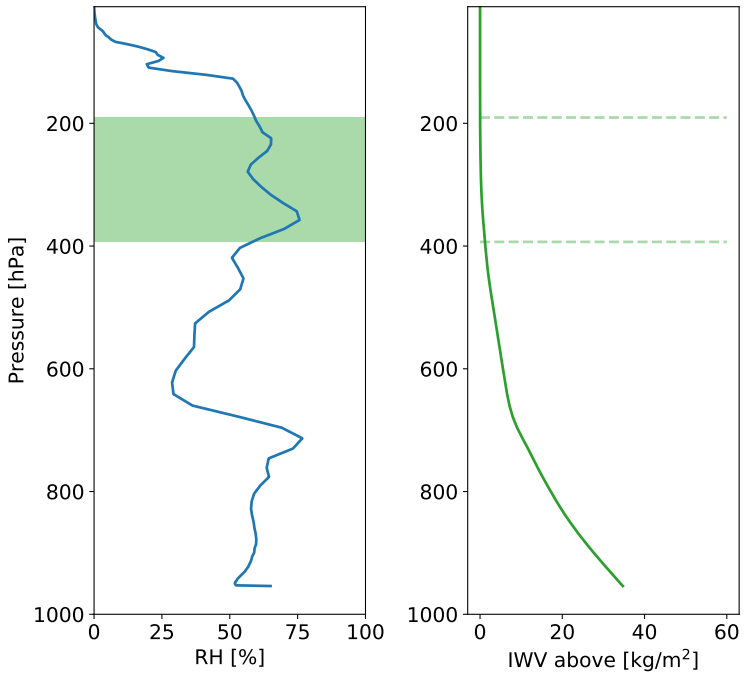

Figure 3.1: Example of an atmospheric profile of RH (left panel) and the IWV above every altitude level (right panel). The levels at which the overlying IWV exceeds the two characteristic thresholds are indicated by dashed lines. UTH is calculated as vertical average of RH in the layer between these two levels (green shading). Note that the example atmosphere shown here is the same as in Figure 2.4.

3.2 Determination of water vapour thresholds and regression coefficients

The following section describes the procedure to find the most suitable IWV thresholds for the new UTH definition. At the same time, the coefficients a and b that are needed to scale a measured BT to UTH are determined. The following steps are performed for each of the three instruments AMSU-B, MHS and HIRS:

1. Calculate UTH_{new} for a set of training atmospheres, starting with an arbitrary pair of IWV thresholds.

2. Use a radiative transfer model to simulate BTs measured in the UTH channel of the instrument for all training atmospheres.

3. Plot ln(UTH_{new}) against BT for all training atmospheres and perform a linear regression.

4. Repeat 1. and 3. for different pairs of IWV thresholds in the UTH definition to find the pair, for which the linear relationship is most pronounced.

Steps 1 to 3 are performed separately for every viewing angle of the instrument. Note that the new definition is only of value if this procedure reveals that the same IWV thresholds can be used for IR and MW instruments at a given viewing angle. The following sections describe the approach outlined above in more detail.

3.2.1 ECMWF atmospheres as training data

The set of training atmospheres used to determine IWV thresholds and regression coefficients was developed by Eresmaa and McNally (2014). It consists of diverse atmospheric profiles selected from the 137-level operational short-range forecast of the European Centre for Medium-range Weather Forecasts (ECMWF). The complete data set includes five subsets, each selected to maximise the variability of a particular atmospheric parameter. The subset chosen for this study consists of 5000 atmospheric profiles of nine different atmospheric variables given on a 137-level pressure grid. It is sampled such that it covers the variability of specific humidity in the atmosphere as well as possible. In contrast to earlier datasets, a special focus was also put on a homogeneous geographical distribution of the sampled profiles. Since the UTH CDR will only cover the tropical region, only tropical atmospheres are selected from the data set, leaving a subset of 2812 atmospheres. This set of atmospheres is used to determine the IWV thresholds and regression coefficients. It will be referred to as the Eresmaa data set hereafter.

To calculate the "true" UTH (UTH_{true}) of a given training atmosphere (step 1 in Section 3.2), the two characteristic IWV thresholds are needed (Equation 3.1). Since these are still to be determined, an arbitrary pair of thresholds is used. The IWV above every altitude level z in the profile is calculated. This is done by integrating the mass density of water vapour ρ from the level z upwards to the TOA:

$$IWV(z) = \int_{z}^{\infty} \rho(z')dz'. \tag{3.2}$$

The altitude levels at which $IWV(z)$ exceeds the two IWV thresholds are determined. In the layer between these two levels a vertical average of the RH profile is calculated. Note that since the RH values are given at discrete model levels, they have to be weighted with the thickness of the corresponding model layers.

3.2.2 Radiative transfer simulations with ARTS

To test the new UTH definition, the BTs measured in infrared and microwave UTH channels are simulated for all Eresmaa atmospheres with a radiative transfer model (step 2 in Section 3.2). Here, the microwave instruments AMSU-B and MHS and the infrared instrument HIRS are chosen. BTs are simulated for all existing viewing angles of the respective instruments. Additionally, VMR Jacobians (Section 2.1.4) are needed to calculate UTH according to the traditional definition. They are also simulated for all instruments and viewing angles.

For the radiative transfer simulations only the information on temperature, humidity and ozone concentration are extracted from the Eresmaa data set. Additionally, the concentrations of nitrogen and oxygen are needed. As they are not provided in the data set, it is assumed that they are constant throughout the atmosphere. Volume mixing ratios (VMRs) of 0.7808 and 0.2095 are used for nitrogen and oxygen, respectively. As UTH can only be derived from clear-sky BTs (Section 2.1.5), only clear-sky atmospheres are used for the simulations. This is done by ignoring all information on clouds provided by the dataset.

The simulations are performed with The Atmospheric Radiative Transfer Simulator (ARTS) (Buehler et al., 2005; Eriksson et al., 2011). ARTS is a line-by-line radiative transfer model for the millimetre and sub-millimetre spectral range. It works with arbitrary frequency grids and can hence be used to simulate any satellite sensor operating in this spectral range. The absorption lines in the spectral range of the respective channel are taken from spectral line catalogues. In this study, the HIgh-resolution TRANsmission molecular absorption database (HITRAN) catalogue (Rothmann et al., 2012) is used. For the different atmospheric absorbers it contains a set of parameters describing the line properties and their dependence on the atmospheric conditions. These parameters are needed to calculate the absorption coefficients at a given frequency for a given atmospheric state. In the simulations performed here, scattering processes are neglected since only clear-sky atmospheres are used.

Generally, two steps are required to simulate the measurement of a satellite instrument for a given atmosphere with a line-by-line radiative transfer model. Firstly, TOA radiances are calculated for many frequencies inside the spectral range of the respective channel by simulating the radiative transfer through the atmosphere. Secondly, the radiances are convolved with the spectral response function of the specific channel (Equation 2.1).

For the simulations in this work, two existing ARTS setups are adapted. The setup used to simulate channel 12 of the HIRS instrument is based on a method developed by Buehler et al. (2010). The basic idea of this method is that the channel radiances can be calculated as a weighted mean of the radiances at some representative frequencies. This allows a very efficient simulation, because the number of frequencies can be significantly reduced compared to a simulation with an "ordinary" frequency grid. The exact form of the spectral response function of channel 12 differs among the individual HIRS/2 instruments. However, it is assumed that these differences are sufficiently small to not have an influence on the determined IWV thresholds. Thus, BTs are simulated only for one specific instrument. Here, the HIRS/2 instrument on board NOAA12 is used, because it has been used as a reference in earlier studies (Shi and Bates, 2011). To simulate this specific instrument channel, 16 representative frequencies between 41.5 THz (7.2 μm) and 46.6 THz (6.4 μm) are used. Buehler et al. (2010) showed that the resulting accuracy of BT is better than 0.05 K.

In contrast to the HIRS simulations, an equidistant grid spacing can be used for the MW simulations, since the spectral complexitiy in the MW region is significantly lower than in the IR region. Furthermore, the spectral response function can be approximated by a rectangle. The number of frequencies is chosen according to Bobryshev (2015) to achieve an accuracy better than 0.01 K. For the 183.31±1 GHz channel of AMSU-B (MHS) the frequency grid consists of 40 (24) frequencies between 182.2 GHz and 184.4 GHz. Note that channel 20 (183.31±7 GHz) BTs of AMSU-B are also simulated, because they are needed to remove surface-contaminated measurements. Since this is their only application, the simulation is not described here in more detail.

Even though only tropical atmospheres are used here, the simulated instruments might see the Earth's surface under extremely dry conditions or above high mountains. These extreme cases are filtered out using the same methodology as Buehler and John (2005): profiles are discarded if the BT in the 183.31±7 GHz channel of AMSU-B is not warmer than that in the 183.31±1 GHz channel. Under clear-sky conditions this only occurs when

both channels see the surface. For all other cases, the BT in the 183.31$\pm$7 GHz channel is warmer, because the emission originates from lower tropospheric levels. Due to the similarity of the HIRS and AMSU-B UTH channels, it is assumed that in the HIRS channel surface contamination occurs for exactly the same profiles than in the AMSU-B channel.

3.2.3 Optimizing water vapour thresholds

The simulated BTs can now be used together with the true UTH of the training atmospheres, to test how well the linear relationship between BT and ln((UTH)) is defined (step 3 in Section 3.2). For all instruments and viewing angles, the logarithm of UTH_{true} of all training profiles is plotted against the simulated BT, similar to what is shown in Figure 2.5. A linear regression is performed using the Theil-Sen method (Theil, 1950; Sen, 1968), which is very robust against outliers. The principal idea of this method is that the slope of the regression line is the median of the slopes of all lines through pairs of points. To get a measure of how well a linear model describes the relation between ln(UTH) and BT, the root-mean-square deviation (RMSD) of all data points from the regression line is calculated. To determine the most suitable pair of IWV thresholds, the procedure described above is repeated for many different pairs of thresholds (step 4 in Section 3.2). For every instrument and viewing angle, the pair that results in the lowest RMSD is chosen to be the most suitable one.

3.3 Water vapour thresholds and regression coefficients

Figure 3.2 shows the most suitable IWV thresholds for HIRS, AMSU-B and MHS as a function of viewing angle. As one would expect, the threshold for the MW instruments AMSU-B and MHS are virtually identical, since the UTH channels of the two instruments have identical characteristics (Section 2.2). The two instruments only differ in the exact angular positions of the individual views. More importantly, the IWV thresholds of the MW instruments and HIRS are also very similar. Therefore, it is possible to find a compromise between HIRS and MW thresholds by taking the average of the two, as indicated by the orange dashed line in Figure 3.2. Using these compromise thresholds ensures that the UTH definition is identical for HIRS and the MW sensors.

From Figure 3.2 it is obvious that the thresholds depend on the instrument viewing angle. When the viewing direction of the satellite moves away from nadir, the thresholds

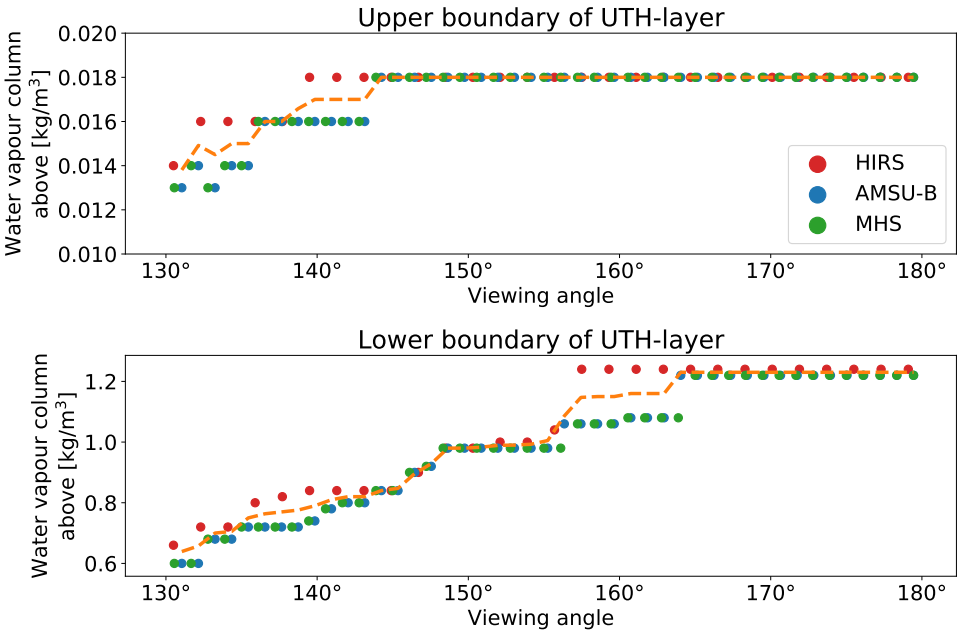

Figure 3.2: IWV thresholds defining the upper boundary (upper panel) and lower boundary (lower panel) of the UTH layer for HIRS (red), AMSU-B (blue) and MHS (green) at all viewing angles, where 180° corresponds to the nadir view. The orange dashed line indicates the mean of the thresholds determined for HIRS and the MW instruments, which is used for the final compromise definition.

become smaller. As the path length through the atmosphere increases as the viewing angle moves away from nadir, a given optical thickness or integrated water vapour along the sensor's line of sight is reached in higher altitudes. A higher altitude corresponds to a smaller IWV above, because the IWV above is always defined along the vertical direction. For the most off-nadir view of $130°$, for example, the path length is increased by a factor of $\frac{1}{-\cos(130°)} \approx 1.56$ with respect to the nadir view. Hence, a given integrated water vapour along the sensor's line of sight ($IWV_{\mathrm{off-nadir}}$) is reached at an altitude, at which the IWV above is $\frac{1}{1.56} = 0.64$ times the $IWV_{\mathrm{off-nadir}}$. Thus, the absolute difference between $IWV_{\mathrm{off-nadir}}$ and IWV above increases with increasing IWV above. This is why the absolute change of the IWV threshold with the viewing angle is stronger for the threshold defining the lower boundary of the UTH layer (Figure 3.2).

Finally, steps 1 and 3 from Section 3.2 are performed using the compromise thresholds from above and the regression intercept a and slope b are determined for every instrument and viewing angle. Figure 3.3 shows the regression for the nadir view of HIRS and

AMSU-B. The corresponding nadir regression coefficients are listed in Table 3.1. The coefficients for MHS are very similar to those of AMSU-B, which is why the regression for MHS is not shown separately in Figure 3.3. Coefficients for all instruments and viewing angles are listed in Table 7.1 in the Appendix (Section 7.1). The UTH that is retrieved from BT with these coefficients will be called fitted UTH (UTH_{fitted}) from here on.

For comparison, the same regression is shown for UTH defined in the traditional way using the fractional water vapour VMR Jacobian ($UTH_{\mathrm{traditional}}$) in Figure 3.4. The regression coefficients are also listed in Table 3.1. It is apparent that the slope of the regression line is more negative for UTH_{new} than for $UTH_{\mathrm{traditional}}$ for both MW and HIRS BTs, meaning that UTH_{new} decreases faster with increasing BT than $UTH_{\mathrm{traditional}}$. A closer comparison of the regression lines in Figure 3.3 and Figure 3.4 reveals that UTH_{new} and $UTH_{\mathrm{traditional}}$ are similar for moist atmospheres (low BTs), but UTH_{new} is lower than $UTH_{\mathrm{traditional}}$ for dry atmospheres (high BTs). A possible explanation for this is the way the RH profile is averaged in the two definitions. While all altitude levels are weighted equally to obtain UTH_{new}, the RH profile is weighted with the Jacobian to obtain $UTH_{\mathrm{traditional}}$. Generally, the shape of the Jacobian is more complex in dry atmospheres than in moist atmospheres. Instead of one defined peak, the Jacobian often has several smaller uneven peaks for dry atmospheres (Figure 2.3). These peaks are often located at the top of atmospheric layers that are moister than the surrounding, since the emission from these layers to space is stronger. Thus, the Jacobian tends to give higher weights to moist atmospheric layers than to dry layers. This could explain why $UTH_{\mathrm{traditional}}$ is larger than UTH_{new} for dry atmospheres.

Table 3.1: Scaling coefficients a and b for the nadir view of the instruments HIRS, AMSU-B and MHS for the new and the traditional definition of UTH.

Definition of UTH	Instrument	a (intercept)	b (slope)
New	AMSU-B	22.4942	-0.0950
	MHS	22.5022	-0.0951
	HIRS	29.6040	-0.1260
Traditional	AMSU-B	18.3820	-0.0778
	MHS	18.3889	-0.0779
	HIRS	25.6810	-0.1093

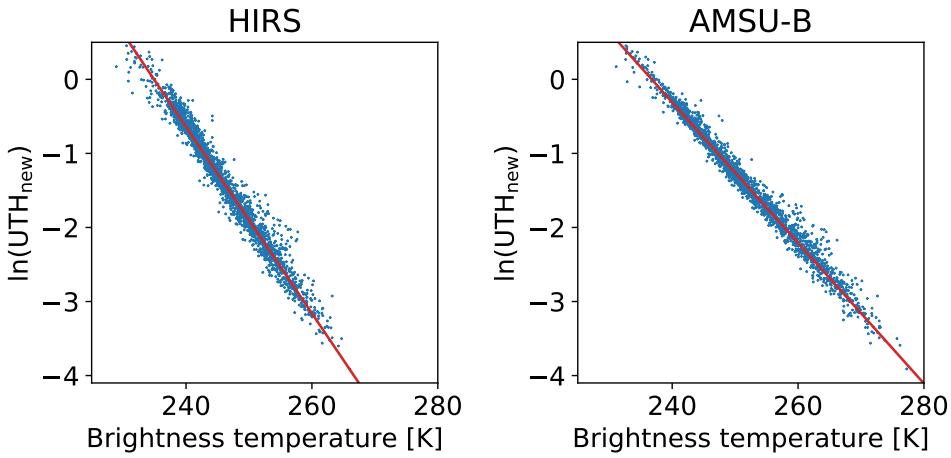

Figure 3.3: Logarithm of nadir UTH defined with the new method (UTH_{new}) versus nadir BT of HIRS (left panel) and AMSU-B (right panel) for the Eresmaa data set. The linear regression that is performed to obtain the parameters a and b needed for the transformation from BT to UTH is shown in red.

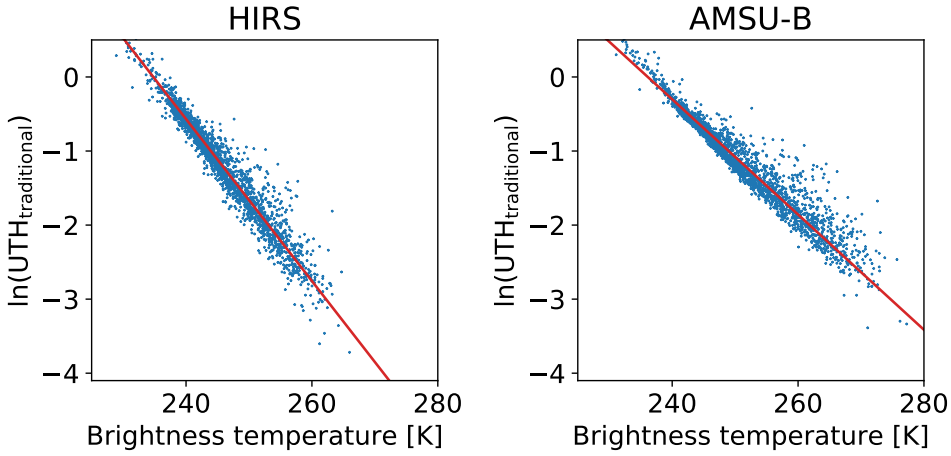

Figure 3.4: Same as Figure 3.3 for the traditional UTH definition based on the fractional water vapour VMR Jacobian.

3.4 Evaluation of the retrieval performance

To give an impression of the performance of the UTH retrieval with the new UTH definition, Figure 3.5 shows UTH_{fitted} versus UTH_{true} for the nadir views of AMSU-B and HIRS. For comparison, the same is shown for the retrieval using $UTH_{\mathrm{traditional}}$ based on the fractional water vapour VMR Jacobian in Figure 3.6. Again, results for MHS are not presented separately, because they are very similar to those for AMSU-B. The scatter of the data points seems to be approximately equal for traditional and new definition, indicating that the retrieval accuracy does not suffer from the new definition.

To investigate the performance in more detail, the difference ΔUTH between UTH_{fitted} and UTH_{true} is calculated for all training atmospheres:

$$\Delta UTH = UTH_{\mathrm{fitted}} - UTH_{\mathrm{true}}. \tag{3.3}$$

Following Buehler and John (2005), the retrieval bias is defined as the mean of ΔUTH of all training atmospheres ($\overline{\Delta UTH}$) and the retrieval standard deviation is the standard deviation of ΔUTH ($\sigma_{\Delta UTH}$). In a similar way, relative retrieval bias ($\overline{\Delta UTH_{\mathrm{rel}}}$) and relative retrieval standard deviation ($\sigma_{\Delta UTH_{\mathrm{rel}}}$) are defined. These are based on the relative difference between UTH_{fitted} and UTH_{true}:

$$\Delta UTH_{rel} = \frac{UTH_{\mathrm{fitted}} - UTH_{\mathrm{true}}}{UTH_{\mathrm{true}}}. \tag{3.4}$$

To get more detailed retrieval statistics, the data points are aggregated in 10 % RH bins of the true UTH. Retrieval bias and standard deviation are calculated separately for each bin and shown in Figure 3.7. Note that UTH values above 80% RH are very rare (Figure 3.5 and 3.6) and the retrieval performance in the corresponding bins is of less importance. The retrieval biases for AMSU-B and HIRS are very similar. Using the new definition, the absolute retrieval bias is close to zero for UTH values below 40% RH and increases to about -4% RH for UTH values between 40% RH and 80% RH. The relative bias is between -5 $\%$ and 0.5 $\%$ in all UTH bins below 80% RH. These biases are slightly larger than for the retrieval with the traditional definition for UTH values above 40% RH and slightly smaller for UTH values below 40% RH.

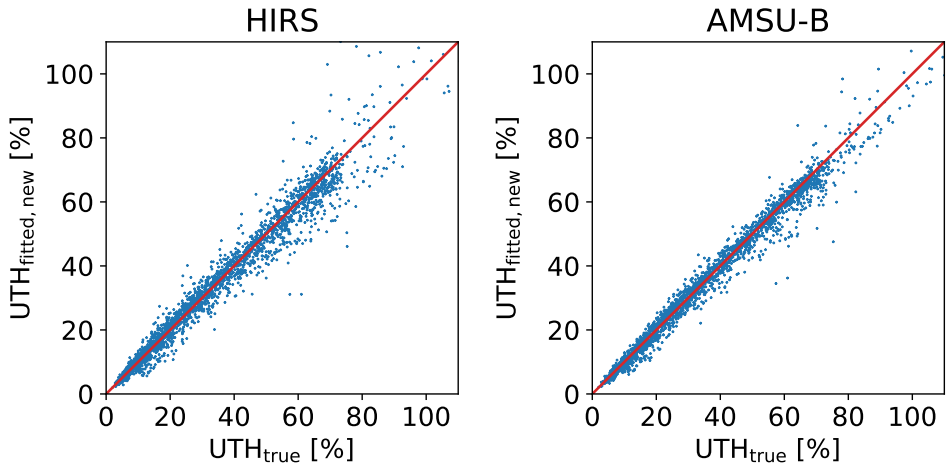

Figure 3.5: Fitted nadir UTH for HIRS (left panel) and AMSU-B (right panel) versus true nadir UTH for the Eresmaa data set. UTH is calculated according to the new definition based on the water vapour overburden. The scatter of the data points is not stronger than for the traditional definition (Figure 3.6), indicating that the retrieval performance does not suffer from the new definition.

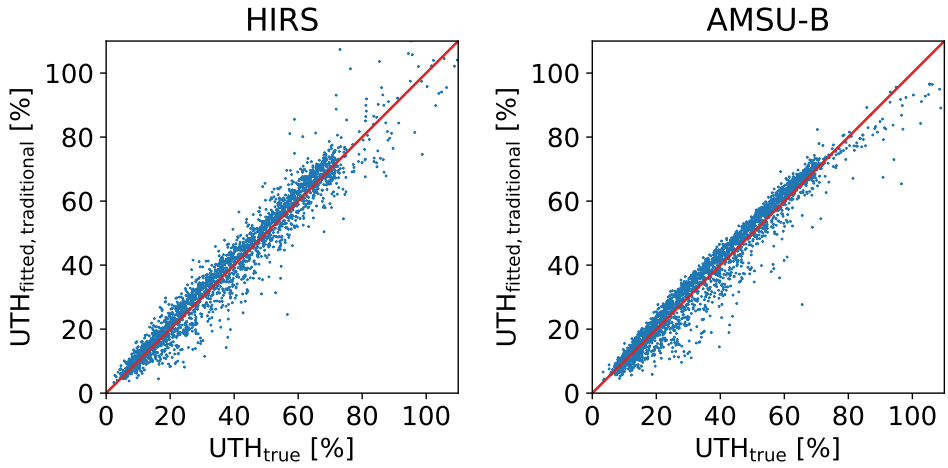

Figure 3.6: Same as Figure 3.5 for the traditional UTH definition based on fractional water vapour VMR Jacobians.

The retrieval standard deviation is generally smaller for the AMSU-B retrieval than for the HIRS retrieval. Using the new UTH definition, $\sigma_{\Delta UTH}$ in the 0-10% UTH bin is approximately 1% RH for both AMSU-B and HIRS and continuously increases to approximately 6% RH for AMSU-B and 11% RH for HIRS at 80-90% UTH. In relative units, the retrieval standard deviation of the AMSU-B retrieval decreases from about 12-13% at

UTH values below 20% RH to about 6-8% for UTH values above 40% RH. For HIRS, $\sigma_{\Delta UTH_{\mathrm{rel}}}$ is generally about 2-4% larger than for AMSU-B. Compared to the retrieval with the traditional UTH definition, standard deviations are generally lower for UTH below 60% RH and slightly higher for UTH above 60% RH.

Overall retrieval biases and standard deviations for both instruments and definitions are listed in Table 3.2. It can be summarized that the new UTH definition results in a smaller retrieval bias for HIRS, but a larger retrieval bias for AMSU-B. With regard to the standard deviation, the retrieval with the new UTH definition performs better for both instruments.

John (2016) has shown that a better performance is achieved with the traditional definition when using RH Jacobians instead of VMR Jacobians. With this improved version of the traditional definition the retrieval performance might be better than with the new definition. However, it should be pointed out that the key advantages of the new definition over the traditional one are the comparability of HIRS and MW UTH and the fact that no radiative transfer simulations are needed in order to calculate the UTH of a given model atmosphere. In return, a slightly reduced retrieval accuracy compared to the traditional definition is acceptable.

Table 3.2: Absolute and relative overall retrieval bias and retrieval standard deviation for the retrieval with the new UTH definition and the traditional UTH definition, respectively.

Definition of UTH	**Instrument**	$\overline{\Delta UTH}$ **[% RH]**	$\overline{\Delta UTH_{\mathrm{rel}}}$ **[%]**	$\sigma_{\Delta UTH}$ **[% RH]**	$\sigma_{\Delta UTH_{\mathrm{rel}}}$ **[%]**
New	AMSU-B	-0.6	-1.4	3.2	9.5
	HIRS	-0.4	-0.7	4.8	12.6
Traditional	AMSU-B	0.2	0.6	4.4	14.3
	HIRS	0.5	2.1	4.8	15.8

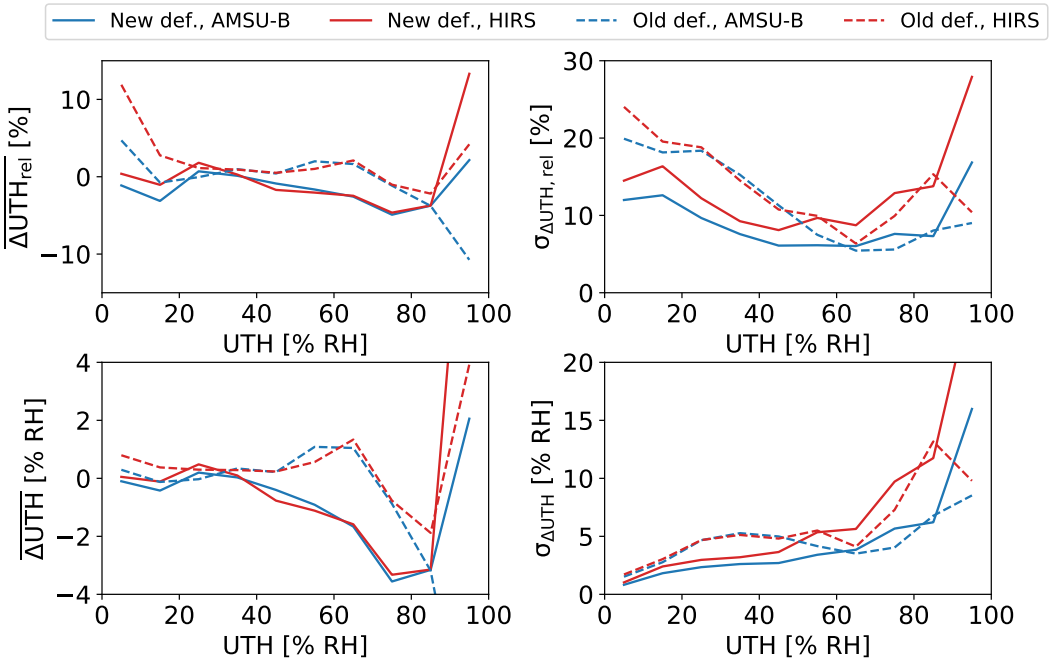

Figure 3.7: Retrieval bias (left panels) and retrieval standard deviation (right panels) in relative units (upper panels) and absolute units (lower panels) for retrievals using the new UTH definition (solid lines) and the traditional definition (dashed lines) for AMSU-B (blue) and HIRS (red).

CHAPTER 4

The behaviour of UTH in a warming climate

As already stated in Section 2.1.5, a general problem of the UTH scaling method is that the BT in a UTH channel is not solely controlled by RH, but also by other factors like the atmospheric temperature profile. This becomes particularly important when one of the factors influencing BT changes in a warming climate, because this can lead to a trend in UTH that is actually not caused by a trend in RH. If this is not considered, wrong conclusions are drawn about the evolution of RH in a warming climate.

One important factor influencing BT is the shift of the emission layer to higher altitudes as the atmosphere warms. Using a set of idealised atmospheric profiles, the first part of this chapter demonstrates that this upward shift influences IR and MW BTs differently. In the second part, more realistic profiles from a simulation with a global climate model are used to show that the shifting emission layer results in artificial trends in the time series of IR UTH. The chapter is concluded by a simple correction for the tropical mean IR UTH and an outlook on how the problem could be solved in future studies.

4.1 Impact of a shifting emission layer on IR and MW brightness temperatures

Here, a set of idealised atmospheric profiles is used to investigate how the BT in the IR and MW UTH channels evolves in a warming climate, in which the relative humidity stays approximately constant. These atmospheric profiles are shown in Figure 4.1. They were obtained via simulations with a one-dimensional radiative-convective equilibrium (RCE) model, performed by Kluft et al. (in review). RCE is an idealisation of the climate system in which convection balances the atmospheric heat loss due to radiative cooling

(Wing et al., 2017). The RCE profiles used here result from different atmospheric CO_2 concentrations ranging from one forth of today's CO_2 concentration ($0.25xCO_2$) to eight times today's CO_2 concentration ($8xCO_2$). Temperature and water vapour VMR of the atmospheres increase with increasing CO_2 concentration in such a way that the RH, which decreases exponentially with pressure, stays constant at each pressure level. Only in the levels above 100 hPa RH slightly increases with increasing CO_2 concentration. These changes in RH are assumed to be sufficiently small and in regions high enough to have no significant impact on the BT measured in a UTH channel. Thus, these profiles are suitable for investigating how the measured BT changes when the atmosphere warms and the RH profile stays constant.

Figure 4.2 shows BTs for the AMSU-B 183.31±1 GHz channel and the HIRS 6.7 µm channel that were simulated with ARTS for the six different RCE profiles shown in Figure 4.1. Both AMSU-B and HIRS BTs increase with increasing CO_2 concentration. This can be explained as follows: as the atmosphere warms and the water vapour concentration increases, the emission layer - and hence also the UTH layer - shifts to higher altitudes.

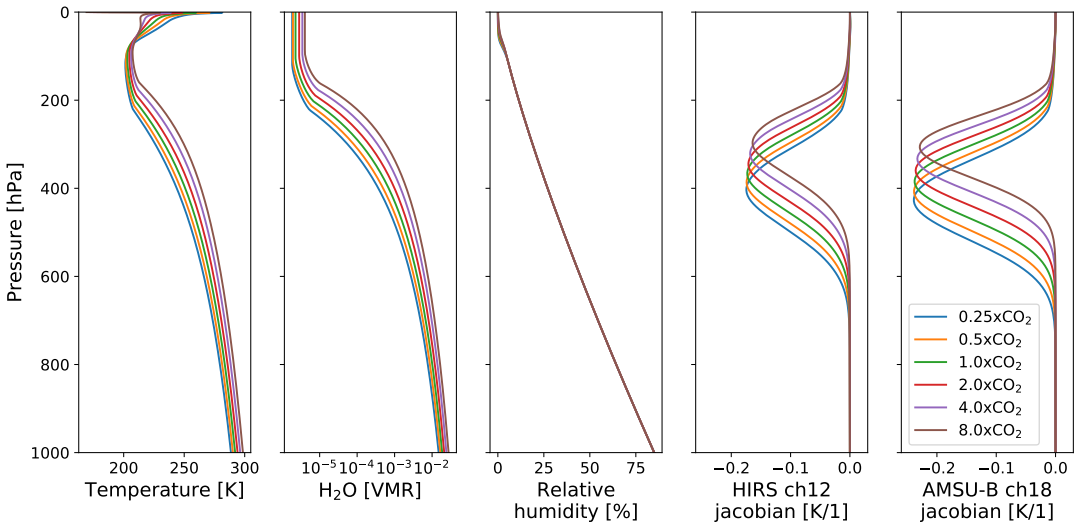

Figure 4.1: Atmospheric profiles of temperature (first panel) and water vapour VMR (second panel) from a one-dimensional radiative-convective equilibrium model simulation by Kluft et al. (in review) for different CO_2 concentrations ranging from one fourth of today's CO_2 concentration ($0.25xCO_2$) to eight times today's CO_2 concentration ($8xCO_2$). The relative humidity profile is kept fixed below the 100 hPa level (third panel). Fractional water vapour VMR Jacobians for the HIRS 6.7 µm channel and the AMSU-B 183.31±1 GHz channel are shown in the fourth and fifth panel, respectively.

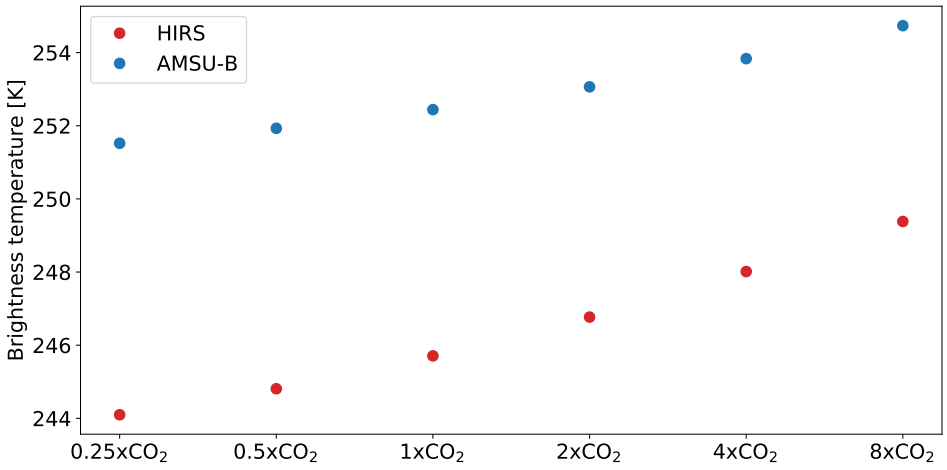

Figure 4.2: HIRS (red) and AMSU-B (blue) BTs simulated for the RCE profiles with six different CO_2 concentrations shown in Figure 4.1. Both HIRS and AMSU-B BTs increase with increasing CO_2 concentration, but the increase in HIRS BT from 0.25xCO_2 to 8xCO_2 is almost twice as big as in AMSU-B BT.

This upward shift in the emission layer is reflected by an upward shift of the peaks of the fractional water vapour VMR Jacobians shown in Figure 4.1. As the RH decreases with increasing altitude (Figure 4.1), it follows that the mean RH in the UTH layer decreases and the emitted BT increases (Equation 2.7). However, the BT increase in the HIRS channel is almost twice as big as the increase in the AMSU-B channel (Figure 4.2). As mentioned in Section 2.1.2, the two channels have different radiometric properties: While the HIRS channel includes a large amount of narrow absorption lines, the MW channel only includes the flanks of a single absorption line (Figure 2.1). To test whether these differences can explain the different evolution of BT in the HIRS and MW channels, BTs are simulated with high spectral resolution within the two channels.

The spectrally resolved BTs are shown in Figure 4.3 for the 0.5xCO_2 scenario and the 4xCO_2 scenario in both the IR and the MW UTH channels. It is apparent that the width of the absorption lines decreases as the atmosphere warms. This happens because the effect of pressure broadening becomes weaker as the emission level shifts to higher altitudes and hence lower pressures. At the flanks of the absorption lines and in the regions where the flanks of neighbouring lines overlap the decrease in line width leads to an increase in BT. This causes a large overall increase in BT in the HIRS channel. In the centres of

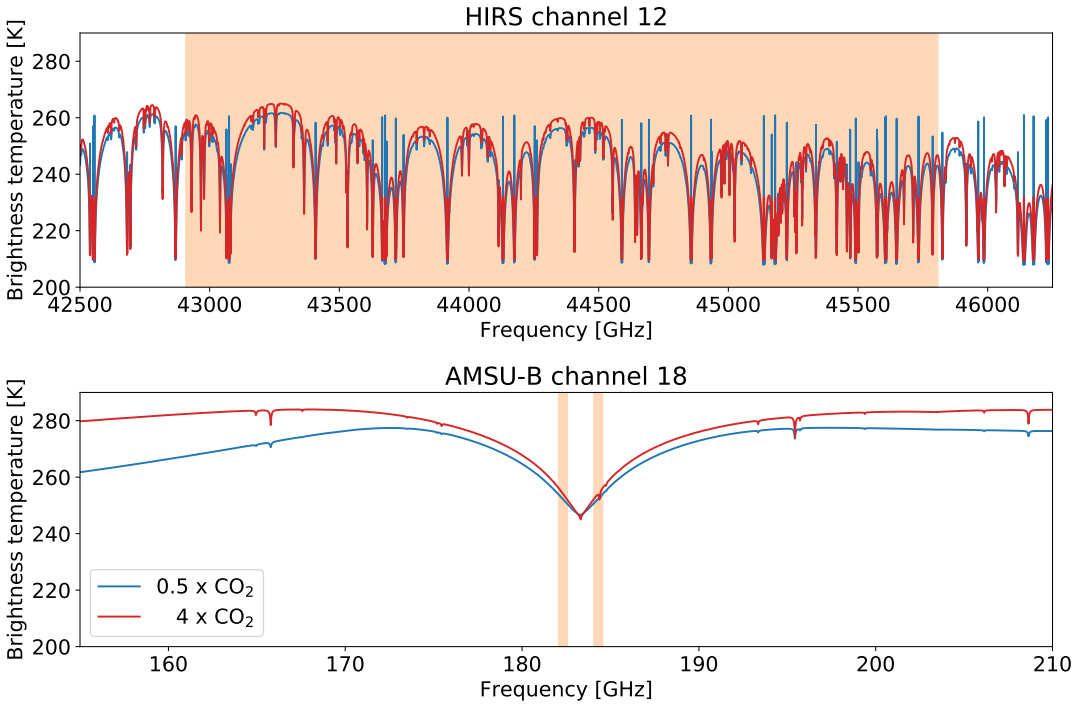

Figure 4.3: Spectrally resolved brightness temperatures in the HIRS 6.7 µm channel (upper panel) and the AMSU-B 183.31±1 GHz channel (lower panel) for the 0.5xCO_2 scenario (blue) and the 4xCO_2 scenario (red). The frequencies the channels are sensitive to are shaded in orange. The shift of the emission layer to lower pressures leads to a narrowing of the absorption lines in the 4xCO_2 scenario.

the absorption lines, however, there is almost no change in BT. As the MW channel is sensitive to frequencies close to the centre of the 183.31 GHz absorption line, the change in the MW BT is small compared to the change in the IR BT.

In summary, it can be said that the different absorption characteristics of the IR and the MW UTH channels lead to different changes in BT as the climate warms and the emission layer shifts to higher altitudes. However, from the results shown in Figure 4.3 it is not possible to determine whether IR or MW BT better reflects changes in RH. To evaluate this, the evolution of fitted UTH from HIRS and MW BTs has to be compared to the evolution of the true UTH. This comparison is performed in the next section, using more realistic atmospheric profiles from a global climate model simulation.

4.2 Investigation of UTH in idealised climate model simulations

The goal of this section is to investigate whether IR or MW BTs better reflect the evolution of upper-tropospheric RH as the climate warms. This is done using a global climate model simulation, in which the atmospheric temperature increases as a result of an increasing CO_2 concentration. In the model output, the evolution of the true UTH (UTH_{true}) is compared to the evolution of the UTH derived from HIRS and AMSU-B BTs, which are hereafter referred to as UTH_{HIRS} and $UTH_{\mathrm{AMSU-B}}$, respectively.

4.2.1 The CMIP5 1%CO_2 run with the MPI-ESM-LR model

The climate model simulation used here is part of the fifth phase of the Coupled Model Intercomparison Project (CMIP5). CMIP5 was launched in 2008 and comprises a set of coordinated climate model simulations performed to improve the understanding of the climate system (Taylor et al., 2012). More than 20 research groups from major international modelling centres were involved in the development of the simulations, which were performed with more than 50 different numerical models. The purpose of the simulations is to determine how good the models are in simulating the recent years and to perform climate projections on two different time scales: near term decadal predictions and long-term predictions on time scales of more than a century.

The 1%CO_2 run, which is used for this study, is part of the core long-term simulations of CMIP5 (Taylor et al., 2012). It is an idealised experiment designed to diagnose the transient climate response to increasing CO_2 concentrations (Giorgetta et al., 2013). The transient climate response is defined as the temperature change by the time the CO_2 concentration has doubled. The 1%CO_2 run is initialised with the so-called piControl experiment, which is a 1000 year pre-industrial control simulation with a forcing that is constant in time. The constant forcing includes well-mixed greenhouse gas concentrations that are kept fixed at their values from 1850. During the total model integration time of 150 years (1850 - 2000) all forcings are the same as in piControl except from the CO_2 concentration, which increases by 1 % every year. This results in a doubling of CO_2 after about 70 years and a quadrupling after about 140 years.

One of the models that participated in the CMIP5 simulations is the Max-Planck-Institute Earth System Model (MPI-ESM). For the investigations here, results from the low reso-

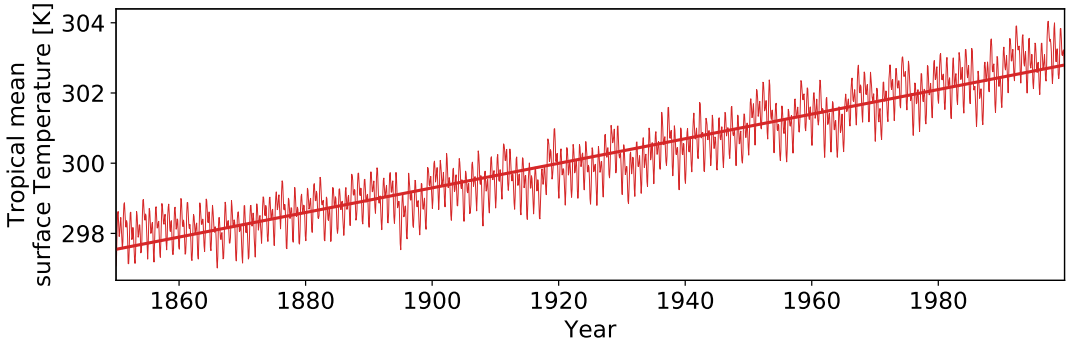

Figure 4.4: Monthly tropical mean surface temperature in the MPI-ESM-LR 1%CO_2 run over the total integration time from 1850 to 2000 (thin line). The slope of the linear trend (thick line) is 0.035 K per year.

lution (LR) version of the MPI-ESM are used. The model consists of coupled general circulation models for the atmosphere (ECHAM6, (Stevens et al., 2013)) and the ocean (MPIOM, (Jungclaus et al., 2013)) as well as the subsystem models for land and vegetation (JSBACH, (Reick et al., 2013)) and the marine biogeochemistry (HAMOCC5, (Ilyina et al., 2013)). The exchange of fluxes of water, energy, momentum and CO_2 between the subsystems is managed by the coupling program named OASIS (Giorgetta et al., 2013). In the LR configuration of MPI-ESM the atmospheric model ECHAM6 has a horizontal resolution of 1.9°, the atmosphere consists of 47 vertical levels and the ocean model has a horizontal resolution of about 1.5° and consists of 40 vertical levels. More details on the model configuration are given by Giorgetta et al. (2013). Figure 4.4 shows how the tropical mean surface temperature evolves in the MPI-ESM-LR model in the 1%CO_2 run. It increases approximately linearly by about 0.35 K per decade. The total change in surface temperature over the total model integration time is about 5 K.

The model output variables that are used in the analysis here are given as monthly averages on 25 pressure levels and on a latitude-longitude grid with 1.9° resolution. UTH_{true} is calculated for every grid point from vertical profiles of RH according to the new definition (Section 3.1). Subsequently, a tropical average of UTH_{true} is calculated for every month.

4.2.2 Radiative transfer simulations with RTTOV

To simulate the BTs a satellite instrument would measure above the model atmospheres, version 12.1 of the fast radiative transfer model for TOVS (RTTOV) (Saunders et al., 2018) is used. Here, the acronym TOVS stands for The TIROS Operational Vertical Sounder, an instrument package on board the NOAA polar-orbiting satellites called Television Infra-Red Observing Satellite (TIROS). RTTOV allows fast simulations of radiances for visible, IR and MW downward-looking scanning radiometers for given atmospheric profiles of temperature, gas concentrations and surface properties. In contrast to line-by-line models like ARTS, the fast radiative transfer model RTTOV uses a faster, but more approximate method called band transmission to simulate radiative transfer. Instead of considering the contribution of each spectral line to the absorption coefficients, the absorption in an entire frequency band is described by a set of pre-calculated coefficients, depending on the atmospheric conditions. RTTOV is used to simulate BTs for the output of the MPI-ESM-LR 1%CO_2 simulation, because simulations with a line-by-line model would be too time consuming.

An existing Python wrapper for RTTOV (Hocking et al., 2018) that has been adapted by Verena Grützun (University of Hamburg) is applied to simulate clear-sky BTs measured in the UTH channels of AMSU-B and HIRS for every month and every grid point of the model. UTH_{HIRS} and $UTH_{\mathrm{AMSU-B}}$ are then calculated using the BT transformation method and the scaling coefficients found in Section 3.3. Spatial averaging is performed to obtain tropical means of UTH_{HIRS} and $UTH_{\mathrm{AMSU-B}}$, which can be compared to those of UTH_{true}.

During the course of this work it turned out that the BTs simulated with RTTOV differ from those simulated with ARTS. As ARTS is well-validated (Melsheimer et al., 2005; Saunders et al., 2007) and line-by-line models are generally more accurate than fast radiative transfer models, it is assumed that the ARTS BTs are more reliable than the RTTOV BTs and the scaling coefficients determined from ARTS BTs (Section 3.3) are used further on. However, applying these scaling coefficients to RTTOV BTs has consequences for the fitted UTH. Figure 4.5 shows the logarithm of the true UTH of all tropical profiles from the first month (January 1850) of the MPI-ESM-LR 1%CO_2 simulation versus the AMSU-B nadir BT simulated with ARTS (blue) and RTTOV (orange). In the month shown, RTTOV BTs are generally lower than ARTS BTs, especially at the cold end of the BT distribution, where the difference is up to 4 K. The red dashed line

represents the transformation of BT to $UTH_{\mathrm{AMSU-B}}$ with the scaling coefficients from Section 3.3. As expected, the line fits better to the ARTS BTs and lies above the RTTOV BTs. Thus, scaling the RTTOV BTs with the coefficients from Section 3.3 leads to a moist bias in the tropical mean $UTH_{\mathrm{AMSU-B}}$ with respect to UTH_{true}. The same applies for UTH_{HIRS} (not shown). This should be kept in mind when analysing the fitted UTH in the next section.

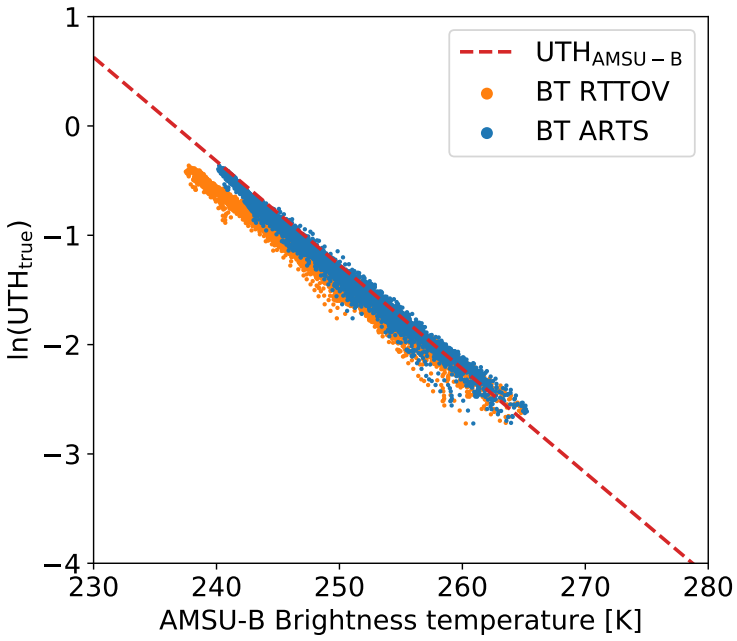

Figure 4.5: Logarithm of UTH_{true} versus AMSU-B nadir BT simulated with ARTS (blue) and RTTOV (orange), respectively, for all tropical profiles in the first month of the MPI-ESM-LR 1%CO_2 run. The logarithm of the fitted UTH obtained by scaling the BT with the scaling coefficients from Section 3.2 is indicated by the dashed red line. Scaling the RTTOV BTs with the same coefficients leads to a moist bias in UTH.

4.3 Trends of true and fitted UTH in the 1%CO_2 run

The evolution of the monthly, tropical mean simulated BTs for AMSU-B and HIRS over the total model integration time of 150 years is shown in Figure 4.6. Different trends are apparent in the AMSU-B and HIRS BTs. While the AMSU-B BT decreases by about 0.02 K per decade, the HIRS BT increases by about 0.09 K per decade. The fact that the

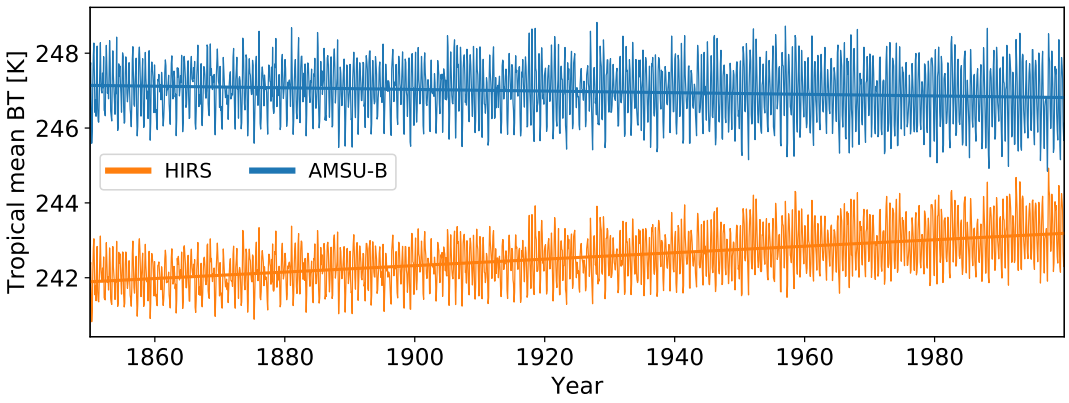

Figure 4.6: Timeseries of tropical and monthly mean BTs for AMSU-B (blue) and HIRS (orange) for the MPI-ESM-LR 1%CO_2 run. The BTs are simulated with RTTOV. The fitted linear trends (solid lines) are -0.02 K per decade for AMSU-B and 0.09 K per decade for HIRS.

HIRS BT increases more strongly than the AMSU-B BT in a warming climate is in line with the findings based on RCE profiles in Section 4.1.

Figure 4.7 shows the evolution of the monthly, tropical mean UTH_{true} as well as the evolution of tropical mean UTH_{HIRS} and $UTH_{\mathrm{AMSU-B}}$ over the model integration time. When comparing UTH_{true} to $UTH_{\mathrm{AMSU-B}}$ and UTH_{HIRS} an offset of about 10% RH is visible (Figure 4.7). This moist bias in the fitted UTH results from the difference between RTTOV and ARTS BTs, which was explained in the previous section. Since this bias only affects the absolute value but not the trend of tropical mean UTH, no attempt is made here to correct for it. In the following, only the trends are considered.

The fitted linear trend of the true UTH is slightly positive with a slope of 0.06% RH per decade. Thus, in the MPI-ESM-LR model the true RH in the UTH layer slightly increases over the model integration time. Figure 4.8 shows how the altitudes of the UTH layer boundaries change over time. It is apparent that both upper and lower boundary move upwards by about 2 km. Thus, as expected, the UTH layer moves to higher altitudes as the atmosphere warms.

When comparing $UTH_{\mathrm{AMSU-B}}$ and UTH_{HIRS} to UTH_{true} (Figure 4.7), it is apparent that $UTH_{\mathrm{AMSU-B}}$ captures the evolution of UTH_{true} quite well. With an increase of about 0.10% RH per decade it follows a similar trend as UTH_{true}. UTH_{HIRS}, however, evolves differently and decreases by about 0.44% RH per decade. This comparison with

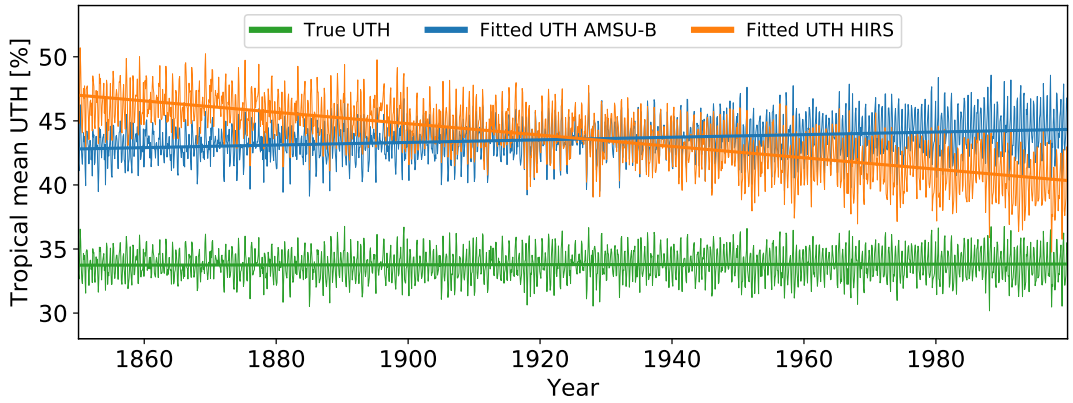

Figure 4.7: Timeseries of monthly area-weighted tropical mean of UTH_{true} (green) as well as $UTH_{\mathrm{AMSU-B}}$ (blue) and UTH_{HIRS} (orange) for the MPI-ESM-LR 1%CO_2 run. The fitted linear trends (thick lines) are 0.06% RH per decade for UTH_{true}, 0.10% RH per decade for $UTH_{\mathrm{AMSU-B}}$ and -0.44% RH per decade for UTH_{HIRS}, respectively.

UTH_{true} reveals that the HIRS BT does not correctly reflect the evolution of RH and it is influenced by additional factors. As demonstrated in Section 4.1, a key factor leading to an increase in the HIRS BT is the shift of the UTH layer to lower pressures.

The fact that the trend of $UTH_{\mathrm{AMSU-B}}$ is not equal to the trend of UTH_{true} suggests that the AMSU-B BT is also influenced by other factors than RH, which lead to a decrease in BT. Such additional factors have to be further investigated in future studies. However, the resulting artificial trend in $UTH_{\mathrm{AMSU-B}}$ is about one magnitude smaller than the artificial trend in UTH_{HIRS}. Thus, it can be concluded that the AMSU-B BT is more suitable to investigate trends in RH than the HIRS BT.

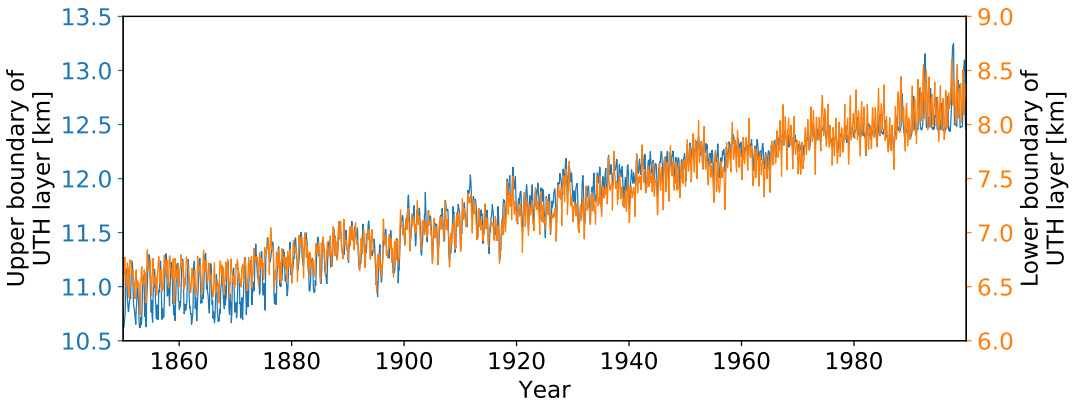

Figure 4.8: Time series of monthly tropical mean altitudes of upper boundary (blue, left y-axis) and lower boundary (orange, right y-axis) of the UTH layer in km. Both boundaries move upwards by about 2 km over the total model integration time.

4.4 A simple correction for IR UTH

The results above have shown that there is a strong negative trend in UTH_{HIRS} which is not caused by a change in RH. In the following, a simple correction for the time series of tropical mean UTH_{HIRS} is introduced, which removes the trend caused by other factors than RH.

The negative trend in UTH_{HIRS} (Figure 4.7) is most-likely caused by the upward shift of the emission layer as the climate changes. This upward shift results from an increase of atmospheric water vapour concentration, which is in turn controlled by the atmospheric temperature. Assuming that the surface temperature T_s (Figure 4.4) can be used as a proxy for the increase in atmospheric temperature, the linear trends found in the previous section can be used to remove the trend in tropical mean UTH_{HIRS} that is not caused by RH. Defining ΔT_s as the deviation of T_s from a reference surface temperature T_{ref}:

$$\Delta T_s = T_s - T_{ref}, \tag{4.1}$$

the corrected time series $UTH_{\mathrm{HIRS,corr}}$ is obtained by

$$UTH_{\mathrm{HIRS,corr}} = UTH_{\mathrm{HIRS}} - \frac{m_{UTH_{\mathrm{HIRS}}} - m_{UTH_{\mathrm{true}}}}{m_{T_s}} \Delta T_s = UTH_{\mathrm{HIRS}} + 1.28\frac{\%}{\mathrm{K}}\Delta T_s. \tag{4.2}$$

Here, $m_{UTH_{\mathrm{HIRS}}}$, $m_{UTH_{\mathrm{true}}}$ and m_{T_s} are the linear trends of the time series of UTH_{HIRS} (Figure 4.7), UTH_{true} (Figure 4.7) and T_s (Figure 4.4), respectively. According to Equation 4.2, an increase of 1 K in surface temperature leads to a decrease of 1.28% RH in UTH_{HIRS} that has to be corrected.

The corrected time series of UTH_{HIRS} is shown in Figure 4.9. Here, T_{ref} was set to 300.2 K to achieve that the UTH_{HIRS} time series is not corrected at the point where it intersects with the $UTH_{\mathrm{AMSU-B}}$ time series. It is apparent that the correction works as desired, since UTH_{HIRS} has now the same trend as UTH_{true}. However, a major problem of the introduced correction is the fact that it is based on results from a single idealised model simulation only. It should be part of future work to test the correction with several other model simulations.

A more satisfactory solution than applying such a simple correction would be to adapt the BT transformation method in such a way that pressure variations in the UTH layer are taken into account. As mentioned in Section 2.1.5, the original form of the BT transformation method included an additional parameter, the scaled reference pressure p_0:

$$\ln(UTH\, p_0) = a + b\, BT. \tag{4.3}$$

The parameter p_0 is the atmospheric pressure p at the level at which the atmospheric temperature T equals the BT measured in the UTH channel (BT_{UTHC}), divided by 300 hPa:

$$p_0 = \frac{p[T = BT_{UTHC}]}{300\mathrm{hPa}}. \tag{4.4}$$

Thus, p_0 changes as the emission layer shifts. For a given BT a p_0 smaller than one adjusts UTH to slightly higher values and vice versa (Equation 4.3). By re-introducing p_0 or a similar reference pressure one could include the effect of a changing pressure due to a shift of the emission layer into the BT transformation method. This could help to prevent the emergence of false trends in the fitted UTH. A disadvantage of introducing this parameter is the fact that it has to be determined from additional measurements. A method for calculating p_0 from HIRS channel 6 observations is presented by Jackson and

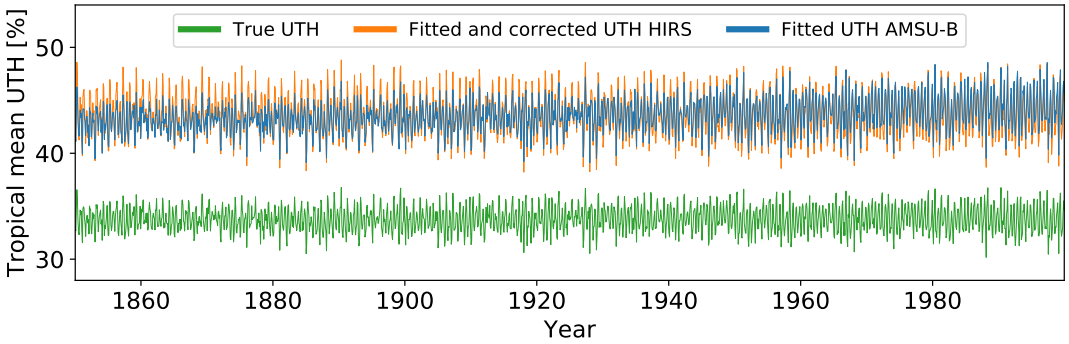

Figure 4.9: Similar as Figure 4.7 but with the corrected version of UTH_{HIRS} (see description in the text). Note that the time series of $UTH_{\mathrm{AMSU-B}}$ (blue) is almost not visible because it is covered by UTH_{HIRS} (orange).

Bates (2001). Introducing such a reference pressure in the BT transformation unfortunately exceeded the scope of this thesis, and therefore should be part of future work.

From the findings in this chapter it can be concluded that climatological trends in UTH from satellite observations with IR instruments should be treated with caution, because a change in UTH is not necessarily caused by a change in RH. To avoid wrong conclusions about the evolution of RH, it is recommended to look at the evolution of BT rather than UTH, at least as long as no satisfactory correction is developed. For this reason, the new CDR introduced in the next chapter will include both BT and UTH.

CHAPTER 5

A new UTH CDR

In this chapter, the newly developed UTH definition is applied to generate a climate data record (CDR) of UTH. It is based on an FCDR (Section 2.3) that has been created in the course of the Horizon 2020 project Fidelity and Uncertainty in Climate Data Records from Earth Observations (FIDUCEO) and contains calibrated BTs observed by microwave instruments.

It is planned to produce a second UTH CDR from the FIDUCEO HIRS FCDR, which can be used to complement the Microwave UTH CDR and expand it to earlier years. This combination of microwave and infrared UTH will be the first application of the newly introduced UTH definition. Unfortunately, the quality of the HIRS FCDR did not allow its use as CDR input at the time this thesis was written. Therefore, this chapter only describes the Microwave UTH CDR.

The core variables contained in the Microwave UTH CDR are monthly mean 183.31 ± 1 GHz BTs as well as the derived UTH, mapped on a regular latitude-longitude grid that covers the tropical region with a resolution of 1°x1°. In the following, the FCDR input data and the CDR processing chain including the propagation of uncertainties are explained. Furthermore, the format and the contents of the produced CDR are described and sources of uncertainty that have to be considered when working with the CDR data are discussed.

5.1 Input data: FIDUCEO Microwave FCDR

The FIDUCEO Microwave FCDR, which forms the basis for the UTH CDR, contains data from the microwave radiometers SSMT-2, AMSU-B and MHS (Section 2.2). The following

sections encompass the novelties of this FCDR, the satellite missions it covers and the variables it contains.

5.1.1 Novelties

As pointed out in Section 2.3, the quality of climate data records is often compromised by instrumental issues and inter-satellite biases. In addition to these general problems, existing data records have weaknesses that limit their use for climate research. Firstly, most of the existing data records do not provide any uncertainty information, although this information is crucial to express trust in the data and to draw reliable conclusions. Secondly, overlaps or doublings in the data files complicate the handling of the data or even lead to distorted results, if they remain undiscovered. Creating more reliable data records that are usable for climate research is one of the main objectives of the FIDUCEO project. The following improvements were achieved in the Microwave FCDRs that were created within this project (Hans, 2018):

- The calibration has been improved using a measurement function approach, providing consistent calibration for the MHS, AMSU-B and SSMT-2 instruments;
- metrologically traceable uncertainties are provided,
- new quality checks and flags are defined;
- each data file contains exactly one orbit of data, starting and ending at the equator.

The improved recalibration approach has significantly reduced the biases between individual instruments, so that no intercalibration in form of a bias correction is needed in contrast to earlier data sets. Further details about the calibration approach are given by Hans (2018).

5.1.2 Content

Like in all level 1 datasets, the variables in the FIDUCEO FCDRs are not yet binned to a latitude-longitude grid, but given at pixel level. This means that every variable has the dimensions x and y, corresponding to the directions across and along the satellite track in the satellite swath, respectively. The following variables contained in the FCDRs are of interest for the production of the UTH CDR (Hans et al., 2018):

- Geographical latitude and longitude

- Pixel acquisition time
- Brightness temperature for all instrument channels
- Uncertainties associated with brightness temperatures of all instrument channels at pixel level
- Seven bitmasks: one bitmask indicating the level of trust in the data, one bitmask indicating quality issues and five bitmasks indicating specific quality issues for each channel.

Figure 5.1 shows an example orbit of 183.31$\pm$1 GHz BT and the three classes of uncertainty for MHS on the Meteorological Operational Satellite B (Metop-B) as it is contained in the FIDUCEO Microwave FCDR. Details about the three classes of uncertainty are given in the next section.

5.1.3 Classification of uncertainties

The FIDUCEO FCDRs provide information on the uncertainty associated with the BT for each pixel. Here, the term uncertainty always denotes the standard uncertainty associated with a measurement.

The FCDR uncertainties are derived using a so-called measurement function approach (Hans, 2018). In general, a measurement function is the function that is used to obtain a measured output quantity value from input quantity values. In the case of an FCDR, it is the function used to convert the raw satellite data, which consists of digitized voltages, into the FCDR quantity, which is radiance or brightness temperature. For the Microwave FCDR, the central element of the measurement function is a so-called two-point-calibration (Hans et al., 2018). This means that the Earth radiance is governed by a linear interpolation between two reference signals. These reference signals come from a warm and a cold calibration target. The radiances emitted by these two targets are known from temperature measurements.

To obtain an uncertainty estimate for the output quantity, the uncertainties associated with the input quantities have to be quantified and propagated through the measurement function using the Law of the Propagation of Uncertainties (Section 2.4). To estimate the uncertainties of the input quantities, all influences or "effects" on the intstrumental calibration that lead to errors in the observed signal have to be taken into account.

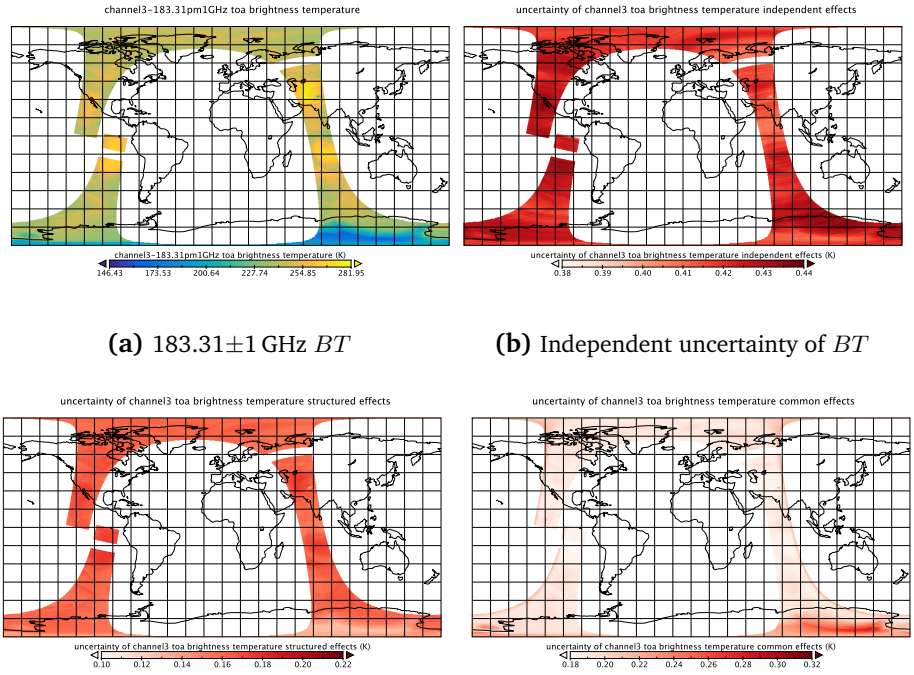

(a) 183.31±1 GHz BT **(b)** Independent uncertainty of BT

(c) Structured uncertainty of BT **(d)** Common uncertainty of BT

Figure 5.1: 183.31±1 GHz BT (a) and the three classes of uncertainty (b-d) in the FIDUCEO Microwave FCDR for an example orbit of MHS on Metop-B. Figure courtesy Imke Hans.

A detailed description of this approach and a complete list of effects included in the Microwave FCDR measurement-function is given by (Hans, 2018).

The uncertainties of the BTs given in the FCDR are split into three different classes, depending on the type of the underlying effect and the resulting error correlation:

- **Uncertainties due to independent effects** (hereafter independent uncertainties): The underlying effects are close to white noise and generate a completely independent uncertainty from pixel to pixel.
- **Uncertainties due to structured effects** (hereafter structured uncertainties): Even though the underlying effects are random, the calibration procedure can lead to error correlations between pixels that are located close to each other. The resulting correlations have spatial and temporal scales that are smaller than one satellite orbit.

- **Uncertainties due to common effects** (hereafter common uncertainties): Encompasses effects with correlation scales that are larger than one orbit (often the whole satellite mission).

This classification becomes important during the CDR processing, when several pixel-level values are averaged to get grid cell averages. Error correlations have to be taken into account when the uncertainty of the averaged value is determined (Section 2.4).

5.1.4 Satellite missions

In total, the Microwave FCDRs cover a time range of 24 years. Together with the HIRS FCDRs it will be possible to extent the data record to a total length of almost 40 years. Table 5.1 gives an overview of all satellite missions included in the Microwave FCDR. Note that in some cases the start and end times of the missions do not match the theoretical lifetimes of the instruments. The reason is that only data that is stored in the NOAA Comprehensive Large Array-data Stewardship (NOAA CLASS) archive was used for the FCDR production. In some cases these are only available for a restricted time range (Hans et al., 2018).

SSMT-2, the oldest of the three microwave instruments, was first launched in 1991 on the satellite F11, which was part of the Defense Meteorological Satellite Program (DMSP). It was followed by the satellites F12, F14 and F15, which were launched in 1994, 1997 and 1999, respectively. The first mission with the AMSU-B instrument started in 1998 with the satellite NOAA-15. Missions on NOAA-16 and NOAA-17 followed in 2000 and 2002, respectively. NOAA-18 and NOAA-19 are the first satellites carrying the newer MHS instrument. They were launched in 2008 and 2010 and are still operational. MHS is also carried by the Meteorological Operational (MetOp) Satellites controlled by the European Organisation for the Exploitation of Meteorological Satellites (EUMETSAT). MetOp-A has been in orbit since 2006, MetOp-B since 2013.

Table 5.1: Satellite missions and time periods covered by the Microwave FCDR. Table taken from Hans et al. (2019).

Instrument	Satellite	Start	End
SSMT-2	DMSP F11	1994-07-05	1995-04-02
SSMT-2	DMSP F12	1994-10-13	2001-01-08
SSMT-2	DMSP F14	1997-04-28	2005-01-10
SSMT-2	DMSP F15	2000-01-24	2005-01-02
AMSU-B	NOAA-15/K	1999-01-01	2011-03-28
AMSU-B	NOAA-16/L	2001-03-20	2014-04-30
AMSU-B	NOAA-17/M	2002-10-15	2013-04-10
MHS	NOAA-18/N	2005-08-30	2017-12-31
MHS	NOAA-19/N'	2009-11-01	2017-12-31
MHS	MetOp-A	2007-06-01	2017-12-31
MHS	MetOp-B	2013-01-29	2017-12-31

5.2 The processing chain

This section gives an overview of all steps involved in the processing of the UTH CDR. The processing chain is shown schematically in Figure 5.2. The production of the FIDUCEO L1C Microwave FCDR from the NOAA CLASS L1B data involves the removal of overlaps between adjacent files ("equator-to-equator-framing") as well as calibration and derivation of uncertainties. It is described in detail by Hans (2018) and is not further discussed here. The actual CDR processing starts with the finalized FCDRs. It involves a pre-screening of pixels, the transformation of BT to UTH and the aggregation and averaging of the pixels to get a monthly gridded field. Moreover, uncertainties of the FCDR BTs are propagated to the CDR quantities. Finally, the FIDUCEO CDR format is implemented to provide easily accessible NetCDF-4 files. The CDR generator that executes all the processing steps is implemented in Python 3.6.

The final CDR consists of three core variables: UTH, cloud-cleared BTs, which is the BT used to derive UTH, and unfiltered brightness temperatures (BT_{full}), which are not cloud-cleared. Consequently, the processing chain consists of three branches leading to these three variables (Figure 5.2). In the following, only the UTH branch is described in detail, because it combines all relevant processing steps. In the two BT branches some of these steps are omitted.

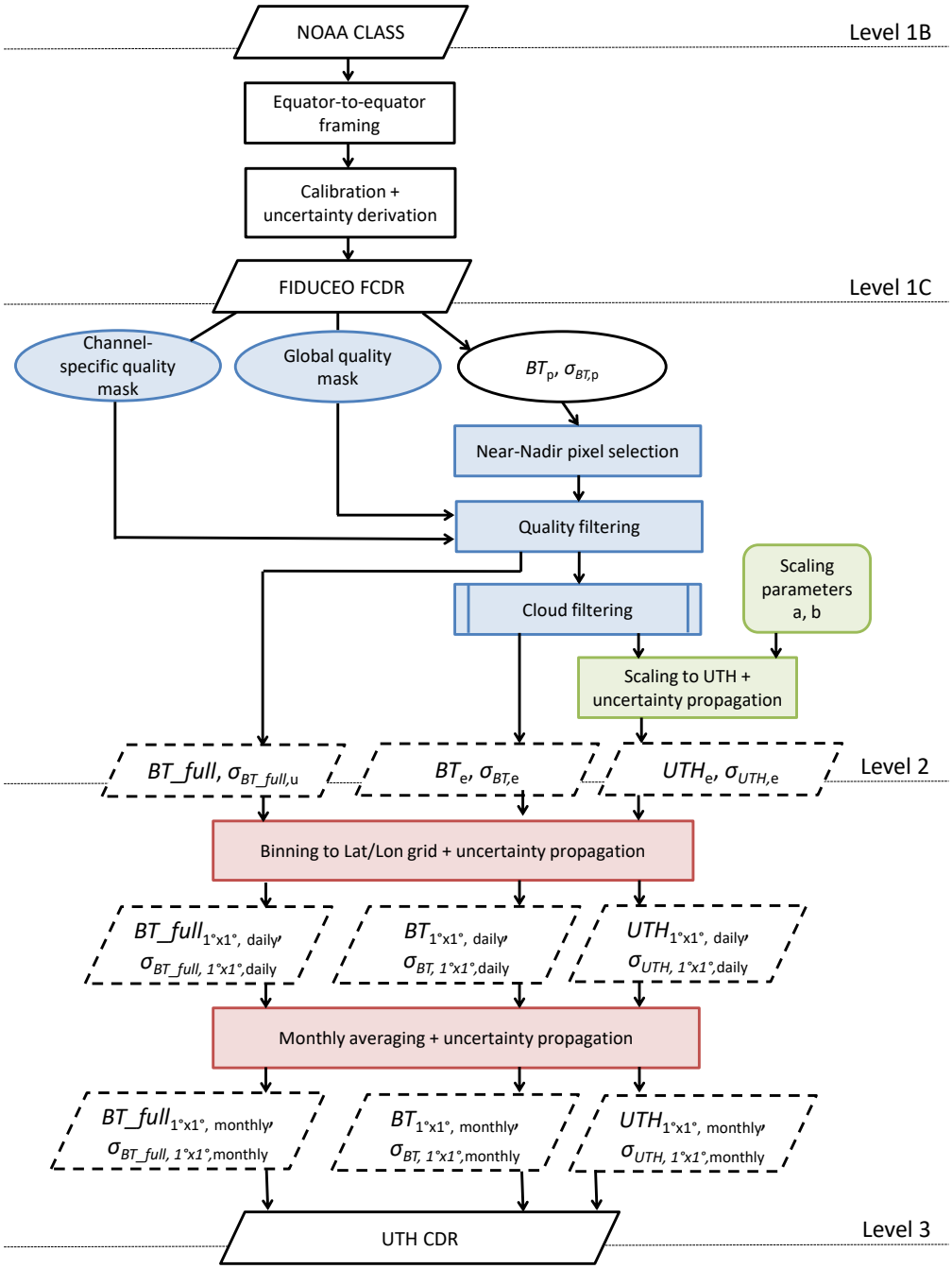

Figure 5.2: Schematic illustration of the UTH CDR processing chain, which is subdivided into pre-screening of pixels (blue), transformation of BT to UTH (green) and gridding and temporal averaging (red). Ellipses denote input data, rounded rectangles denote auxiliary input, rectangles denote processing steps, parallelograms with solid borders denote input or output data sets and parallelograms with dashed borders denote intermediate products that are not available to the user.

5.2.1 Pre-screening of pixels

The FCDR contains calibrated BT for every instrument channel at pixel level (Section 5.1.2). Only the 183.31±1 GHz BT is used as input for the UTH CDR. In the pre-screening procedure, a subset of pixels is selected from the pixel-level brightness temperatures BT_{p} for further processing (Figure 5.2). Only pixels located close to the nadir view of the satellite that meet certain quality criteria and are not contaminated by clouds are selected.

Nadir pixel selection

The UTH layer shifts to higher altitudes as the viewing direction of the satellite moves away from nadir. This shift in altitude is reflected in a decrease in the characteristic IWV thresholds towards off-nadir viewing angles, shown in Figure 3.2. However, it brings benefits to only include observations that provide information on a uniform altitude region into the CDR, e.g. when the UTH from the CDR is compared to UTH derived from model atmospheres or radiosonde profiles. Therefore, only pixels that are characterized by uniform IWV thresholds (Figure 3.2) are chosen for further processing, even though this comes at the expense of spatial and temporal coverage. For AMSU-B and MHS this holds true for the innermost 28 pixels of the scanline (14 on both sides of the nadir views). This corresponds to the innermost 10 pixels of SSMT-2, assuming that the IWV thresholds for SSMT-2 are similar to those of AMSU-B and MHS.

Quality screening

The FCDR contains information about the quality of each measurement in the form of an overall quality bitmask and a channel-specific bitmask. Pixels that are marked as "invalid" by the overall quality bitmask are rejected. This can have several different reasons, e.g. an invalid geolocation or viewing-geometry of the data, an invalid pixel acquisition time or an invalid sensor status. For a full list of reasons see the description of the quality bitmasks in Hans et al. (2018). Pixels are also discarded if the specific bitmask of the 183.31±1 GHz channel indicates that the calibration was not possible or there was bad data from the Earth views.

Cloud screening

UTH can only be derived from measurements of BT that are not contaminated by clouds. A strong advantage of MW measurements over IR measurements is the fact that clouds are nearly transparent in the MW. This particularly applies to the 183.31±1 GHz UTH channel, which receives signals originating from the upper troposphere and is hence not sensitive to low clouds. However, cold clouds with a high ice content do interact with MW radiation (Buehler et al., 2007) and can affect the measurement. The cloud particles scatter radiation away from the sensor's line of sight and hence cause a reduction in BT. In order to avoid that cloudy scenes are erroneously interpreted as very moist scenes, which would result in a positive UTH bias in the climatology, a cloud filtering has to be performed before retrieving UTH.

To filter out cloudy pixels, a method developed by Buehler et al. (2007) is used. It was developed based on AMSU-B measurements but works equally for MHS and SSMT-2 measurements due to the similar design of the instruments. The method is illustrated in Figure 5.3. It combines two criteria. The first one is the difference in BT the 183.31±1 GHz and the 183.31±3 GHz channels. Following the MHS channel naming they are hereafter called channel 3 (183.31±1 GHz) and channel 4 (183.31±4 GHz) and the measured brightness temperatures are called BT_{ch3} and BT_{ch4}, respectively. Under clear-sky conditions, BT_{ch3} is colder than BT_{ch4} because channel 3 is sensitive to a higher region in the troposphere than channel 4 and the temperature in the troposphere generally decreases with altitude. However, BT_{ch3} can be warmer than BT_{ch4} when ice clouds are present. Thus, pixels for which the difference $BT_{\mathrm{ch3}} - BT_{\mathrm{ch4}}$ is positive are classified as cloudy and discarded (Figure 5.3). The second criterion is a viewing angle dependent threshold on BT_{ch3}, which is roughly 240 K for near-nadir viewing angles. It has been shown by Buehler et al. (2007) that BT_{ch3} does not get smaller than this threshold for clear-sky atmospheres. Thus, pixels are identified as cloudy when BT_{ch3} is smaller than the threshold. The exact thresholds for every viewing angle are given in Buehler et al. (2007). For SSMT-2, which has a different scanning geometry than MHS and AMSU-B (Section 2.2), the thresholds corresponding to the nearest MHS viewing angles are used.

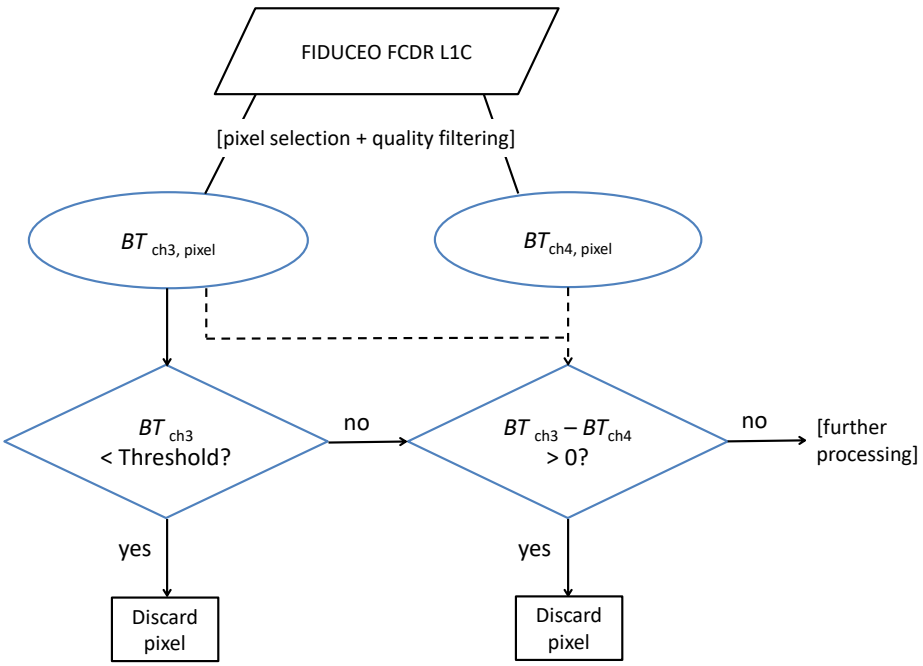

Figure 5.3: Illustration of the method used for the cloud filtering. Pixels are identified as cloudy and discarded when the BT in channel 3 (183.31±1 GHz) is smaller than a viewing angle dependent threshold or when the BT in channel 3 is larger than the BT in channel 4 (183.31±3 GHz).

5.2.2 Level 2 processing: Transformation of brightness temperature to UTH

The pixel-level BTs that are not discarded during the pre-screening are scaled to UTH using the BT transformation method:

$$UTH_{\mathrm{e}} = exp(a + b\,BT_{\mathrm{e}}), \tag{5.1}$$

where the index e denotes pixel-level quantities after pre-screening. For AMSU-B and MHS the scaling coefficients a and b that were determined in Section 3.3 are used. For SSMT-2 the coefficients are not derived separately, but the coefficients of the respective nearest MHS views are used. This is a reasonable simplification since the UTH channels of SSMT-2 and MHS have a very similar design. Since the scaling coefficients of MHS and

AMSU-B do not differ significantly (Section 3.3), it is assumed that the same is true for MHS and SSMT-2.

5.2.3 Level 3 processing: Pixel aggregation and averaging

As soon as UTH has been determined for each pixel, data from different pixels are combined in a two-step process. In the first step all pixels from observations of one day are aggregated in 1°x1° bins on a regular latitude-longitude grid that covers the tropical region from 30° South to 30° North. Subsequently, the aggregated pixels are averaged to get daily averages of UTH for each grid cell ($UTH_{1°\mathrm{x}1°,\mathrm{daily}}$):

$$UTH_{1°\mathrm{x}1°,\mathrm{daily}} = \frac{1}{N}\sum_{e=1}^{N} UTH_e. \tag{5.2}$$

Here, N is the number of pixels that are aggregated within the 1°x1° region. In a second step, daily averages are combined to monthly means for every grid cell:

$$UTH_{1°\mathrm{x}1°,\mathrm{monthly}} = \frac{1}{N_t}\sum_{t=1}^{N_t} UTH_{1°\mathrm{x}1°,\mathrm{t}}, \tag{5.3}$$

where the index t denotes the day of the month and N_t is the number of daily averages entering the monthly average. Note that in this averaging, every daily average is weighted equally, regardless of the number of pixels that contributed to the daily average. This way of averaging is chosen in order to capture the daily variations in UTH as well as possible. Another possibility would be to weight each daily average with the number of contributing pixels in the averaging, or even discard daily averages when the number of contributing pixels is below a certain threshold. This would give more weight to daily averages, for which the effect of instrumental noise is small, because they are based on more measurements. However, the natural variability of UTH is expected to be larger than the instrumental noise and it is hence more important to capture daily variations than to reduce the effect of noise. The goal is to obtain a monthly average, which is as close as possible to the "true" monthly average that would be obtained from a continuous observation.

In addition to the monthly mean UTH, the sample standard deviation of the daily UTH values is calculated and included in the CDR:

$$\sigma_{UTH} = \sqrt{\frac{\sum_{t=1}^{N_t}(UTH_{1°\text{x}1°,\text{t}} - UTH_{1°\text{x}1°,\text{monthly}})^2}{N_t - 1}}. \tag{5.4}$$

The above explained averaging procedure is carried out similarly for the cloud-filtered brightness temperatures $BT_{1°\text{x}1°,\text{monthly}}$ and the unfiltered brightness temperatures $BT_{\text{full},1°\text{x}1°,\text{monthly}}$ (Figure 5.2).

5.2.4 Propagation of uncertainties

For the propagation of uncertainties from FCDR to CDR level, the Law of the Propagation of Uncertainties (2.9) is used. The input quantities are the pixel-level BT from the FCDR. Their uncertainties have to be propagated to the gridded and averaged UTH values in the CDR. This is done in two steps: Firstly, uncertainties are propagated from level 1C to level 2, i.e. from pixel-level BT to pixel-level UTH. Secondly, they are propagated from level 2 to level 3, i.e. from pixel-level UTH to gridded and averaged UTH. Note that the first step is omitted in the processing of $BT_{1°\text{x}1°,\text{monthly}}$ and $BT_{\text{full},1°\text{x}1°,\text{monthly}}$.

Level 1C to level 2

The level 2 processing is a simple unit transformation with one input quantity BT_e and one output quantity UTH_e (Equation 5.1). Thus, Equation 2.9 simplifies to

$$\begin{aligned} u_c(UTH_e) &= \sqrt{(\frac{\partial UTH_e}{\partial BT_e})^2\, u_c(BT_e)^2} \\ &= |b\, exp(a + bBT_e)\, u_c(BT_e)| = |b\, UTH_e\, u_c(BT_e)|, \end{aligned} \tag{5.5}$$

where the index c denotes the three different classes of uncertainties: independent, structured and common uncertainties (Section 5.1.3). Each class is propagated separately to level 2.

Level 2 to Level 3

During the level 3 processing uncertainties are propagated from pixel-level UTH to daily grid cell averages $UTH_{1^\circ\text{x}1^\circ,\text{daily}}$ (Equation 5.2). For this averaging process, the Law of the Propagation of Uncertainties becomes

$$u_c(UTH_{1^\circ\text{x}1^\circ,\text{daily}}) = \frac{1}{N}\sqrt{\sum_{e=1}^{N} u_c(UTH_e)^2 + 2\sum_{e=1}^{N-1}\sum_{e'=e+1}^{N} u_c(UTH_e)u_c(UTH_{e'})r(e,e')}, \tag{5.6}$$

where $r(e, e')$ is the correlations coefficient of two pixels denoted by e and e'. From the second term in the square root it is clear that positive correlations at pixel level increase the uncertainties of the grid cell averages. For independent uncertainties the correlation term is zero. Consequently, the averaging process significantly reduces the uncertainty of the grid cell value compared to the uncertainties of the individual pixel values. If all N pixel uncertainties were equal, the grid cell uncertainty would be reduced by a factor $1/\sqrt{N}$. The opposite is true for the common uncertainties. For this class correlations extend over infinite length and time scales and the correlation coefficient r is one per definition. Thus, averaging of several pixel values does not reduce the grid cell uncertainty. In other words, the grid cell uncertainty is obtained by averaging the pixel uncertainties. For structured uncertainties, pixels are positively correlated over a certain number of adjacent scanlines in the satellite swath. This results from an averaging of calibration coefficients over several scanlines (Hans, 2018). In the case of the Microwave FCDR, calibration coefficients are always averaged over seven scanlines. Thus, the overall length scale over which the correlation decreases to zero is seven scan lines. The FCDR contains so-called correlation vectors ρ, which provide the correlation coefficient of two pixels e and e' as a function of the difference between the scanlines l of these pixels $|l_e - l_{e'}|$. With these correlation vectors the second term in the square root of Equation 5.6 can be written as

$$2\sum_{e=1}^{N-1}\sum_{e'=e+1}^{N} u_c(UTH_e)u_c(UTH_{e'})\rho(|l_e - l_{e'}|). \tag{5.7}$$

The uncertainty propagation from daily averages $UTH_{1^\circ\text{x}1^\circ,\text{daily}}$ to the monthly average $UTH_{1^\circ\text{x}1^\circ,\text{monthly}}$ (Equation 5.3) is performed in a very similar way, under the assumption

that there is no temporal correlation for independent and structured uncertainties and full temporal correlation, i.e. $r = 1$, for common uncertainties.

So far it has not been considered that error correlations between the pixel-level input quantities also lead to correlations between the final grid cell averages. These "inter-grid cell correlations" must be taken into account by the CDR user when further spatial or temporal averaging is performed. For independent and common uncertainties the correlations behave in the same way as on pixel level. Thus, independent uncertainties are not correlated at all, common uncertainties are fully correlated over infinite length and time scales.

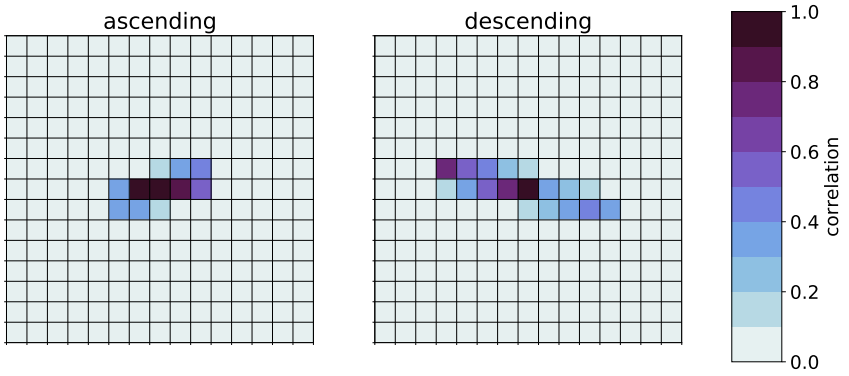

Figure 5.4: Correlations of structured uncertainties on grid cell level from one month (January 2016) of data from MHS on Metop-A for the example of a 15x15 grid with 1° resolution located at the equator. Correlations between the centre grid cell and the remaining grid cells are shown for ascending (left) and descending (right) satellite overpasses.

For structured uncertainties, the correlation structure is more complex. Therefore, a complete propagation that also yields the covariances of the grid cell averages has to be performed using the matrix form of Equation 5.6. However, this requires large covariance matrices and hence much computational power. Therefore, this propagation is not performed in the CDR processing. However, to get an idea of the correlation pattern at grid cell level, the full uncertainty propagation is carried out for one example case, namely one month of BTs from MHS on Metop-A on a 15x15 grid with 1° resolution that is located around the equator. Figure 5.4 shows the resulting correlations between

the grid cell in the centre and adjacent grid cells. Correlations occur over a maximum range of ± 4 grid cells in zonal direction and ± 2 grid cells in meridional direction. The correlation pattern differs between ascending and descending satellite overpasses because the satellite ground path is tilted in different directions with respect to the meridians. Inter-grid cell correlations are strongest in cross-track direction because for the structured effects pixels in the same scanline are fully correlated, whereas the correlation is weaker between pixels in neighbouring scanlines. In principle, it is possible to assume a general correlation pattern for structured uncertainties of each grid cell based on the given example. This pattern could be used when further averaging and uncertainty propagation is performed by the user. However, dealing with such correlation patterns is quite complex and requires huge correlation matrices for the uncertainty propagation. The effort associated with such an approach is somewhat disproportionate, given the fact that the structured uncertainties only represent a relatively small proportion of the total uncertainty (Hans, 2018). Therefore, it is recommended to treat the structured uncertainties the same as common uncertainties in an averaging process. This approach provides an upper limit for the structured uncertainty of the average.

5.3 A description of the FIDUCEO UTH CDR

5.3.1 Covered satellite missions

The CDR generator is run over all available Microwave FCDR data (Table 5.1) of SSMT-2, AMSU-B and MHS instruments. The final CDR does not cover exactly the same time periods as the FCDR, since only measurements from the 183.31 ± 1 GHz channel are used to derive UTH. Data gaps in this channel in the FCDR lead to data gaps in the CDR. All satellite missions and time periods covered by the UTH CDR are listed in Table 5.2 and illustrated as a bar chart in Figure 5.5.

5.3.2 File format

The CDR data files are written in NetCDF-4 format using a NetCDF-writer provided by Tom Block (Brockmann Consult), which implements the common CDR file format that has been defined within the FIDUCEO project. Each monthly average corresponds to one data file. Each file has a size of about 3.9 MB, resulting in a total CDR size of about 4.0 GB. The filenames follow the FIDUCEO standard and have the following structure:

FIDUCEO_CDR_UTH_{INSTRUMENT}_{SATELLITE}_{STARTTIME}_{ENDTIME}_L3_v{CDR-VERSION}_fv{WRITER-VERSION}.nc

where {INSTRUMENT} can be either SSMT2, AMSUB or MHS. {SATELLITE} can be any of the satellites these instruments are flying on. {STARTTIME} is the first second of the

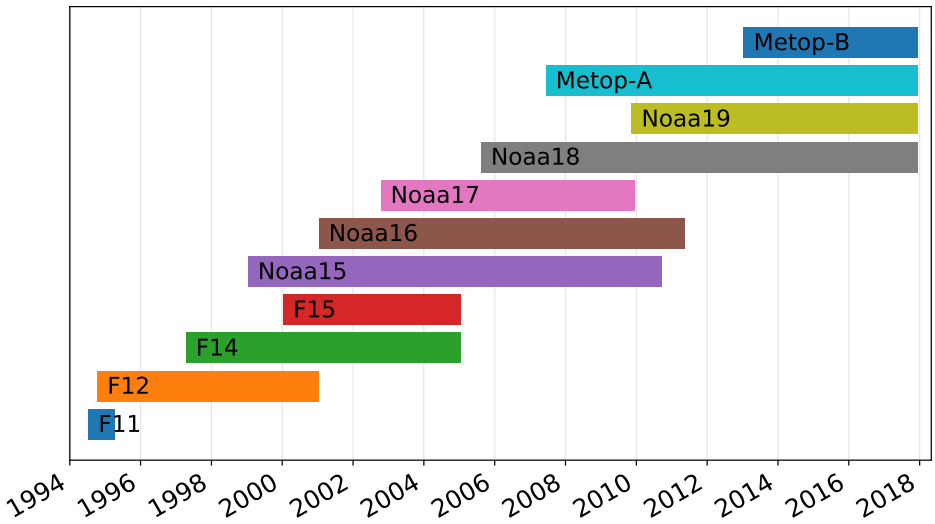

Figure 5.5: Time periods covered by the satellite missions contained in the UTH CDR.

Table 5.2: Satellite missions and time periods covered by the UTH CDR.

Instrument	Satellite	Start	End
SSMT-2	DMSP F11	07/1994	04/1995
SSMT-2	DMSP F12	10/1994	01/2001
SSMT-2	DMSP F14	04/1997	01/2005
SSMT-2	DMSP F15	01/2000	01/2005
AMSU-B	NOAA15	01/1999	09/2010
AMSU-B	NOAA16	01/2001	05/2011
AMSU-B	NOAA17	10/2002	12/2009
MHS	NOAA18	08/2005	12/2017
MHS	NOAA19	11/2009	12/2017
MHS	MetopA	06/2007	12/2017
MHS	MetopB	01/2013	12/2017

first day in the month, with the format YEAR-MONTH-DAY-HOUR-MINUTE-SECOND, {ENDTIME} is the last second of the last day in the month. {CDR-VERSION} is the version number of the CDR and {WRITER-VERSION} is the version of the NetCDF-writer.

To make the CDR as self-explanatory as possible, the files provide global attributes with general information and a set of data variables with individual attributes. The global attributes provide information on the version of the CDR and the time coverage of the data file. Moreover, they contain the Digital Object Identifier (DOI) of the data set, which was published by the Centre for Environmental Data Analysis (CEDA). In order to sustain traceability, a list of file names of all FCDR files that were used to generate the CDR file is also included in the global attributes. An example of the global attributes of a CDR file is given in Figure 5.6.

```
// global attributes:
   :_NCProperties = "version=1|netcdflibversion=4.6.1|hdf5libversion=1.10.1";
   :Conventions = "CF-1.6";
   :licence = "This dataset is released for use under CC-BY licence
(https://creativecommons.org/licenses/by/4.0/) and was developed in the EC FIDUCEO project \"Fidelity
and Uncertainty in Climate Data Records from Earth Observations\". Grant Agreement: 638822.";
   :writer_version = "2.0.0";
   :institution = "University of Hamburg";
   :title = "Upper Tropospheric Humidity (UTH)";
   :source = "FIDUCEO_FCDR_L1C_MHS_METOPA_20150101053447_20150101071607_EASY_v4.1_fv2.0.1.nc",
                [...]
             "FIDUCEO_FCDR_L1C_MHS_METOPA_20150131170323_20150131184443_EASY_v4.1_fv2.0.1.nc";
   :history = "Created on 2019-01-29 17:44.";
   :references = "";
   :comment = "Version 1.1 of UTH CDR based on Microwave FCDR Version 4.1.";
   :auxiliary_data = "";
   :configuration = "";
   :time_coverage_start = "20150101013042";
   :time_coverage_end = "20150201004846";
   :time_coverage_duration = "P30DT23H18M4S";
   :time_coverage_resolution = "P30DT10H29M6S";
   :geospatial_lat_units = "deg";
   :geospatial_lon_units = "deg";
   :geospatial_lat_resolution = 1.0; // double
   :geospatial_lon_resolution = 1.0; // double
   :id = "10.5285/ 2083b33b5c3d4cf0acb9a49226789caa";
   :naming_authority = "Centre for Environmental Data Analysis (CEDA)";
 }
```

Figure 5.6: Example for the global attributes of a UTH CDR file for January 2015 from data of MHS on Metop-A.

5.3.3 Variables

The monthly averages contained in the CDR are split into two parts: One from ascending satellite overpasses and one from descending overpasses. Each CDR file contains:

- Longitudes and Latitudes of grid cell centres and grid cell boundaries;

- Monthly average and standard deviation of all available channel 3 brightness temperatures (including cloudy pixels), for ascending and descending branches;
- Monthly average and standard deviation of all channel 3 brightness temperatures used to derive UTH (excluding cloudy pixels), for ascending and descending branches;
- Monthly average and standard deviation of UTH;
- Independent, structured and common uncertainty for monthly averages of brightness temperatures and UTH, for ascending and descending branches;
- Observation counts (number of pixels entering the grid cell average) and overpass counts (number of satellite overpasses contributing to the grid cell average) for ascending and descending branches;
- Earliest and latest time of day of pixel contribution to the monthly average, for ascending and descending branches;

The data has the following dimensions:

- x - East-west dimension (size: 360);
- y - North-south dimension (size: 61);
- bounds - Dimension defining lower and upper bounds (size: 2);

A full list of variable names as well as their dimensions and descriptions is given in Table 7.2 in the Appendix. The names of the variables follow standard names from the Climate and Forecast (CF) metadata conventions for those cases where a standard name exists. Where no standard name exists, the FIDUCEO team has introduced a name not included in the standard. The suffixes "`_ascending`" and "`_descending`" indicate whether a variable is derived from ascending or descending satellite overpasses, respectively. For each variable several attributes are provided. They contain information on the unit and the dimensions of the variable, as well as a description of the quantity. Before storing, the data are scaled to integers to reduce the required disk space. The corresponding scale factors are also part of the attributes. They are applied automatically when established NetCDF-readers, as e.g. implemented in Python or MATLAB, are used to read the data. Another attribute is the fill value, which is placed whenever there are data gaps due to missing FCDR data or due to cloud coverage.

5.3.4 Example content

Monthly fields of brightness temperature and UTH

The core quantities of the CDR are the monthly averages of 183.31±1 GHz BT and UTH, together with their uncertainties. They are shown in Figure 5.7 and Figure 5.8 for the example of July 2012, using data from the ascending overpasses of MHS on NOAA18. The corresponding observation counts and satellite overpass counts are shown in Figure 5.9.

In the monthly mean cloud-cleared BT (Figure 5.7) and the retrieved UTH (Figure 5.8) one can clearly distinguish the dry subsidence regions, which are associated with high BTs from the moister, convective regions, which are associated with low BTs. The standard deviation of daily UTH averages is smaller in the dry subsidence regions than in the moist regions, because the UTH in the subsidence regions always has small values.

Figure 5.7 also shows the three uncertainty classes for BT. When comparing the overall structure of independent and structured uncertainties to the satellite overpass counts shown in Figure 5.9, it becomes clear that a small number of satellite overpasses results in high independent and structured uncertainties. The reason is that these types of uncertainties are reduced by a factor of approximately $1/\sqrt{N}$ in an averaging process with N samples. The more satellite overpasses, the smaller the independent and structured uncertainties. Common uncertainties, by contrast, are not reduced by averaging and hence show a different pattern. Their magnitude seems to be large where the BT is low and vice versa. This is because the common uncertainty in the 183.31±1 GHz channel is dominated by the uncertainty due to the polarisation correction, which depends on the Earth radiance (Hans et al., 2019).

The magnitudes of the individual uncertainty classes are different in every satellite mission (Hans, 2018), because the effects that contribute to the uncertainties differ among the missions. This is apparent from Figure 5.10, which shows histograms of independent, structured and common uncertainties on grid cell level for two complete example missions. The Metop-A and NOAA15 missions were chosen here, because they represent the missions with the smallest and largest overall measurement uncertainties in the CDR. Therefore, they provide an overview of the possible range of magnitudes of the CDR uncertainties. The average magnitudes of independent, structured and common uncertainties of BT in the Metop-A mission are approximately 0.04 K, 0.06 K and 0.19 K,

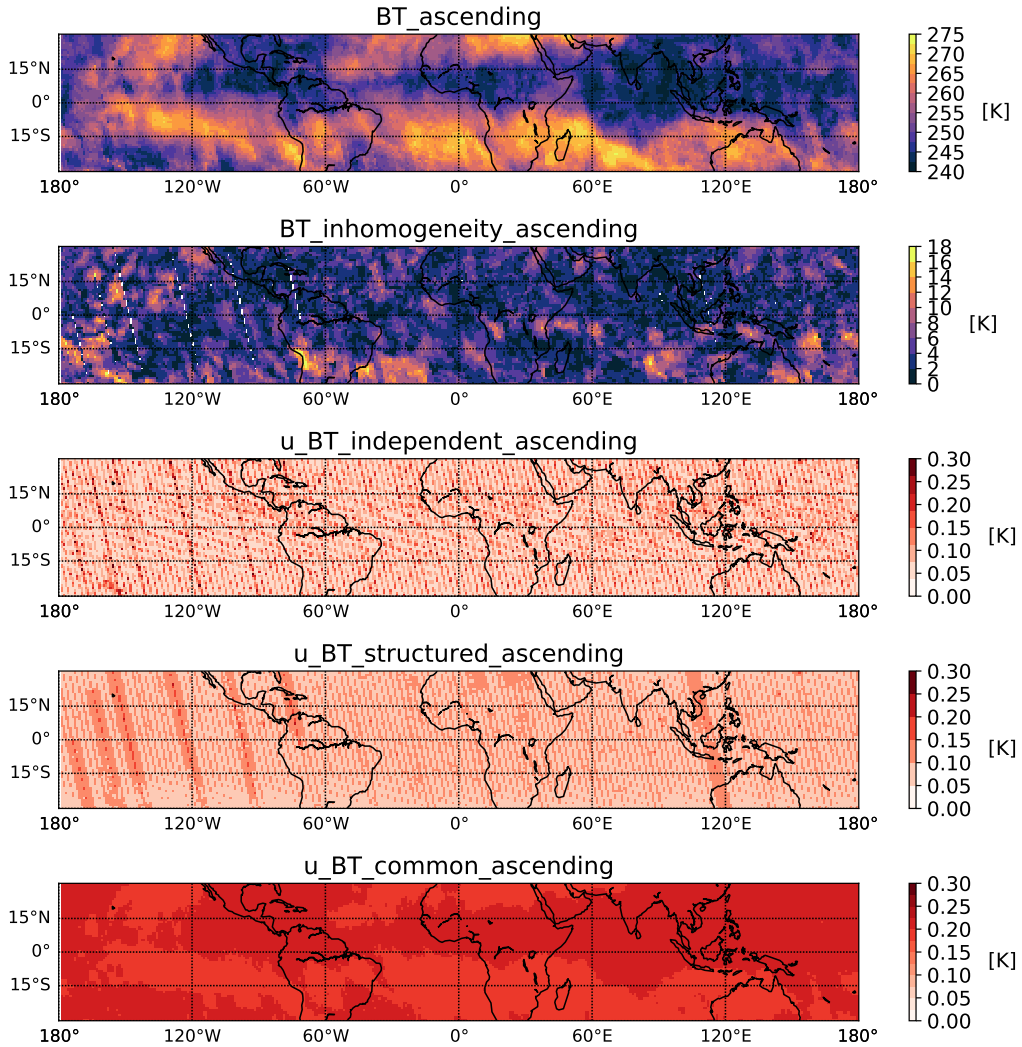

Figure 5.7: Example CDR content: Monthly mean brightness temperature (first panel) for July 2012 from ascending passes of MHS on NOAA18 as well as standard deviation of daily brightness temperature averages (second panel) and uncertainties of brightness temperature split into three classes: independent, structured and common uncertainties (third to fifth panel)

respectively. In the NOAA15 mission the average magnitudes are approximately 0.11 K, 0.19 K and 0.60 K for independent, structured and common uncertainties, respectively. However, in both missions the independent uncertainty represents the smallest class, followed by the structured and the common uncertainty. Except from the NOAA19 mission, in which the structured uncertainty dominates (not shown), this order is found

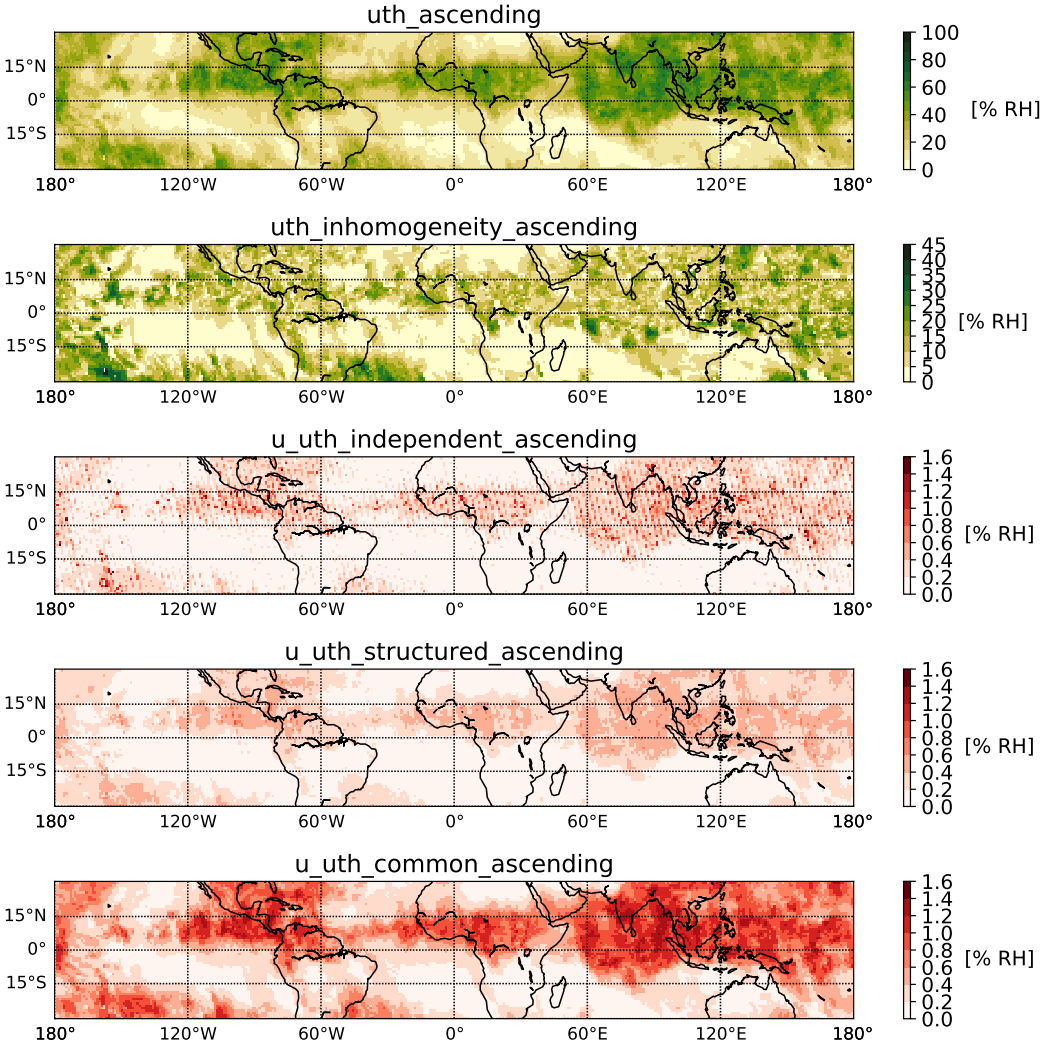

Figure 5.8: Example CDR content: Monthly mean UTH (first panel) for July 2012 from ascending passes of MHS on NOAA18 as well as standard deviation of daily brightness temperature averages (second panel) and uncertainties of UTH split into three classes: independent, structured and common uncertainties (third to fifth panel)

in all satellite missions in the CDR. This distinguishes the CDR uncertainties from the FCDR uncertainties and is owed to the fact that common uncertainties are not reduced in the averaging processes in the CDR processing, whereas independent uncertainties are significantly reduced. Structured uncertainties are also reduced to a certain degree, but less than independent uncertainties.

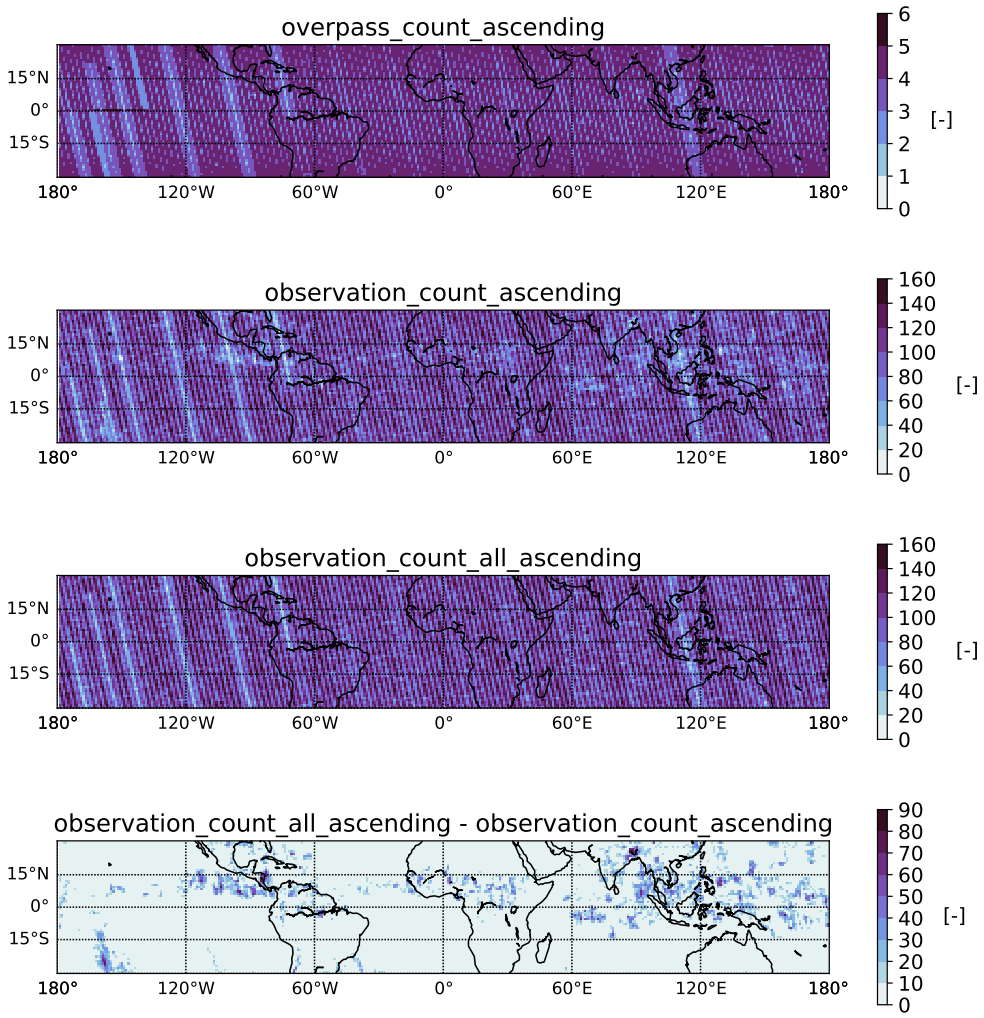

Figure 5.9: Different kinds of count variables in the CDR: count of satellite overpasses (`overpass_count`, first panel), count of pixels – excluding cloudy pixels – contributing to the monthly averages (`observation_count`, second panel) and counts of pixels including cloudy pixels (`observation_count_all`, third panel). The difference between `observation_count_all` and `observation_count` yields the number of cloudy pixels that have been discarded during the UTH retrieval (fourth panel).

In the uncertainties of UTH (Figure 5.8) the same structures as in the uncertainties of BT (Figure 5.7) are generally visible. However, there is another pattern superimposed, which resembles the UTH itself. From the transformation of BT to UTH in Equation 5.1, it is clear that a given absolute change in BT leads to a certain relative change in

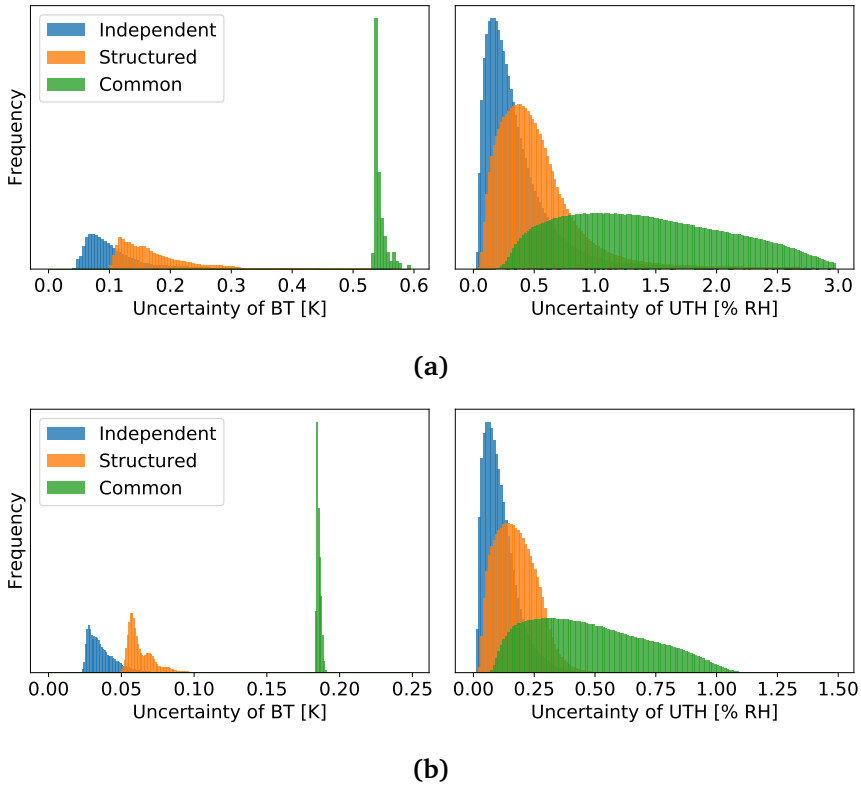

Figure 5.10: Histograms of grid cell level uncertainties of BT (left panels) and UTH (right panels) for the complete NOAA15 mission (a) and Metop-A mission (b), which represent the two missions with the smallest and largest overall measurement uncertainty in the CDR.

UTH. For example, an absolute change of $+1\,\mathrm{K}$ in BT results in a relative change of $e^{1\mathrm{K}\,b}$ ($\approx$0.9) in UTH. Hence, the absolute change in UTH is large when UTH is large and vice versa. Consequently, when uncertainties are propagated from BT to UTH, they have to be weighted with UTH (Equation 5.5). This explains why the magnitude of the uncertainties of UTH is primarily determined by the magnitude of UTH itself (Figure 5.8). This is also evident from the histograms of the three classes of uncertainty of UTH shown in the right panels of Figure 5.10. Due to the weighting with UTH, the distributions of the UTH uncertainties are broader than the distributions of the BT uncertainties.

The count variables in the CDR (Figure 5.9) can be used to identify different kinds of data gaps. As the name suggests, the variable `overpass_count` counts the number of satellite overpasses in each grid cell. The variable is most suitable for identifying large data gaps, for example the lack of a whole orbit of data. The observation counts

count the number of pixels contributing to the monthly average. Two different kinds of observations counts are given: `observation_count` only includes pixels contributing to the monthly means $UTH_{1°\text{x}1°,\text{monthly}}$ and $BT_{1°\text{x}1°,\text{monthly}}$, i.e. cloudy pixels are not counted. `observation_count_all` counts all pixels, including cloudy pixels and corresponds to the number of pixels entering $BT_{full,1°\text{x}1°,\text{monthly}}$. The difference between `observation_count_all` and `observation_count` yields the number of cloudy pixels that have been discarded during the UTH retrieval.

In the overpass and observation counts striped and chessboard-like patterns are visible. Hence, the grid cells are observed with varying frequencies as a result of the way the satellite samples the Earth. It can be argued that the resolution of the latitude-longitude grid should be made coarser, to smooth out some of these patterns and ensure a uniform sampling. The user is indeed advised to combine several grid cells and thereby smooth the data when looking at monthly fields. However, temporal averaging reduces these sampling effects. Thus, when quantities like yearly or seasonal averages are calculated, the fine grid resolution of 1°x1° can be maintained.

Application example: A time series of tropical mean UTH

An obvious application of the UTH CDR is the creation of a time series of monthly, tropical mean UTH with an estimate of the measurement uncertainty. This section provides a short instruction on how to calculate tropical means and how to combine uncertainties to obtain a time series for a whole satellite mission as those shown in Figure 5.11.

As a first step, the monthly averages from ascending and descending satellite overpasses, UTH_{asc} and UTH_{desc}, have to be averaged to one combined field $UTH_{\text{asc+desc}}$. The corresponding independent uncertainties $u_{\text{ind,asc}}$ and $u_{\text{ind,desc}}$ are added as follows:

$$u_{\text{ind}} = \frac{\sqrt{u_{\text{ind,asc}}^2 + u_{\text{ind,desc}}^2}}{2}. \tag{5.8}$$

Common uncertainties $u_{\text{com,asc}}$ and $u_{\text{com,desc}}$ are treated as fully correlated:

$$u_{\text{com}} = \frac{u_{\text{com,asc}} + u_{\text{com,desc}}}{2}. \tag{5.9}$$

As explained in Section 5.2.4, it is recommended to treat the structured uncertainties the same as common uncertainties. This approach is very conservative and provides an upper limit of the structured uncertainties of the mean. However, since structured uncertainties are small compared to the other two classes, the impact on the total uncertainty is small anyway.

Following the averaging of UTH_{asc} and UTH_{desc}, a tropical average UTH_{trop} can be calculated for every month of the satellite mission. Here one has to take into account that areas of the grid cells of the latitude-longitude grid are not uniform, but decrease from the equator towards higher latitudes. Thus, a weighted average should be performed using the cosine of the latitude of the grid cell centre ($\cos(lat_j)$) as weights:

$$UTH_{\mathrm{trop}} = \frac{\sum_{j=1}^{N_{\mathrm{cells}}} \cos(lat_j)\, UTH_{\mathrm{asc+desc},j}}{\sum_{j=1}^{N_{\mathrm{cells}}} \cos(lat_j)}, \tag{5.10}$$

where the index j denotes the grid cell index and N_{cells} is the total number of grid cells. The weighting factors $\cos(lat_j)$ have to be taken into account when uncertainties are propagated to UTH_{trop}. Again, the independent uncertainty of the tropical mean $u_{\mathrm{ind,trop}}$ is the square root of the summed squares of the individual grid cell uncertainties $u_{\mathrm{ind},j}$, weighted with $\cos(lat_j)$:

$$u_{\mathrm{ind,trop}} = \frac{\sqrt{\sum_{j=1}^{N_{\mathrm{cells}}} \cos(lat_j)^2\, u_{\mathrm{ind},j}^2}}{\sum_{j=1}^{N_{\mathrm{cells}}} \cos(lat_j)}, \tag{5.11}$$

The common uncertainty of the tropical mean, $u_{\mathrm{com,trop}}$, is the mean of the common uncertainties of the individual grid cells $u_{\mathrm{com},j}$, also weighted with $\cos(lat_j)$:

$$u_{\mathrm{com,trop}} = \frac{\sum_{j=1}^{N_{\mathrm{cells}}} \cos(lat_j)\, u_{\mathrm{com},j}}{\sum_{j=1}^{N_{\mathrm{cells}}} \cos(lat_j)}. \tag{5.12}$$

Again, to be conservative it is recommended to treat the structured uncertainties the same as the common uncertainties. The total uncertainty of the tropical average $u_{\mathrm{tot,trop}}$ is obtained as follows:

$$u_{\mathrm{tot,trop}} = \sqrt{u^2_{\mathrm{ind,trop}} + u^2_{\mathrm{struct,trop}} + u^2_{\mathrm{com,trop}}}. \tag{5.13}$$

In Figure 5.11, this total uncertainty is depicted as a shaded area around the time series of each satellite mission. As explained in the previous section, common uncertainties represent the largest part of the total uncertainties, because they are not reduced by the averaging. In most cases, the time series of different satellite missions agree within their uncertainties. However, there are exceptions, particularly in the early satellite missions with the SSMT-2 instrument. The differences between those satellite missions are most-likely caused by other factors like the sparse sampling, which will be discussed in the next section. Generally, it is important to note that the uncertainty shown here is only the uncertainty associated with the measurement of BT that was propagated from the FCDR. There are additional sources of uncertainty that emerge during the CDR processing. These are discussed in the following section.

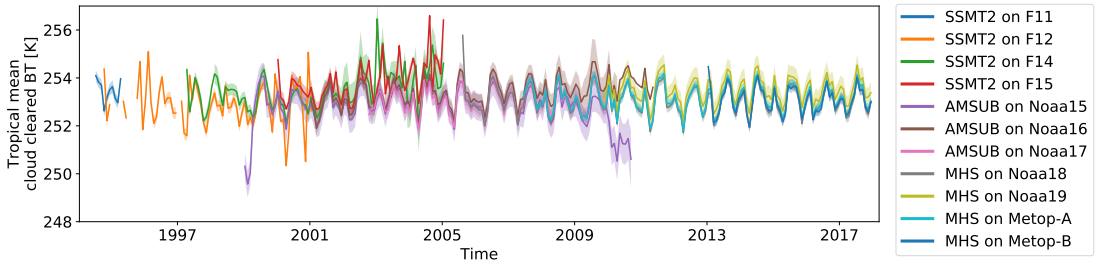

Figure 5.11: Tropical area-weighted mean of cloud filtered BT for all available satellite missions of the UTH CDR. The range of $\pm$ one measurement uncertainty is indicated as shaded area around the monthly means.

5.4 Sources of uncertainty at CDR level

A major achievement of the UTH CDR is the fact that it contains uncertainty information, which is needed to express trust in the data. The uncertainties that are contained in the UTH CDR have been propagated from the FCDR. They are associated with the measurement of brightness temperature. However, there are additional uncertainties,

which arise during the level 2 and level 3 processing and can have a significant effect on the UTH climatology. These uncertainties are not included in the CDR since a full understanding and quantification would require thorough investigations, which were not possible in the time period available to create the CDR and should hence be part of future work. This section provides an overview of the additional uncertainties as well as a suggestion on how to estimate their magnitude, where possible. A detailed discussion of the uncertainties is also provided in the UTH CDR Uncertainty Report, which is part of the supporting documentation of the UTH CDR.

5.4.1 Uncertainties arising at level 2

Uncertainties at level 2 mainly result from the fact that the BT transformation method is not perfect. In the real atmosphere, there are deviations from the linear relationship between brightness temperature and the logarithm of UTH. One way to estimate the resulting uncertainty in the monthly gridded UTH values in the CDR is by using the retrieval standard deviation $\sigma_{\Delta UTH}$, which was determined in Section 3.4 from simulated AMSU-B BTs for the Eresmaa data set (Figure 3.7). The overall retrieval standard deviation is 3.2% RH, but it varies over the range of possible UTH values. Values of $\sigma_{\Delta UTH}$ for UTH bins of 10% are provided in Table 5.3. These can be used to estimate the uncertainty of UTH due to deviations from the linear relationship between BT and the logarithm of UTH. However, it should be noted that this is a simplified approach, since the grid cell averages of UTH in the CDR are a combination of several instantaneous UTH values, which all have different uncertainties. A comparison of the uncertainty estimates given in Table 5.3 with the histograms in Figure 5.10 shows that the estimated uncertainty resulting from assuming a linear relationship between BT and $ln(UTH)$ is already larger than the typical measurement uncertainties of monthly averages at grid cell level, particularly for high UTH values. However, when assuming that the deviations from the linear relationship are random, one can argue that the resulting uncertainty is reduced when further temporal or spatial averaging is performed, whereas the common uncertainties are not reduced.

5.4.2 Uncertainties arising at level 3

Additional uncertainties at level 3 arise from the fact that the monthly average of UTH and BT is determined from a few satellite overpasses only and therefore differs from the true monthly average. From Figure 5.9 it is apparent that a certain point in the

Table 5.3: UTH retrieval standard deviation $\sigma_{\Delta UTH}$ for UTH bins of 10%, which can be used to estimate the uncertainty of UTH associated with the exponential UTH model. The values for $\sigma_{\Delta UTH}$ are based on simulations of AMSU-B BTs for the Eresmaa data set and are equal to those shown in Figure 3.7.

UTH bins	$\sigma_{\Delta UTH}$ **[% RH]**
0-10%	0.8
10-20%	1.8
20-30%	2.3
30-40%	2.6
40-50%	2.7
50-60%	3.4
60-70%	3.8
70-80%	5.7
80-90%	6.2
90-100%	16.0

tropics is usually observed not more than about six times per month by ascending satellite overpasses. Simplified, the uncertainty resulting from the sparse sampling u_{sampling} of the monthly average can be estimated from the standard deviation of the daily averages s and the number of satellite overpasses N_t:

$$u_{\mathrm{sampling}} = \frac{s}{\sqrt{N_t}}. \tag{5.14}$$

A problem with this method is that it implies that the measured values vary randomly. Variations in the atmosphere are, however, systematic rather than random. Hence, rather than assigning an uncertainty resulting from the sparse sampling, months with generally few satellite overpasses should be used with caution or even be excluded when a climatology of UTH or BT is created. One possibility to identify such months is to use the average number of satellite overpasses per month and per grid cell. This is shown in Figure 5.12 for all satellite missions in the CDR. For the AMSU-B and MHS missions, apart from a few exceptions, the satellites pass each grid cell on average about 12 to 13 times per month. In the earlier SSMT-2 missions, however, large data gaps lead to a poorer sampling. In all four of the missions there are months with less than one average satellite overpass per grid cell. Thus, the time period before 1999, in which only SSMT-2 observations are available, should be used very cautiously.

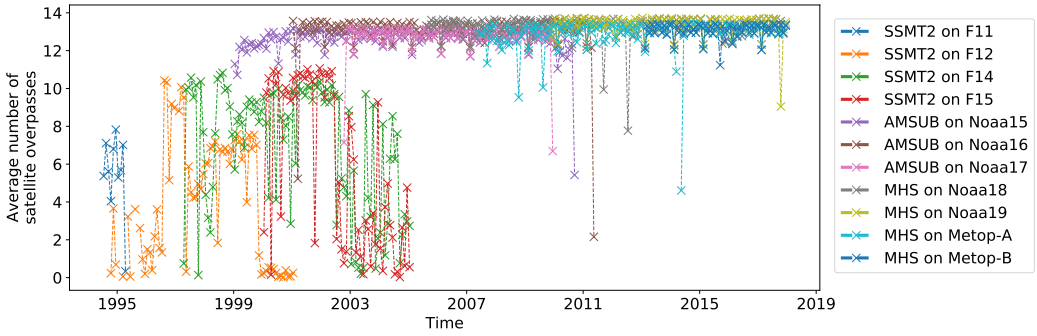

Figure 5.12: Average number of satellite overpasses per grid cell and month for each satellite mission in the UTH CDR.

A related uncertainty results from the sun-synchronous orbit of the satellites (Section 2.2.3). In this orbit, the satellites always pass a given point on Earth at the same local time. This means that they always observe the same phase of the diurnal cycle. Thus, the monthly averages derived from these observations are actually only valid for a certain time of day. The resulting uncertainty depends on the amplitude of the diurnal cycle of BT, which is largest in convective regions. Kottayil et al. (2013) found diurnal amplitudes on the order of 1 K over the ocean and diurnal amplitudes exceeding 3 K over some convective regions over land. These numbers provide an upper limit for the uncertainty resulting from the diurnal cycle. Estimating the uncertainty more precisely or even correcting for the diurnal cycle is not possible, because this would require an exact knowledge of the temporal course of the diurnal cycle. To reduce the uncertainty due to the diurnal cycle in the monthly averages of BT and UTH, the averages from ascending and descending satellite overpasses should always be combined. Moreover, when monthly averages from multiple satellite missions with different equator-crossing times are available, they should also be combined in order to get a better sampling of the diurnal cycle. An overview of the equator-crossing times of all satellites included in the UTH CDR is given in Figure 5.13.

Connected to the uncertainty associated with the sampling of the diurnal cycle is the uncertainty that results from a potential orbit drift of the satellite. With the exception of Metop-A and Metop-B, which are actively stabilised, all satellites included in the UTH CDR are subject to an orbit drift. This drift is apparent from the change in the equator-crossing times over time (Figure 5.13). As a consequence of the drift, the observed phase of the diurnal cycle changes over time. Such an aliasing of the diurnal cycle can lead to artificial trends when long time scales are analysed. However, a comparison of the monthly mean

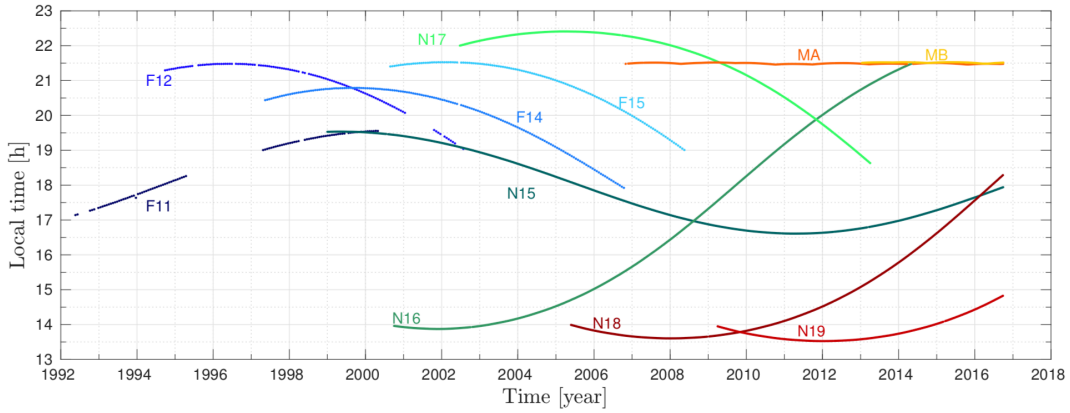

Figure 5.13: Equator-crossing times of ascending passes of all satellites included in the UTH CDR. Labels starting with N denote the NOAA satellites (NOAA15-NOAA19), MA and MB denote the satellites Metop-A and Metop-B, respectively. Figure courtesy Imke Hans.

BTs measured by the stabilised satellite Metop-A with BTs measured by the drifting satellite NOAA18 (Figure 5.11) suggests that these artificial trends are small. In the same time period from 2007 to 2017, the linear trends of the Metop-A and NOAA18 BTs are 0.049 K (-0.701% RH) per decade and 0.002 K per decade, respectively. Hence, the trends differ by less than 0.05 K per decade. Nonetheless, one should always compare trends obtained from ascending and descending satellite overpasses as well as from overlapping satellite missions with different equator-crossing times, in order to identify trends that might result from an orbit drift.

Another problem one should be aware of is the dry bias in UTH that results from the cloud filtering. Since clouds are associated with high values of RH, removing cloud contaminated data introduces a dry bias or clear-sky bias in the retrieved UTH climatology. In monthly averages of UTH that is derived from microwave observations, Buehler et al. (2007) estimate the dry bias to about 2-3% RH in regions with deep convective clouds (see their Figure 5). This dry bias is small compared to infrared observations of UTH, which are more strongly affected by clouds.
To illustrate this dry bias in the UTH CDR, the difference between monthly tropical mean BT_{filtered} and BT_{full} is plotted in Figure 5.14 for all satellite missions. For most of the instruments BT_{filtered} is about 0.2 K warmer than BT_{full}. This corresponds to a fractional bias of about -2% in the tropical mean UTH. However, for some instruments the difference between BT_{filtered} and BT_{full} is significantly larger. Affected instruments

are SSMT-2 on F14 (after 2001), AMSU-B on NOAA15 (whole mission), AMSU-B on NOAA16 (after 2006) and MHS on NOAA19 (whole mission). In order to avoid time dependent biases when a climatological time series is created, the above-named satellite missions should not be used in the affected time periods.

The reason for the large differences between BT_{filtered} and BT_{full} can be explained by comparing Figure 5.14 to the noise performance of the instruments, which was investigated by Hans et al. (2017). The affected time periods are identical to those periods in which the noise performance of the 183.31±1 GHz channels of the respective instruments are poorest. As a consequence of the strong instrumental noise, the distribution of the measured BTs is broader than for instruments with less noise. During the cloud filtering, BTs below a fixed threshold are cut off. For the instruments with strong noise this leads to a larger change in the mean BT and hence to an increased dry bias in the mean UTH compared to the other instruments. A schematic illustration of how the cloud filtering affects the mean value of a measured distribution is shown in Figure 5.15. An exception is AMSU-B on NOAA15, for which BT_{full} becomes warmer than BT_{filtered} after 2009. This could be related to the BT in the 183.31±3 GHz channel, which is used as an additional threshold in the cloud filtering (Section 5.2.1). The noise in this channel also strongly increases in the affected time period (Hans et al., 2017) and possibly leads to a decrease in BT_{filtered}.

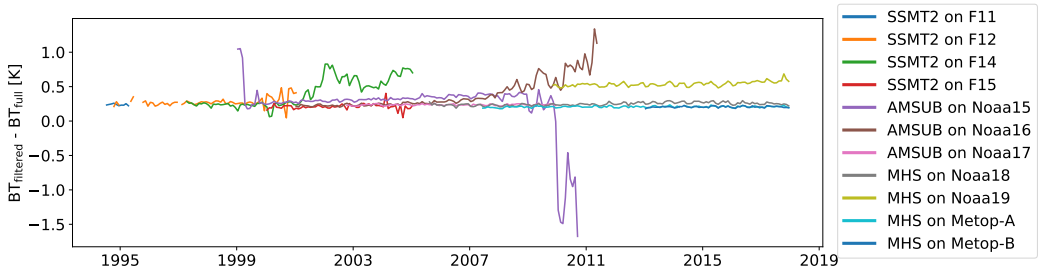

Figure 5.14: Difference between monthly, area-weighted tropical means of cloud filtered brightness temperature BT_{filtered} and unfiltered brigthness temperature BT_{full} for all satellite missions included in the UTH CDR.

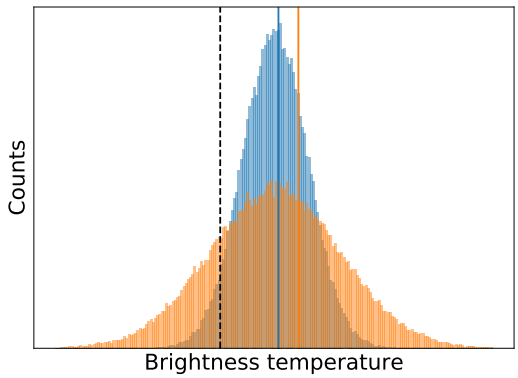

Figure 5.15: Schematic illustration of the impact of a cloud filter on the mean values of two BT distributions with different variances. The distribution with higher variance (orange) represents the distribution measured by an instrument with high noise. Cutting off all values below a certain threshold (black dashed line) results in a higher mean value for the distribution with high variance (orange line) than for the distribution with lower variance (blue line).

5.5 Conclusion: A guideline for the creation of a UTH time series

The above sections revealed a series of problems, which induce uncertainties on the climatology of BT and UTH. The question is now how to make use of these findings when using the CDR data for climate research. The following points provide a guideline for the creation of a climatological time series of tropical mean UTH or BT from the CDR data:

- Combine monthly averages of BT/UTH from ascending and descending satellite overpasses in order to improve the sampling of the diurnal cycle
- Create a time series of area-weighted tropical means of BT/UTH for every satellite mission (as explained in Section 5.3.4)
- Combine the time series of all available satellite missions with different equator crossing times in order to obtain one long-term time series of BT/UTH with a best possible sampling of the diurnal cycle. Do not include data from instruments with poor noise performance, particularly when cloud filtered BT or UTH are analysed. A recommendation of missions and time ranges to use is given in Table 5.4, which is based on Figure 5.14.

- Propagate measurement uncertainties to the tropical means for each satellite mission (as explained in Section 5.3.4). When combining the time series of overlapping satellite missions to one time series, all three classes of uncertainties can be treated as independent, since all effects are instrument-specific.

Table 5.4: Recommendation of time periods to use for the generation of a climatological time series of BT or UTH. Time periods were excluded where high instrumental noise leads to a difference between BT_{filtered} and BT_{full} (Figure 5.14) that is larger than 0.3 K (or negative in the case of NOAA15).

Instrument	Satellite	Start	End
SSMT-2	DMSP F11	07/1994	04/1995
SSMT-2	DMSP F12	10/1994	10/1999
SSMT-2	DMSP F14	04/1997	03/2001
SSMT-2	DMSP F15	01/2000	01/2004
AMSU-B	NOAA15	04/1999	03/2002
AMSU-B	NOAA16	01/2001	02/2007
AMSU-B	NOAA17	10/2002	12/2009
MHS	NOAA18	08/2005	12/2017
MHS	NOAA19	-	-
MHS	Metop-A	06/2007	12/2017
MHS	Metop-B	01/2013	12/2017

Figure 5.16 shows time series of BT_{full}, BT_{filtered} and UTH that were created according to the instructions above. Uncertainties are generally smaller in time periods for which a bigger number of satellite missions are available. However, considering only the uncertainties propagated from the FCDR is not enough. Even though there are several SSMT-2 missions available in the years before 1999 and their combined measurement uncertainty is small, it is recommended not to use this part of the time series for a trend analysis due to large data gaps in these missions (Figure 5.12). Moreover, there might be residual trends in the time series, which are caused by drifts of the satellite orbits. Different trends in time series derived from only ascending and only descending satellite overpasses and from overlapping satellite missions with different equator crossing times can be an indication for that. However, such artificial trends are estimated to be smaller than 0.05 K per decade (Section 5.4.2). Moreover, as pointed out in Chapter 4, UTH is influenced by other factors than RH. When these factors change in a warming climate, UTH can change even though RH stays constant. This should always be kept in mind when long-term trends of UTH are analysed.

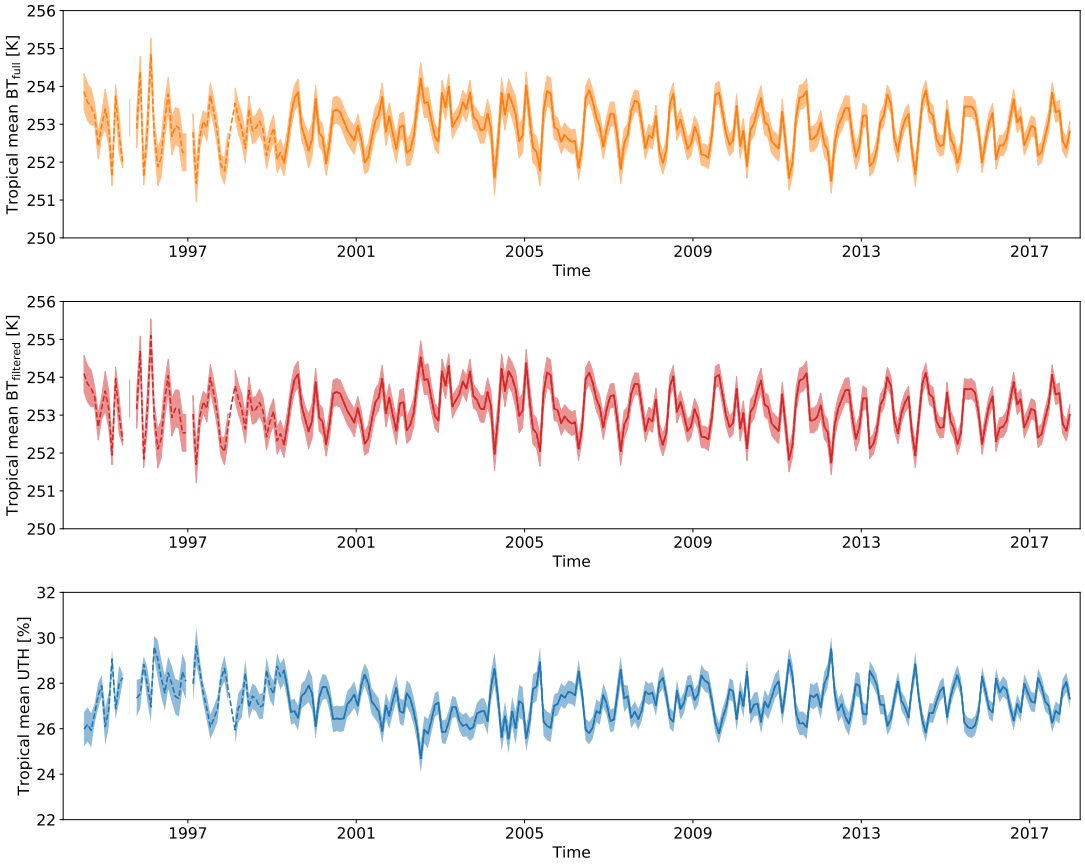

Figure 5.16: Combined time series of tropical, area-weighted mean BT_{full} (upper panel), BT_{filtered} (middle panel) and UTH (lower panel) from all satellite missions listed in Table 5.4. The shaded areas display $\pm$ one measurement uncertainty (propagated from the FCDR) around each tropical mean value. The time period before 1999 is plotted as dashed line, because there are significant data gaps in this period and it should hence not be used for a trend analysis.

CHAPTER 6

Summary and outlook

Upper Tropospheric Humidity (UTH) plays an important role in controlling the longwave radiation emitted to space. Therefore, stable, long-term observational data records of UTH are needed to investigate the evolution of UTH in a warming climate and to evaluate climate model simulations. The generation of such a Climate Data Record (CDR) of UTH from satellite-borne observations is one of the aims of the Horizon 2020 project FIDUCEO, which this thesis was part of. The following aspects represent the most important innovations of the FIDUCEO UTH CDR:

- It is based on the FIDUCEO Microwave Fundamental Climate Data Record (FCDR), which uses an improved recalibration approach that significantly reduces the biases between individual instruments
- It includes metrologically traceable measurement uncertainties and additional uncertainties are discussed in the supporting documentation
- A new definition of UTH is used, which will allow a direct comparison to UTH derived from HIRS brightness temperatures in future

The first two aspects address major problems of most existing CDRs: There are significant biases between the measurements of consecutive satellite missions and no uncertainty information is provided, although in a metrological sense a measurement is only complete with its uncertainty. The third aspect is an attempt to solve a problem specifically related to UTH. The quantity can be derived from BT measured either in IR or MW water vapour channels probing the upper troposphere. However, IR and MW UTH cannot be directly compared due to the definition of UTH, which depends on the specific instrument used to measure BT. Therefore, this thesis introduced a new UTH definition that

is identical for the UTH channels of the HIRS/2 instrument and the MW sounders MHS, AMSU-B and SSMT-2. This will allow the combination of all satellite missions carrying these instruments to create a 40 year time series of UTH.

The new UTH definition was introduced in Chapter 3 of this thesis. According to this definition, UTH is the RH averaged over an atmospheric layer - the UTH layer - that is bounded by two characteristic water vapour overburdens. It was shown that the same characteristic water vapour columns (called IWV thresholds) can be chosen for the 6.72 µm channel and the 183.31±1 GHz channel, so that UTH derived from HIRS/2 will be directly comparable to UTH derived from MHS, AMSU-B and SSMT-2. The new definition has an additional benefit: Calculating UTH from model atmospheres with the new definition only requires atmospheric profiles of relative and absolute humidity, but no radiative transfer simulations. Moreover, a comparison with the traditional UTH definition showed that the performance of the UTH retrieval does not suffer from the new definition. Retrieval bias and standard deviation are of similar magnitude for the traditional and the new definition.

A problem that remains with the new definition of UTH is the fact that the BT measured in a UTH channel is influenced by other factors than RH. When these factors change in a warming climate this causes trends in BT and the derived UTH, which conceal the actual trend of RH. An important factor that was identified in Chapter 4 of this thesis is a shift in the emission layer towards lower pressures as the atmosphere warms. At a lower pressure, the water vapour absorption lines get narrower. This particularly influences the BT in the 6.72 µm channel. The impact of this effect on the evolution of the observed UTH in a warming climate was shown by simulating IR and MW BTs for atmospheric profiles in the CMIP5 1%CO_2 run of the MPI-ESM-LR model and comparing the derived UTH to the true UTH of the profiles. While both the true UTH and the fitted UTH from MW BTs show a small positive trend of about 0.1% RH per decade, the fitted UTH from IR BTs exhibits a negative trend of about -0.4% RH per decade. This negative trend is most likely caused by the upward-shift of the UTH layer, but not by a change in RH. In order to avoid wrong conclusions about the evolution of RH, it is recommended to look at the evolution of BT rather than UTH. A possible way to solve the problem in the future is to adapt the BT transformation method for IR BTs by re-introducing a pressure parameter, similar to the one introduced by Soden and Bretherton (1993). However, this means that additional measurements, e.g. from other instrument channels, will be needed to determine the pressure parameter. Generally, future research should focus on revealing and understanding all factors influencing the BT in the different UTH channels,

so that the right conclusions can be drawn from measurements of BT.

The new UTH definition was applied in Chapter 5, where the processing of the FIDUCEO Microwave UTH CDR is described. It covers the time period from 1994 to 2017 and contains two core variables: monthly mean 183.31$\pm$1 GHz brightness temperatures and UTH. The variables are mapped on a regular latitude-longitude grid that covers the tropical region with a resolution of 1°x1°. As soon as a FIDUCEO HIRS FCDR with sufficient quality is available, a HIRS UTH CDR should be created. Then it can be evaluated how well the new UTH definition serves its purpose and HIRS observations can be used to complement the UTH time series from MW observations and expand it to earlier years.

A key feature of the new UTH CDR is the fact that it contains an estimation of the uncertainty associated with the measurement for every grid cell value. This uncertainty was propagated from the FCDRs and is split into three different classes: Independent, structured and common uncertainties. The three types differ in their correlation structures and therefore have to be treated differently in averaging processes. However, it has been shown that it is not sufficient to only consider the measurement uncertainty, because there are additional uncertainties arising at CDR level. Quantifying these additional uncertainties to a degree that allows to explicitly include them into the CDR was not possible in the time available for this thesis. This requires detailed investigations, which should be part of future work. Instead, the additional uncertainties are discussed in the supporting documentation of the CDR and in this thesis to make the user aware of them.

Since most of the uncertainties can be reduced through averaging, an obvious application of the CDR is the creation of a time series of tropical, monthly averages of BT and UTH. A guideline for this was given in Section 5.5. Most importantly, data from overlapping satellite missions with different equator crossing times should be combined in order to improve the sampling of the diurnal cycle. Furthermore, when looking at cloud filtered quantities, the user is advised to not use measurements from instruments with poor noise performance, because these measurements are biased. Moreover, data from the early SSMT-2 missions should be used with caution due to poor coverage.

As an overall conclusion, it can be said that the new UTH definition introduced in this thesis will allow a synergistic view on infrared and microwave UTH in the future. With the creation of the FIDUCEO microwave UTH CDR, the first step towards a combined infrared and microwave UTH data record has been taken. Such a joint data record has the potential to shed new light on the long-term evolution of UTH.

CHAPTER 7

Appendices

7.1 UTH scaling coefficients

The UTH scaling coefficients derived from the 137-level ECMWF data set for each viewing angle of AMSU-B, MHS and HIRS are listed in table 7.1. These coefficients have been used to scale BT to UTH in the FIDUCEO UTH CDR.

Table 7.1: Scaling coefficients derived from the 137-level ECMWF data set for each viewing angle of AMSU-B, MHS and HIRS, respectively.

AMSU-B			MHS			HIRS		
Viewing angle [°]	a	b	Viewing angle [°]	a	b	Viewing angle [°]	a	b
179.45	22.4942	-0.0950	179.4444	22.5022	-0.0951	179.1	29.6040	-0.1260
178.35	22.4944	-0.0950	178.3333	22.5025	-0.0951	177.3	29.6143	-0.1261
177.25	22.4947	-0.0950	177.2222	22.5027	-0.0951	175.5	29.6170	-0.1261
176.15	22.4952	-0.0950	176.1111	22.5031	-0.0951	173.7	29.6244	-0.1261
175.05	22.4956	-0.0950	175.0000	22.5038	-0.0951	171.9	29.7322	-0.1266
173.95	22.4959	-0.0951	173.8889	22.5041	-0.0951	170.1	29.9528	-0.1275
172.85	22.4966	-0.0951	172.7778	22.5048	-0.0951	168.3	29.9779	-0.1277
171.75	22.4972	-0.0951	171.6667	22.5054	-0.0951	166.5	29.9940	-0.1278
170.65	22.4988	-0.0951	170.5556	22.5072	-0.0952	164.7	30.0087	-0.1279
169.55	22.5008	-0.0951	169.4445	22.5093	-0.0952	162.9	30.0238	-0.1280
168.45	22.5026	-0.0952	168.3333	22.5108	-0.0952	161.1	30.0410	-0.1281
167.35	22.5047	-0.0952	167.2222	22.5133	-0.0952	159.3	30.0596	-0.1282
166.25	22.5073	-0.0952	166.1111	22.5158	-0.0953	157.5	30.1466	-0.1287
165.15	22.5104	-0.0953	165.0000	22.5194	-0.0953	155.7	30.2235	-0.1291
164.05	22.5139	-0.0953	163.8889	22.5223	-0.0954	153.9	30.3488	-0.1297
162.95	22.6439	-0.0959	162.7778	22.6529	-0.0959	152.1	30.3812	-0.1299
161.85	22.6481	-0.0959	161.6667	22.6574	-0.0960	150.3	30.3200	-0.1297
160.75	22.6525	-0.0960	160.5556	22.6619	-0.0960	148.5	30.3598	-0.1300
159.65	22.6637	-0.0961	159.4445	22.6733	-0.0961	146.7	30.4123	-0.1304
158.55	22.6680	-0.0961	158.3334	22.6778	-0.0962	144.9	30.4927	-0.1308
157.45	22.6786	-0.0962	157.2222	22.6882	-0.0963	143.1	30.5393	-0.1312
156.35	22.7997	-0.0968	156.1111	22.8108	-0.0968	141.3	30.5333	-0.1313
155.25	22.9909	-0.0976	155.0000	23.0034	-0.0977	139.5	30.6151	-0.1318
154.15	23.0230	-0.0978	153.8889	23.0349	-0.0978	137.7	30.5528	-0.1318
153.05	23.0389	-0.0979	152.7778	23.0514	-0.0980	135.9	30.7128	-0.1327
151.95	23.0533	-0.0980	151.6667	23.0663	-0.0981	134.1	30.7704	-0.1332
150.85	23.0695	-0.0982	150.5556	23.0833	-0.0982	132.3	31.0615	-0.1347
149.75	23.0894	-0.0983	149.4445	23.1034	-0.0984	130.5	31.0902	-0.1351
148.65	23.1076	-0.0985	148.3334	23.1244	-0.0985			
147.55	23.1930	-0.0989	147.2223	23.2098	-0.0990			
146.45	23.2621	-0.0992	146.1111	23.2783	-0.0993			
145.35	23.3854	-0.0998	145.0000	23.4048	-0.0999			
144.25	23.4157	-0.1000	143.8889	23.4379	-0.1002			
143.15	23.4103	-0.1001	142.7778	23.4334	-0.1002			
142.05	23.4421	-0.1004	141.6667	23.4678	-0.1005			
140.95	23.4965	-0.1007	140.5556	23.5235	-0.1008			
139.85	23.5671	-0.1011	139.4445	23.5958	-0.1012			
138.75	23.6226	-0.1014	138.3334	23.6560	-0.1016			
137.65	23.6239	-0.1015	137.2223	23.6585	-0.1017			
136.55	23.6886	-0.1019	136.1112	23.7270	-0.1021			
135.45	23.6495	-0.1019	135.0000	23.6908	-0.1022			
134.35	23.7903	-0.1027	133.8889	23.8373	-0.1029			
133.25	23.8228	-0.1030	132.7778	23.8799	-0.1033			
132.15	24.0405	-0.1041	131.6667	24.1042	-0.1044			
131.05	24.0674	-0.1044	130.5556	24.1406	-0.1048			

7.2 CDR variables

All variables contained in the FIDUCEO UTH CDR are listed in Table 7.2.

Table 7.2: List of names, descriptions, dimensions and units of all variables contained in the UTH CDR. Dimension x has size 360 and is the east-west dimension, y has size 61 and is the north-south dimension and bounds has size 2 and is the dimension defining lower and upper bounds.

Variable Name	Description	Dimensions	Unit
lat	Geographical latitudes of grid cell centers	y	Degree north
lat_bnds	Geographical latitudes of grid cell boundaries	y, bounds	Degree north
lon	Geographical longitudes of grid cell centers	x	Degree east
lon_bnds	Geographical longitudes of grid cell boundaries	x, bounds	Degree east
time_ranges_ascend	Minimum and maximum seconds of day pixel contribution time for ascending nodes	x, y	s
time_ranges_descend	Minimum and maximum seconds of day pixel contribution time for descending nodes	x, y	s
observation_count_ascend	Number of UTH/brightness temperature observations (= number of pixels contributing to the average) in a grid box for ascending passes	x, y	1
observation_count_descend	Number of UTH/brightness temperature observations (= number of pixels contributing to the average) in a grid box for descending passes	x, y	1
observation_count_all_ascend	Number of brightness temperature observations in a grid box when no cloud filtering is done for ascending passes	x, y	1
observation_count_all_descend	Number of brightness temperature observations in a grid box when no cloud filtering is done for descending passes	x, y	1
overpass_count_ascend	Number of satellite overpasses in a grid box for ascending passes	x, y	1
overpass_count_descend	Number of satellite overpasses in a grid box for descending passes	x, y	1
BT_ascend	Monthly average of all brightness temperatures which were used to retrieve	x, y	K

	UTH in a grid box for ascending passes (calculated from daily averages)		
BT_descend	Monthly average of all brightness temperatures which were used to retrieve UTH in a grid box for descending passes (calculated from daily averages)	x, y	K
BT_inhomogeneity_ascend	Standard deviation of all daily mean brightness temperatures which were used to retrieve UTH in a grid box for ascending passes	x, y	K
BT_inhomogeneity_descend	Standard deviation of all daily mean brightness temperatures which were used to retrieve UTH in a grid box for descending passes	x, y	K
u_independent_BT_ascend	Uncertainty of monthly mean brightness temperature due to independent effects for ascending passes	x, y	K
u_independent_BT_descend	Uncertainty of monthly mean brightness temperature due to independent effects for descending passes	x, y	K
u_structured_BT_ascend	Uncertainty of monthly mean brightness temperature due to structured effects for ascending passes	x, y	K
u_structured_BT_descend	Uncertainty of monthly mean brightness temperature due to structured effects for descending passes	x, y	K
u_common_BT_ascend	Uncertainty of monthly mean brightness temperature due to common effects for ascending passes	x, y	K
u_common_BT_descend	Uncertainty of monthly mean brightness temperature due to common effects for descending passes	x, y	K
BT_full_ascend	Monthly average of all daily mean brightness temperatures – including cloudy pixels - in a grid box for ascending passes	x, y	K
BT_full_descend	Monthly average of all daily mean brightness temperatures – including	x, y	K

	cloudy pixels - in a grid box for descending passes		
BT_full_inhomogeneity_ascend	Standard deviation of all daily mean brightness temperatures – including cloudy pixels - in a grid box for ascending passes	x, y	K
BT_full_inhomogeneity_descend	Standard deviation of all daily mean brightness temperatures – including cloudy pixels - which were used to retrieve UTH in a grid box for descending passes	x, y	K
u_independent_BT_full_ascend	Uncertainty of monthly mean brightness temperature including cloudy pixels due to independent effects for ascending passes	x, y	K
u_independent_BT_full_descend	Uncertainty of monthly mean brightness temperature including cloudy pixels due to independent effects for descending passes	x, y	K
u_structured_BT_full_ascend	Uncertainty of monthly mean brightness temperature including cloudy pixels due to structured effects for ascending passes	x, y	K
u_structured_BT_full_descend	Uncertainty of monthly mean brightness temperature including cloudy pixels due to structured effects for descending passes	x, y	K
u_common_BT_full_ascend	Uncertainty of monthly mean brightness temperature including cloudy pixels due to common effects for ascending passes	x, y	K
u_common_BT_full_descend	Uncertainty of monthly mean brightness temperature including cloudy pixels due to common effects for descending passes	x, y	K
uth_ascend	Monthly average of all UTH retrievals in a grid box for ascending passes	x, y	%
uth_descend	Monthly average of all UTH retrievals in a grid box for descending passes	x, y	%
uth_inhomogeneity_ascend	Standard deviation of all daily UTH averages that were used to calculate the monthly UTH average in a grid box for ascending passes	x, y	%
uth_inhomogeneity_descend	Standard deviation of all daily UTH averages that were used to calculate the	x, y	%

	monthly UTH average in a grid box for descending passes		
u_independent_uth_ascend	Uncertainty of monthly mean UTH due to independent effects for ascending passes	x, y	%
u_independent_uth_descend	Uncertainty of monthly mean UTH due to independent effects for descending passes	x, y	%
u_structured_uth_ascend	Uncertainty of monthly mean UTH due to structured effects for ascending passes	x, y	%
u_structured_uth_descend	Uncertainty of monthly mean UTH due to structured effects for descending passes	x, y	%
u_common_uth_ascend	Uncertainty of monthly mean UTH due to common effects for ascending passes	x, y	%
u_common_uth_descend	Uncertainty of monthly mean UTH due to common effects for descending passes	x, y	%

Bibliography

J. J. Bates. Trends in upper-tropospheric humidity. *Geophysical Research Letters*, 28(9): 1695–1698, 2001. doi: 10.1029/2000GL012544.

A. Bobryshev. Frequency grid setups for microwave radiometers AMSU-A and AMSU-B. Technical report, Universität Hamburg, 2015.

S. A. Buehler. Orbit drift and diurnal cycle aliasing. `http://www.fiduceo.eu/content/orbit-drift-and-diurnal-cycle-aliasing`, 2016. Last access: 22 November 2018.

S. A. Buehler and V. O. John. A simple method to relate microwave radiances to upper tropospheric humidity. *Journal of Geophysical Research*, 110:D02110, 2005. doi: 10.1029/2004JD005111.

S. A. Buehler, P. Eriksson, T. Kuhn, A. von Engeln, and C. Verdes. ARTS, the Atmospheric Radiative Transfer Simulator. *Journal of Quantitative Spectroscopy and Radiative Transfer*, 91(1):65–93, 2005. doi: 10.1016/j.jqsrt.2004.05.051.

S. A. Buehler, M. Kuvatov, T. R. Sreerekha, V. O. John, B. Rydberg, P. Eriksson, and J. Notholt. A cloud filtering method for microwave upper tropospheric humidity measurements. *Atmospheric Chemistry and Physics*, 7:5531–5542, 2007. doi: 10.5194/acp-7-5531-2007.

S. A. Buehler, M. Kuvatov, V. O. John, M. Milz, B. J. Soden, D. L. Jackson, and J. Notholt. An upper tropospheric humidity data set from operational satellite microwave data. *Journal of Geophysical Research*, 113:D14110, 2008. doi: doi:10.1029/2007JD009314.

S. A. Buehler, V. O. John, A. Kottayil, M. Milz, and P. Eriksson. Efficient radiative transfer simulations for a broadband infrared radiometer—Combining a weighted mean of representative frequencies approach with frequency selection by simulated annealing. *Journal of Quantitative Spectroscopy and Radiative Transfer*, 111(4):602–615, 2010. doi: 10.1016/j.jqsrt.2009.10.018.

W. P. Elliot and D. J. Gaffen. On the Utility of Radisonde Humidity Archives for Climate Studies. *Bulletion of the American Meteorological Society*, 72:1507–1520, 1991. doi: 10.1175/1520-0477(1991)072<1507:OTUORH>2.0.CO;2.

R. Eresmaa and A. P. McNally. Diverse profile datasets from the ECMWF 137-level short-range forecasts. Technical report, European Centre for Medium-range Weather Forecasts, 2014.

P. Eriksson, S. A. Buehler, C. P. Davis, and O. Lemke. ARTS, the atmospheric radiative transfer simulator, version 2. *Journal of Quantitative Spectroscopy and Radiative Transfer*, 112(10):1551–1558, 2011. doi: 10.1016/j.jqsrt.2011.03.001.

EUMETSAT-webpage. Satellite orbits. `https://www.eumetsat.int/website/home/Satellites/LaunchesandOrbits/SatelliteOrbits/index.html`, 2018. Last access: 22 November 2018.

FIDUCEO-webpage. Tutorials - Error and uncertainty. `http://www.fiduceo.eu/tutorial/error-and-uncertainty`, 2018.

M. A. Giorgetta, J. Jungclaus, C. H. Reick, S. Legutke, J. Bader, M. Böttinger, V. Brovkin, T. Crueger, M. Esch, K. Fieg, K. Glushak, V. Gayler, H. Haak, H.-D. Hollweg, T. Ilyina, S. Kinne, L. Kornblueh, D. Matei, T. Maruitsen, U. Mikolajewicz, W. Mueller, D. Notz, F. Pithan, T. Raddatz, S. Rast, R. Redler, E. Roeckner, H. Schmidt, R. Schnur, J. Segschneider, K. D. Six, M. Stockhause, C. Timmreck, J. Wegner, H. Widmann, K.-H. Wieners, M. Claussen, J. Marotzke, and B. Stevens. Climate and carbon cycle changes from 1850 to 2100 in MPI-ESM simulations for the Coupled Model Intercomparison Project phase 5. *Journal of Advances in Modeling Earth Systems*, 5(3):572–597, 2013. doi: 10.1002/jame.20038.

T. J. Greenwald and S. A. Christopher. Effect of cold clouds on satellite measurements near 183 GHz. *Journal of Geophysical Research*, 107(D13):4170, 2002. doi: 10.1029/2000JD000258.

GUM. Evaluation of measurement data — Guide to the expression of uncertainty in measurement (GUM) JCGM 100:2008. Technical report, Joint Committee for Guides in Metrology (JCGM), 2008. URL `https://www.bipm.org/en/publications/guides/`.

I. Hans. *Towards a new fundamental climate data record for microwave humidity sounders based on metrological best practice*. PhD thesis, University of Hamburg, 2018.

I. Hans, M. Burgdorf, V. O. John, J. Mittaz, and J. A. Buehler. Noise performance of microwave humidity sounders over their lifetime. *Atmospheric Measurement Techniques*, 10:4927–4945, 2017. doi: 10.5194/amt-10-4927-2017.

I. Hans, M. Burgdorf, and E. Woolliams. Product user guide - Microwave FCDR release 0.2. Technical report, University of Hamburg and National Physical Laboratory, 2018.

I. Hans, M. Burgdorf, S. Buehler, M. Prange, T. Lang, and V. John. An Uncertainty Quantified Fundamental Climate Data Record for Microwave Humidity Sounders. *Remote Sensing*, 11(5):548, 2019. doi: 10.3390/rs11050548.

I. M. Held and B. J. Soden. Water Vapor Feedback and Global Warming. *Annual Review of Energy and the Environment*, 25:441–475, 2000. doi: 10.1146/annurev.energy.25.1.441.

J. Hocking, P. Roquet, and P. Brunel. Python/C/C++ wrapperfor RTTOV v12. Technical report, EUMETSAT NWP SAF, 2018. URL `https://www.nwpsaf.eu/site/download/documentation/rtm/docs_rttov12/rttov-wrapper.pdf`.

T. Ilyina, K. D. Six, J. Segschneider, E. Maier-Reimer, H. Li, and I. Nú nez Riboni. Global ocean biogeochemistry model HAMOCC: Model architecture and performance as component of the MPI-Earth system model in different CMIP5 experimental realizations. *Journal of Advances in Modeling Earth Systems*, 5(2):287–315, 2013. doi: 10.1029/2012MS000178.

IPCC. *Climate Change 2013: The Physical Science Basis. Contribution of Working Group I to the Fifth Assessment Report of the Intergovernmental Panel on Climate Change*. Cambridge University Press, Cambridge, United Kingdom and New York, NY, USA, 2013. doi: 10.1017/CBO9781107415324.

D. L. Jackson and J. J. Bates. Upper tropospheric humidity algorithm assessment. *Journal of Geophysical Research*, 106(D23):32259–32270, 2001. doi: 10.1029/2001JD000348.

V. John. Algorithm Theoretical Basis Document, UTH Edition 1.0, Upper Tropospheric Humidity TCDR CM-14711. Technical report, EUMETSAT SAF on Climate Monitoring, 2016.

V. O. John and B. J. Soden. Temperature and humidity biases in global climate models and their impact on climate feedbacks. *Geophysical Research Letters*, 34(18):L18704, 2007. doi: 10.1029/2007GL030429.

V. O. John, G. Holl, R. P. Allan, S. A. Buehler, D. E. Parker, and B. J. Soden. Clear-sky biases in satellite infrared estimates of upper tropospheric humidity and its trends. *Journal of Geophysical Research*, 116:D14108, 2011. doi: 10.1029/2010JD015355.

J. H. Jungclaus, N. Fischer, H. Haak, K. Lohmann, J. Marotzke, D. Matei, U. Mikolajewicz, D. Notz, and J. S. von Storch. Characteristics of the ocean simulations in the Max Planck Institute Ocean Model (MPIOM) the ocean component of the MPI-Earth system model. *Journal of Advances in Modeling Earth Systems*, 5(2):422–446, 2013. doi: 10.1002/jame.20023.

L. Kluft, S. Dacie, S. A. Buehler, H. Schmidt, and B. Stevens. Re-examining the first climate models: Climate sensitivity of a modern radiative-convective equilibrium model. *Journal of Climate*, in review.

A. Kottayil, V. O. John, and S. A. Buehler. Correcting diurnal cycle aliasing in satellite microwave humidity sounder measurements. *Journal of Geophysical Research*, 118: 101–113, 2013. doi: 10.1029/2012JD018545.

R. S. Lindzen, M.-D. Chou, and A. Y. Hou. Does the Earth have an Adaptive Infrared Iris? *Bulletin of the American Meteorological Society*, 82(3):417–432, 2001. doi: 10.1175/1520-0477(2001)082<0417:DTEHAA>2.3.CO;2.

C. Melsheimer, C. Verdes, S. A. Buehler, P. Eriksson, D. G. Feist, S. Ichizawa, V. O. John, Y. Kasai, G. Kopp, N. Koulev, T. Kuhn, O. Lemke, S. Ochiai, F. Schreier, T. R. Sreerekha, M. Suzuki, T. Takahashi, S. Tsujimaru, and J. Urban. Intercomparison of general purpose clear sky atmospheric radiative transfer models for the millimeter/submillimeter spectral range. *Radio Science*, 40:RS1007, 2005. doi: 10.1029/2004RS003110.

C. Merchant. What is a Fundamental Climate Data Record? `http://www.fiduceo.eu/content/what-fundamental-climate-data-record`, 2018. Last access: 22 March 2019.

K. Minschwaner and A. E. Dessler. Water Vapor Feedback in the Tropical Upper Troposphere: Model Results and Observations. *Journal of Climate*, 17:1272–1282, 2004. doi: 10.1175/1520-0442(2004)017<1272:WVFITT>2.0.CO;2.

NOAA CLASS webpage. TOVS/ATOVS. `https://www.avl.class.noaa.gov/release/data_available/tovs_atovs/index.htm`. Last access: 17 March 2019.

NWP SAF-webpage. Mathematical overview of RTTOV. `https://www.nwpsaf.eu/site/software/rttov/documentation/rttov-mathematical-overview/`, 2019.

R. T. Pierrehumbert, H. Brogniez, and R. Roca. *On the Relative Humidity of the Atmosphere*, chapter 6, pages 143–185. T. Schneider and A. Sobel, 2007.

C. H. Reick, T. Raddatz, V. Brovkin, and V. Gayler. Representation of natural and anthropogenic land cover change in MPI-ESM. *Journal of Advances in Modeling Earth Systems*, 5(3):459–482, 2013. doi: 10.1002/jame.20022.

J. Robel, A. Graumann, and Kathy Kidwell. NOAA KLM user's guide with NOAA-N, -N' supplement. Technical report, National Oceanic and Atmospheric Administration, National Environmental Satellite, Data, and Information Service, National Climatic Data Center, Remote Sensing and Applications Division, 2009.

L. S. Rothmann, I. E. Gordon, Y. Babikov, A. Barbe, D. Chris Brenner, P. F. Bernath, M. Birk, L. Bizzocchi, V. Boudon, L. R. Brown, A. Campargue, K. Chance, E. A. Cohen, L. H. Coudert, V. M. Devi, B. J. Drouin, A. Fayt, J.-M. Flaud, R. R. Gamache, J. J. Harrison, J.-M. Hartmann, C. Hill, J. T. Hodges, D. Jacquemart, A. Jolly, J. Lamouroux, R. J. Le Roy, G. Li, D. A. Long, O.. M. Lyulin, C. J. Mackie, S. T. Massie, S. Mikhailenko, H. S. P. Muller, O. V. Naumenko, A. V. Nikitin, J. Orphal, V. Perevalov, A. Perrin, E. R. Polovtseva, C. Richard, M. A. H. Smith, E. Starikova, K. Sung, S. Tashkun, J. Tennyson, G. C. Toon, Vl. G. Tyuterev, and G. Wagner. The HITRAN2012 molecular spectroscopic database. *Journal of Quantitative Spectroscopy and Radiative Transfer*, 130:4–50, 2012. doi: 10.1016/j.jqsrt.2013.07.002.

R. Saunders, P. Rayer, A. von Engeln, N. Bormann, L. Strow, S. Hannon, S. Heilliette, X. Liu, F. Miskolczi, Y. Han, G. Masiello, J.-L. Moncet, G. Uymin, V. Sherlock, and D. S. Turner. A comparison of radiative transfer models for simulating Atmospheric Infrared Sounder (AIRS) radiances. *Journal of Geophysical Research*, 112(D1), 2007. doi: 10.1029/2006JD007088.

R. Saunders, J. Hocking, E. Turner, P. Rayer, D. Rundle, P. Brunel, J. Vidot, P. Roquet, M. Matricardi, A. Geer, N. Bormann, and C. Lupu. An update on the RTTOV fast radiative transfer model (currently at version 12). *Geoscientific Model Development*, 11: 2717–2737, 2018. doi: 10.5194/gmd-11-2717-2018.

J. Schulz and L. Schüller. Wasserdampf- und Wolkenklilmatologie aus Fernerkundungsdaten. *Promet*, 37:5–16, 2011.

P. K. Sen. Estimates of the regression coefficient based on Kendall's tau. *Journal of the American Statistical Association*, 63(324):1379–1389, 1968. doi: 10.2307/2285891.

L. Shi and J. J. Bates. Three decades of intersatellite-calibrated High-Resolution Infrared Radiation Sounder upper tropospheric water vapor. *Journal of Geophysical Research*, 116:D04108, 2011. doi: 10.1029/2010JD014847.

B. J. Soden and F. P. Bretherton. Upper Tropospheric Relative Humidity From the GOES 6.7 μm Channel Method and Climatology for July 1987. *Journal of Geophysical Research*, 98(D9):16669–16688, 1993. doi: 10.1029/93JD01283.

B. J. Soden and I. M. Held. An Assessment of Climate Feedbacks in Coupled Ocean–Atmosphere Models. *Journal of Climate*, 19(14):3354–3360, 2006. doi: 10.1175/JCLI3799.1.

B. J. Soden, D. D. Turner, B. M. Lesht, and L. M. Miloshevich. An analysis of satellite, radiosonde, and lidar observations of upper tropospheric water vapour from the Atmospheric Radiation Measurement Program. *Journal of Geophysical Research*, 109: D04105, 2004. doi: 10.1029/2003JD003828.

B. J. Soden, D. L. Jackson, V. Ramaswamy, M. D. Schwarzkopf, and X. Huang. The Radiative Signature of Upper Tropospheric Moistening. *Science,* 310:841–844, 2005. doi: 10.1126/science.1115602.

R. W. Spencer and W. D. Braswell. How dry is the tropical free troposphere? Implications for global warming theory. *Bulletin of the American Meteorological Society*, 78(6): 1097–1106, 1997. doi: 10.1175/1520-0477(1997)078<1097:HDITTF>2.0.CO;2.

B. Stevens, M. Giorgetta, M. Esch, T. Mauritsen, T. Crueger, S. Rast, M. Salzmann, H. Schmidt, J. Bader, K. Block, R. Brokopf, I. Fast, S. Kinne, L. Kornblueh, U. Lohmann, R. Pincus, T. Reichler, and E. Roeckner. Atmospheric component of the MPI-M Earth System Model: ECHAM6. *Journal of Advances in Modeling Earth Systems*, 5(2):146–172, 2013. doi: 10.1002/jame.20015.

K. E. Taylor, R. J. Stouffer, and G. A. Meehl. An Overview of CMIP5 and the experiment design. *Bulletin of the American Meteorological Society*, 93(4):485–498, 2012. doi: 10.1175/BAMS-D-11-00094.1.

H. Theil. A rank-invariant method of linear and polynomial regression analysis. *Proceedings of the Royal Netherlands Academy of Sciences*, 53:Part I: 386?392, Part II: 521?525, Part III: 1397?1412, 1950. doi: 10.1007/978-94-011-2546-8_20.

A. A. Wing, K. A. Reed, M. Satoh, B. Stevens, S. Bony, and T. Ohno. Radiative-Convective Equilibrium Model Intercomparison Project. *Geoscientific Model Development Discussions*, 2017. doi: doi.org/10.5194/gmd-2017-213.

WMO-OSCAR. Observing Systems Capability Analysis and Review Tool webpage. `https://www.wmo-sat.info/oscar/satellites/view/306`, 2019. Last access: 14 January 2019.

X. Wu, J. J. Bates, and S. J. S. Khalsa. A Climatology of the Water Vapor Band Brightness Temperature from NOAA Operational Satellites. *Journal of Climate*, 6:1282–1300, 1993. doi: 10.1175/1520-0442(1993)006<1282:ACOTWV>2.0.CO;2.

Acknowledgements

Finally, I would like to thank everyone who has contributed to the success of this thesis.

My special thanks go to Prof. Dr. Stefan Bühler, for the idea of this thesis, for the helpful discussions and for giving me the opportunity to work independently as part of the EU project FIDUCEO. I am glad that I had the possibility to work on such an exciting topic in the course of my master's thesis.

I also owe a special thanks to my second supervisor Dr. Martin Burgdorf, who has always provided me advise and support, particularly when I needed help to orientate myself in the FIDUCEO project. Furthermore, I would like to thank him for carefully reading through my thesis and making helpful suggestions for improvement.

Moreover, I was very lucky to have Dr. Imke Hans sharing an office with me. I would like to thank her very warmly for regularly listening to my problems, for long and fruitful discussions, for reading through all the documents I have written and for providing me with tips and support, although being occupied with her Phd thesis.

I want to thank all members of the group "Radiation and Remote Sensing" for the cooperative working atmosphere, for the assistance in programming and for valuable impulses during our group meetings. Particularly a big thank you goes to Lukas Kluft for providing me his RCE model atmospheres and to Laura Dietrich for simulating the brightness temperatures for the 1%CO_2 run. Moreover, I would like to thank Dr. Verena Grützun and Miriam Tivig for providing me with ideas and inspirations during our "Tropical Café".

Furthermore, I would like to express my sincere thanks to all the members of the EU project FIDUCEO, for giving me the opportunity to contribute to such an important project

and for their patience and helpfulness.

For the stimulating and reassuring discussions during our work breaks I want to thank my fellow students Laura Dietrich, Marc Prange, Simon Michel, Jakob Dörr, Daniel Sorg, Joscha Fregin and Henning Dorff.

Last but not least, I would like to thank my boyfriend Tobi and my family back home for always standing behind me. Without all your support I would not have made it through my studies.

Versicherung an Eides statt

Hiermit versichere ich an Eides statt, dass ich die vorliegende Arbeit im Studiengang M.Sc. Meteorologie selbstständig verfasst und keine anderen als die angegebenen Hilfsmittel – insbesondere keine im Quellenverzeichnis nicht benannten Internet-Quellen – benutzt habe. Alle Stellen, die wörtlich oder sinngemäß aus Veröffentlichungen entnommen wurden, sind als solche kenntlich gemacht. Ich versichere weiterhin, dass ich die Arbeit vorher nicht in einem anderen Prüfungsverfahren eingereicht habe und die eingereichte schriftliche Fassung der auf dem elektronischen Speichermedium entspricht.

Mit einer Ausstellung der Arbeit in der Fachbibliothek bin ich einverstanden.

Hamburg, den 23.04.2019